

University of Alberta

**Hydraulics of Plunging Drop Structures in Urban
Drainage Systems**

by

Graciela Adriana Camino Zapata

A thesis submitted to the Faculty of Graduate Studies and Research
in partial fulfillment of the requirements for the degree of

Doctor of Philosophy

in

Water Resources Engineering

Civil and Environmental Engineering

©Graciela Adriana Camino Zapata

Fall 2011

Edmonton, Alberta

Permission is hereby granted to the University of Alberta Libraries to reproduce single copies of this thesis and to lend or sell such copies for private, scholarly or scientific research purposes only. Where the thesis is converted to, or otherwise made available in digital form, the University of Alberta will advise potential users of the thesis of these terms.

The author reserves all other publication and other rights in association with the copyright in the thesis and, except as herein before provided, neither the thesis nor any substantial portion thereof may be printed or otherwise reproduced in any material form whatsoever without the author's prior written permission.

To the memory of my father, Guillermo Jr.

Abstract

Understanding the flows inside plunging drop structures could enable efficient ways to transport water between different elevations in urban drainage systems. A physical modelling approach is pursued throughout this thesis to investigate the complex nature of the flow developed inside some of these structures. This work is comprised of four parts based partly on published papers or on manuscripts submitted for publication. Two separate experimental investigations focus on the performance of stacked drop manholes. A flow regime classification is proposed based on hydraulic characteristics. The effectiveness of these structures in dissipating the surplus inflow energy and its suitability to perform adequately under diverse flow conditions is assessed. An analysis based on the integral momentum equation is presented to estimate pool depths and energy losses under critical flow conditions. A third part of the thesis is focused on estimating the energy dissipation achieved by simple jet diffusion inside a confined chamber emulating the pool formed at the base of various drop structures. A vertical jet issuing into a rectangular chamber is set under two values of confinement and three locations of entry. Velocity measurements to assess the axial centerline jet velocity development as well as turbulent characteristics for the axial center line of an eccentric jet are presented. The results are compared to classical jet behaviour and jets under other confined conditions showed that a confined setting can be largely dissipative. A fourth portion of the thesis is centered on a tall plunging dropshaft. Flow observations on the jet out of a horizontal inlet pipe and falling down the shaft are described. Velocities at different cross sections along the shaft and outflow are computed from high speed imagery. Local water flow rates are recorded to help understand the physics of the flow inside the dropshaft. Finally, energy losses and air flow rates are compared with the ones reported on similar plunging structures.

Acknowledgements

I have been privileged to receive the guidance, encouragement and friendship of my supervisors: Dr. David Z. Zhu and Dr. Nallamuthu Rajaratnam. I evidenced in awe Dr. Raj's vast expertise in hydraulics and Dr. Zhu's acuteness. I have benefitted from their continual supervisory, constructive advise, wisdom, and careful reading of the drafts throughout the long process of the research.

I gratefully acknowledge the contribution of the thesis examining committee: Dr. James Kells, Dr. Morris Flynn, Dr. Peter Steffler, Dr. David Zhu and Dr. Nallamuthu Rajaratnam for their relevant feedback and thorough review of this document.

I would like express my gratitude to the Professors of Water Resources group: Dr. Peter Steffler, Dr. Mark Loewen, Dr. Faye Hicks, Dr. Thian Gan, Dr. David Z. Zhu and Dr. Nallamuthu Rajaratnam who have shared their knowledge, abundant expertise and insightful critics in diverse areas of water resources inside and outside the class environment.

I also wish to especially thank the lab technicians: Perry Fedun and Chris Krath. Their skilled work has enable the completion of the lab work.

I am thankful to the people of the Drainage and Construction Section and Planning Section of the City of Edmonton as well as Stantec Consulting for their opinions during the progress report sessions.

It has been a rewarding experience to share formal class sessions, office time, lab work as well as numerous informal conversations with my fellow colleagues during my stay in U of A. Thanks to my friends A. Kiyani, M. M. Ali, J. Aqeel, I. Lima-Neto, M. Mukto, J. Cai, W. Zang, A. Azimi, R. Islam, A. Habibzadeh, N. Hall, E. Chen, N. Abarca, G. Ejaz, A. Aslam, A. Ibrahim, J. Nafziger, N. Kovachis, M. Langford, A. Hall, J. Morley and M. Shafieifar.

I feel deeply fortunate to count on the unconditional support of my loving husband, who has given me his strength, his patience, the best gift of my baby boy, and above all his love that we deeply share. My mother has always been a soul mate who has been committed to my work as her own. Her perseverance is compared to none. Her push in the last stage of my research had made the final product to come out. Finally, my grandpa G. Camino and my extended family have always given me the confidence and invaluable encouragement that I treasure.

Contents

List of figures	vii
List of Tables	x
CHAPTER 1:INTRODUCTION	1
1.1 DROP STRUCTURES IN URBAN DRAINAGE SYSTEMS.....	1
1.2 THESIS OUTLINE.....	3
CHAPTER 2:USE OF A STACKED DROP MANHOLE: A CASE STUDY IN EDMONTON.....	5
2.1 INTRODUCTION	5
2.2 EXPERIMENTAL DESIGN	8
2.2.1 <i>Flow patterns and regimes</i>	12
2.2.2 <i>Energy dissipation</i>	15
2.3 WATER DEPTH IN CHAMBERS	24
2.4 SUMMARY AND CONCLUSIONS	28
CHAPTER 3:HYDRAULICS OF SYMMETRIC STACKED DROP MANHOLES	32
3.1 INTRODUCTION	32
3.2 EXPERIMENTAL PROGRAM	34
3.3 FLOW PATTERNS AND REGIMES	36
3.3.1 <i>First Chamber</i>	36
3.3.2 <i>Second Chamber</i>	39
3.4 THEORETICAL FRAMEWORK	42
3.4.1 <i>First chamber under a dropshaft type flow</i>	42
3.4.2 <i>Second chamber for submerged flow with orifice outflow</i>	43
3.4.3 <i>Orifice flow equation</i>	48
3.5 ENERGY DISSIPATION.....	50
3.6 AIR ENTRAINMENT	54
3.7 SUMMARY AND CONCLUSIONS	56
CHAPTER 4:JET DIFFUSION INSIDE A CONFINED CHAMBER	71
4.1 INTRODUCTION	71
4.2 EXPERIMENTAL ARRANGEMENT AND PROGRAM	72
4.3 METHOD TO COMPUTE ENERGY LOSSES.....	75

4.4	EXPERIMENTAL RESULTS.....	80
4.4.1	<i>Data quality analysis</i>	80
4.4.2	<i>Velocity decay</i>	82
4.4.3	<i>Velocity profiles</i>	85
4.4.4	<i>Turbulence characteristics</i>	87
4.5	MODEL PREDICTIONS	91
4.6	CONCLUSIONS.....	92
CHAPTER 5: FLOW OBSERVATIONS IN A TALL PLUNGING DROPSHAFT		99
5.1	INTRODUCTION	99
5.2	EXPERIMENTAL SETUP AND PROGRAM.....	104
5.3	EXPERIMENTAL RESULTS AND DISCUSSION	107
5.3.1	<i>Data conditioning</i>	107
5.3.2	<i>Qualitative observations on the physics of the flow</i>	109
5.3.3	<i>Energy dissipation</i>	120
5.3.4	<i>Air demand</i>	122
5.4	CONCLUSIONS AND REMARKS	125
CHAPTER 6: CONCLUSIONS AND RECOMMENDATIONS.....		128

List of Figures

<i>Figure 1.1 Typical urban drainage drop structures: a) vortex dropshaft of helical inlet; b) plunging dropshaft of elbow entrance; and, c) sanitary drop manhole (adapted from Williamson, 2001).....</i>	<i>2</i>
<i>Figure 2.1 Constructed stacked drop manhole in Windermere, Edmonton. A total of 5 such manholes were used to resolve an elevation drop of 50 m.....</i>	<i>7</i>
<i>Figure 2.2 Laboratory model of a stacked drop manhole: a) sectional view; and, b) plan view. All the dimensions are given in meters.....</i>	<i>9</i>
<i>Figure 2.3 Definition sketches and flow regimes in the manhole: a) Free overfall; b) Surface jet 2; c) Submerged sharp-edged opening; d) Fully submerged.....</i>	<i>13</i>
<i>Figure 2.4 Flow regimes and onset conditions</i>	<i>14</i>
<i>Figure 2.5 Water surface profiles of the flow in regime I at a) $Q^* = 0.2$, $F=0.8$. b) $Q^* = 0.44$, $F=2.3$; and regime III at c) $Q^* = 1.07$, $F=3$</i>	<i>17</i>
<i>Figure 2.6 Rope like vortex for $Q^* > 1.2$ in chamber two</i>	<i>18</i>
<i>Figure 2.7 Water surface profiles of the flow passing through the rectangular opening facing upstream</i>	<i>20</i>
<i>Figure 2.8 Energy head losses per chamber</i>	<i>21</i>
<i>Figure 2.9 Comparison of energy head losses per chamber for series of experiments E.....</i>	<i>22</i>
<i>Figure 2.10 Energy loss coefficient as a function of the drop parameter</i>	<i>23</i>
<i>Figure 2.11 Sketch of the flow in chamber two</i>	<i>24</i>
<i>Figure 2.12 Non-dimensional water depths in chambers.....</i>	<i>25</i>
<i>Figure 2.13 Comparison of depths of water in chamber.....</i>	<i>26</i>
<i>Figure 2.14 Non dimensional water depths in chambers in free fall regime.....</i>	<i>27</i>
<i>Figure 3.1 Setup of a SDM: a) Sectional view; b) Plan view of a symmetric SDM; c) Plan view of an offset SDM.....</i>	<i>35</i>
<i>Figure 3.2 Flow types: a) Regime I. Drop flow; b) Regime II. Transitional flow; c) Regime III. Dropshaft flow</i>	<i>37</i>
<i>Figure 3.3 Dimensionless pool depths inside the first chamber of a SDM.....</i>	<i>38</i>
<i>Figure 3.4 Two flow regimes in the second chamber of a small height SDM: a) orifice flow in outlet at $Q^*=0.92$; b) full pipe flow in outlet at $Q^*=0.96$</i>	<i>40</i>
<i>Figure 3.5 Velocity distribution of a fully surcharged flow on the horizontal center plane at the level of the opening section between chambers. a) $Q^*=0.80$; b) $Q^*=0.38$.....</i>	<i>41</i>

Figure 3.6 Control volumes in a SDM: a) first chamber (CV_1); b) second chamber (CV_2).....	46
Figure 3.7 Predictions on non-dimensional pool depths in: a) the first chamber and, b) the second chamber	47
Figure 3.8 a) Dimensionless pool depth in the first chamber for all runs under RIII; b) discharge coefficient in the outflow of first chamber of symmetric SDMs	49
Figure 3.9 Relative energy losses inside SDMs of diverse configurations with respect to Q^*	51
Figure 3.10 Dimensionless energy losses as a function of dimensionless velocity head in SDMs.....	51
Figure 3.11 Local head coefficients related to the drop Froude number.....	53
Figure 3.12 Dimensionless air flow rates inside the chambers of a symmetric SDM of large height ($h=8D$) of two opening heights.....	55
Figure 3.13 Dimensionless air flow rates inside: 1) symmetric SDMs of two opening heights, 2) a single drop manhole (Gargano et al. 2008), and 3) a dropshaft (Rajaratnam et al. 1997).....	56
Figure 3.14 A1 a) Normalized velocity profiles; b) normalized pressure profiles in the centerline of the jet out of the opening between chambers of a SDM ($h_1=4D$) under RI.	62
Figure 3.15 A2 Normalized pressure and velocity profiles in the centerline of the jet out of the opening under fully surcharged flow inside a small height SDM ($h=4D$).....	63
Figure 4.1 Experimental setup with definition sketch of the rectangular chamber.....	74
Figure 4.2 Velocity structure of a circular bluff wall jet (inside a manhole chamber).....	75
Figure 4.3 Maximum velocity decay in the streamwise direction of centered jets	83
Figure 4.4 Maximum velocity decay in the streamwise direction of eccentric jets	84
Figure 4.5 Mean velocity distribution of an eccentric jet (center plane XY).....	86
Figure 4.6 Mean velocity distribution of an eccentric jet (center plane XZ).....	86
Figure 4.7 Normalized turbulence intensities in the streamwise direction: a) u'^2/um_0 ; b) u'^2/U_0	88
Figure 4.8 Distribution of dimensionless mean kinetic energy $K^{0.5}/U_0$ in center planes XY and XZ.....	91
Figure 4.9 Comparison of relative energy losses of the flow from jet onset to exit in outlet pipe.....	92
Figure 5.1 Sketches of a tall dropshaft in: a) model and b) prototype of typical ratio drop height to diameter of the shaft of the city of Edmonton (source: A.E. 2008).....	103
Figure 5.2 Experimental setup and definition zones	105
Figure 5.3 Calibration of total-pressure probes of 2.4mm, 4.9mm, 7.3mm and rake of 2.4mm probes for $Q^*=0.64$	107

Figure 5.4 Convergence of the sampling time in the air velocity measurements for a dimensionless water discharge $Q^*=0.56$	108
Figure 5.5 Instantaneous air velocity under off-pump condition for noise analysis	109
Figure 5.6 Inflow jet at impingement on shaft's wall (adapted from Quick, 1990).....	110
Figure 5.7 Frontal view (section A-A in Fig. 5.5) of the location of impingement on the curved inner periphery of the shaft for a) $Q^*=0.16$ and b) $Q^*=0.54$	110
Figure 5.8 instantaneous scenes of spray formation in the outflow for a range of inflow discharges (MotionScope camera, shutter speed $900 \mu s$).....	112
Figure 5.9 Sequence of water streams spreading and diffusing at different elevations of the shaft and outlet for $Q^*=0.16$ (Phantom v7.3 camera, shutter speed $20 \mu s$).....	113
Figure 5.10 Dimensionless water sampling rate q/q_m in the main direction (inflow-outflow) at a section $h/D_s=17$ distance from the invert inlet elevation (negative values in x-axis are to distinguish the impingement side of the shaft at $r/r_o=-1$)	114
Figure 5.11 Dimensionless water sampling rate q/q_m across the inflow-outflow direction of different sections of the shaft (negative values in x-axis are to distinguish the impingement side of the shaft at $r/r_o=-1$).....	116
Figure 5.12 Dimensionless contours of water sampling rate q/q_m across a section of the shaft at a distance $h/D_s=17$ from the inlet	117
Figure 5.13 Mean relative water velocities along the shaft related to dimensionless drop height h/D_s for a range of discharges.....	118
Figure 5.14 Mean relative water velocities along the shaft related to dimensionless drop height h/D_s for a range of discharges.....	119
Figure 5.15 Relative energy losses attained in a tall dropshaft for a range of dimensionless flow rates Q^*120	
Figure 5.16 Comparison of relative energy losses for a range of dimensionless discharges of diverse plunging drop structures.....	121
Figure 5.17 Comparison of mean relative energy losses with respect to the relative drop height of diverse plunging drop structures	122
Figure 5.18 Air and water flow rates in a dimensional and dimensionless form.....	123
Figure 5.19 Comparison of relative air flow rates for different drop height plunging dropshafts	124

List of Tables

<i>Table 2.1. Experimental conditions.....</i>	<i>11</i>
<i>Table 2.2. Typical jet flows in chambers.....</i>	<i>14</i>
<i>Table 3.1. Summary of experimental conditions</i>	<i>36</i>
<i>Table 5.1 Geometry of previous models on plunging drop manholes and dropshafts.....</i>	<i>102</i>
<i>Table 5.2 Geometry of the model plunging dropshaft.....</i>	<i>104</i>

CHAPTER 1: INTRODUCTION

1.1 DROP STRUCTURES IN URBAN DRAINAGE SYSTEMS

Waste water and storm water drainage systems are predominantly designed to let water flow by gravity action to a downstream water body or treatment facility. Sewers at different elevations should be provided with adequate structures to resolve the elevation difference between them. The main purpose of the drop structure is to minimize the effects of the falling flow by dissipating energy from the falling flow and reducing the amount of air entrained into the structure (Williamson 2001).

Two basic categories of vertical drop structures may be distinguished according to their height and inlet characteristics: a) vortex dropshafts and b) plunging type drop structures: dropshafts and drop manholes (Fig. 1.1). Vortex dropshafts let the flow to spiral down the vertical shaft essentially clinging along the shaft walls and the air moves as a central air core (Hager 1999). Plunging drop structures simply direct the flow into the vertical shaft and no provisions for the air flow are in place within the shaft.

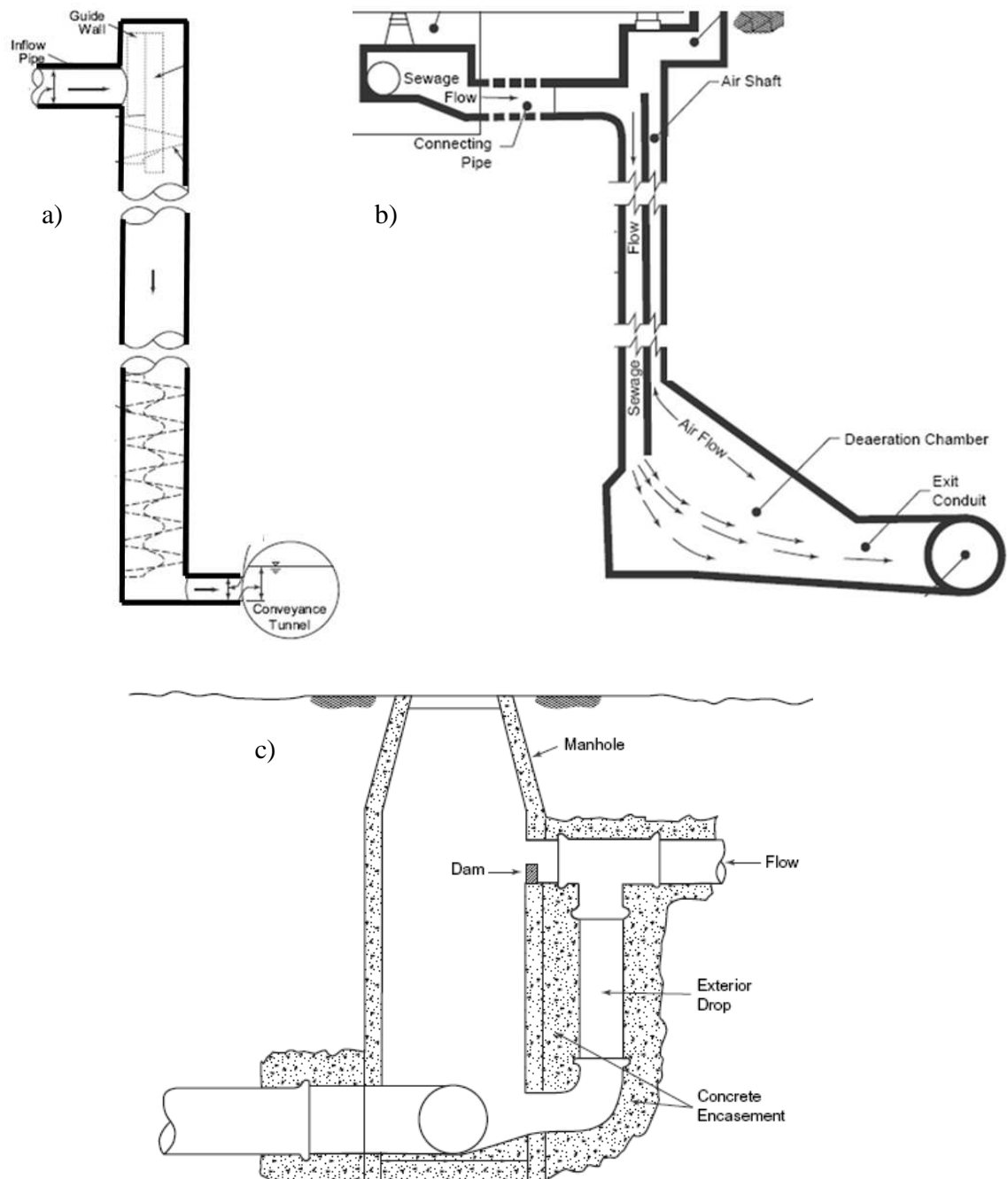


Figure 1.1 Typical urban drainage drop structures: a) vortex dropshaft of helical inlet; b) plunging dropshaft of elbow entrance; and, c) sanitary drop manhole (adapted from Williamson, 2001)

1.2 THESIS OUTLINE

In this thesis, the hydraulics of certain plunging drop structures implemented in sewer and stormwater systems are investigated. In **Chapter 2** of this thesis, a novel design of drop manhole consisting of two identical rectangular chamber manholes at an elevation difference is introduced. The purpose of the stacked drop manhole (SDM) was to extend the limit of drop height referred to be around 1.00 m by most sewer City guidelines in North America (e.g. City of Calgary 2000). The study focused on the hydraulic performance of the stacked structure. Four distinctive regimes were classified on the basis of the pool depths in the chambers and the manhole geometry. The energy losses were associated to the inflow conditions, geometry of the design and outlet controls.

The SDM design was further investigated in **Chapter 3**. A symmetric SDM is proposed to extend results on the offset design to a more compact and simplified arrangement that could help to standardize its usage. A critical flow condition associated with pool depths is recognized and a theoretical treatment based on the integral momentum equation is pursued. In addition, a fully surcharged state is recreated by imposing a downstream pressure. Detailed velocity profiles at the horizontal center plane of the opening are measured under surcharged flow and energy loss coefficients are obtained. Finally, bulk air flows are measured in a large height SDM (drop height $h = 8D$, where D is the inlet pipe diameter) and compared with drop structures of comparable drop height.

In **Chapter 4**, a key process of energy dissipation achieved within most plunging drop structures is reviewed in detail. Energy loss by jet diffusion occurring inside the pool formed at the base of drop manholes and dropshafts can be very effective. An investigation of a confined circular jet issuing vertically into a pool was examined. An inspection of the effect of the enclosure size and the location of entry of the inflow jet as well as the velocity decay in the centerline of the jet was done. A method was developed based on jet theory to assess the capacity to dissipate energy of a confined jet enclosed within a chamber of only few diameters in length.

In **Chapter 5**, an experimental study of the flow inside a model plunging dropshaft with drop height about 20 times its shaft diameter is introduced. The model could stand for a typical prototype dropshaft in the city of Edmonton with a shaft diameter of 1.20 m at a scale ratio of about three on a Froudean similitude. Observations on the impinging jet from the inlet pipe on the shaft wall were made. Relative energy losses achieved by the structure as well as relative air flow rates were obtained for the whole range of discharges available for the setup. **Chapter 6** summarizes our main results.

References

Hager, W.H. 1999. *Wastewater Hydraulics*. Theory and practice. Springer, Berlin.p.628

Williamson, S. (2001). *Drop structure design for wastewater and stormwater collection systems*. Monograph 14. New York, Parsons Brinckerhoff Inc.: p.131.

CHAPTER 2: USE OF A STACKED DROP MANHOLE: A CASE STUDY IN EDMONTON*

2.1 INTRODUCTION

Outfalls discharging into rivers should ensure that their erosive capacity is not detrimental to the river or creek system. Windermere Subdivision is a recently constructed urban development within the City of Edmonton, Alberta, located on the bank of the North Saskatchewan River with an elevation of about 50 m above the river valley. To convey stormwater safely into the North Saskatchewan River without excessive flow velocity is crucial. Two possible approaches were examined to convey and dispose urban storm waters to the river: 1) a deep tunnelling system with a number of street sewers connected to it; and, 2) a shallow sewer system with a number of small drops.

The first approach requires dropshafts of a large height drop (of about 50 m). Much of the research to explore efficient ways to carry water flows from one elevation to another has centered on drop structures of larger height (see review Williamson 2001). Plunging type dropshafts of rectangular and circular shapes have been investigated (Rajaratnam et al. 1997; Chanson 2004; Chanson 2007) as well as vortex type dropshafts (Hager 1990; Guo and Song 1991; Vischer and Hager 1995; Zhao et al. 2006). A second approach is to provide a surface level system having sloping sewers connected in intervals by drop manholes. This option is much more

* The content of this chapter has been published in the Canadian Journal of Civil Engineering, CJCE. Camino, G. A., Zhu, D. Z., Rajaratnam, N. and Manas, S. (2009). "Use of a stacked drop manhole for energy dissipation: A case study in Edmonton." *Can. J. Civ. Eng.*, 36: 1037-1050. Thomas C. Keefer medal for the best paper in the Canadian Journal of Civil Engineering

economical basically due to the reduced excavation costs, simplified construction techniques and easier maintenance than the first approach, as it is close to the ground level. In Windermere Subdivision, it is estimated that the surface level system has a cost of about \$250,000 in comparison to the \$1 million for a deeper system. With this significant economical benefit, it was important to study this second approach.

Very few guidelines for designing small height drop structures are currently available. In North America, most cities simply restrict the drop to less than 1m (City of Calgary 2000). Restriction of the height reduces potentially harmful effects on the structure such as erosion, abrasion, vibration, and excessive air entrainment (Hager 1999). The design guideline of the City of Edmonton requires a drop manhole to be used for elevation differences higher than 1.00 m between incoming and outgoing pipe. This drop manhole should be equipped with air vents and be designed following requirements outlined in the design guidelines. After a discussion with the City, a drop manhole of 1.40 m would be allowed and treated as standard as long as the design scheme ensures an efficient performance; i.e. it conveys urban waters safely into the outlet maximizing the dissipation of the excess energy of the inflow.

To further extend the limit of the drop height, a novel design scheme was proposed by Stantec Consulting by stacking two identical drop manholes at different elevations. The purpose of the design was to dissipate excessive kinetic and potential energy and meet the general requirements of municipal drainage agencies. The scheme consisted of two rectangular chambers of same geometry, with a length of 3.00 m and a width of 2.40 m, and a total drop height of 2.80 m. The chambers were left uncovered with full provision of air. The proposed design was recently constructed (Fig. 2.1) after the confirmation of the design by this study.



Figure 2.1 Constructed stacked drop manhole in Windermere, Edmonton. A total of 5 such manholes were used to resolve an elevation drop of 50 m.

There are no previous records related to stacked manholes. In general, very few studies have focused on small-height drop structures in municipal systems. Christodoulou (1991) explored initially the study of energy dissipation in drop manholes concentrating on supercritical flows at inflows. All the processes of energy dissipation inside these structures were lumped into a coefficient of local head-loss, K , as is frequently used in standard manholes (Pedersen and Mark 1990). The loss coefficient, K , was essentially found to depend on the parameter \sqrt{gh}/V_1 where h is the drop height and V_1 is the incoming average velocity. The head loss coefficient K was also found to be linked to manhole size, and exit shape under surcharged flow conditions in a straight-through pipe (Kusuda and Arao 1996). Later Calomino et al. (1999) supplemented this with empirical relationships for K as a function of the approach flow Froude number, shaft diameter, filling ratio (i.e. flow depth/pipe diameter) and drop height.

More recently, de Marinis et al. (2007) presented experimental results of an ongoing

study on drop manholes. The relative energy losses, for experiments for one drop height (2.00 m) and various approach flow conditions, were correlated with the dimensionless parameter related to the approach flow Froude number and the inflow filling ratio. The losses showed certain correspondence with the regimes classified by the jet impact location. These previous investigations have given some light on the global losses but there are still several issues such as flow development, regime transitions, flow patterns and most favourable drop heights that are not well known.

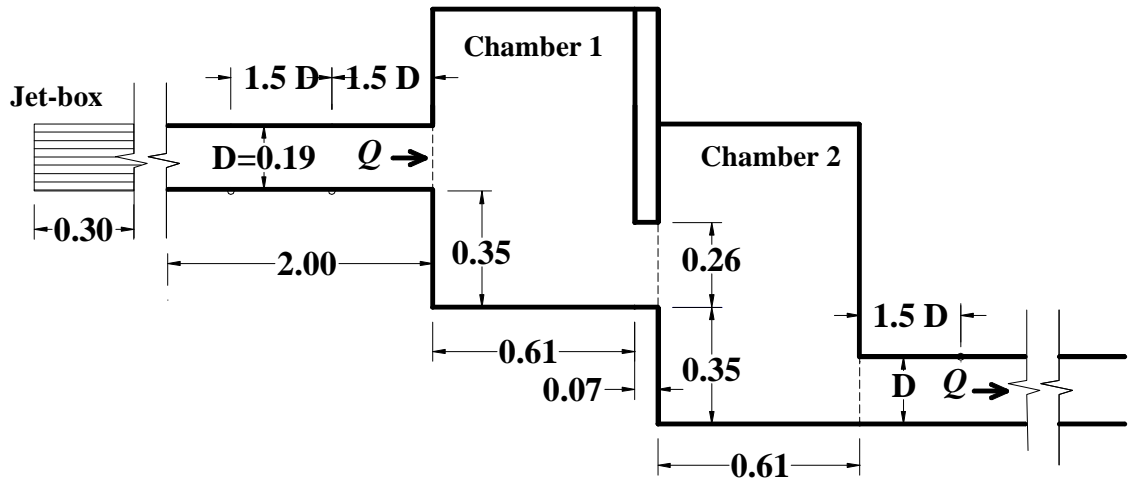
In the present study, flow within a stacked drop manhole model was carefully observed for several inflow rates (subcritical and supercritical) over a wide range of prototype flows. The study focused on the hydraulic behaviour of the flow inside the stacked structure along with an assessment of the energy dissipation, distinctive flow regimes and water levels in the chambers. By exploring the performance of the stacked manhole, this study intends to further our understanding on flows inside standard drop manholes and propose an economical option for hydraulic designers.

2.2 EXPERIMENTAL DESIGN

A model of the prototype design was built in the Blench Hydraulics Laboratory of the University of Alberta. The prototype has an inlet pipe (DR41 PVC) of 750 mm in diameter with a slope $S = 5.5\%$ and a design discharge of $1.80 \text{ m}^3/\text{s}$. Two reinforced concrete chambers house 1.40 m drop height each. The opening between the first and the second chambers consisted of a sharp-edged rectangular opening of 1.00 m width and 1.00 m height. To prevent short circuiting, the location of the opening was offset to the alignment of the inlet-outlet pipes. The outlet pipe had the same diameter as that of the inlet pipe and its invert was level with the bottom of the second chamber.

The physical model was designed based on Froudian similitude. Adapted to the available acrylic commercial pipes, the model resulted in a scale of 1:3.95 and the manhole chambers were constructed using Plexiglas for visual observation. All dimensions of the physical model are detailed in Fig. 2.2. Note that the outlet pipe

was set horizontal and behaved as a short pipe. Uniform flow in the inlet in prototype was produced using a jet-box and a set of plates in the inlet pipe of the model (Gargano and Hager 2002). Dye plumes and tuft probes and mesh were used for observation of flow patterns for certain regimes.



b)

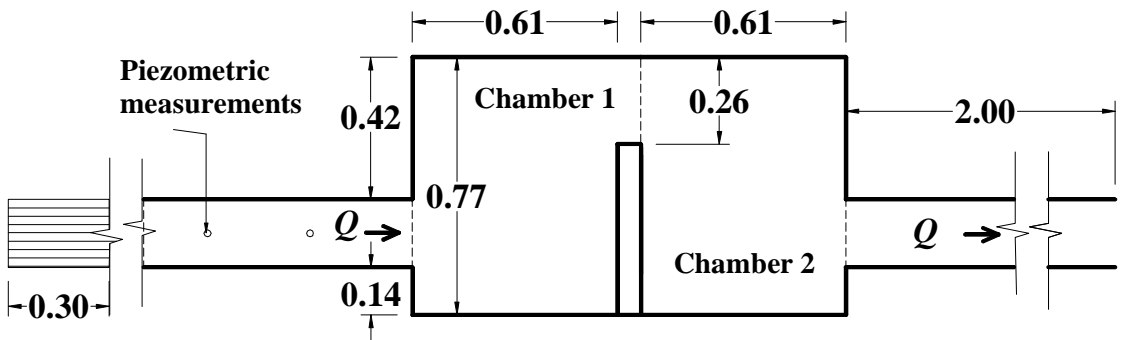


Figure 2.2 Laboratory model of a stacked drop manhole: a) sectional view; and, b) plan view. All the dimensions are given in meters.

An online magnetic flow meter was used to measure the discharge. A number of piezometers were placed in both pipes at $1.5D$ distance between each other, where D is the pipe diameter. Straight and inverted point gauges were implemented to measure free falling nappes, water surface profiles in chambers and flow over the rectangular

opening between chambers. Averaged velocities on the flow passing through the opening were attempted using a Schiltknecht miniAir20 digital anemometer of propeller for periods of 120 sec. In addition, Prandtl Pitot-tubes of 3 mm and 1.5 mm diameter were adopted to measure the velocity in the falling nappes.

Point gauge measurements of the upper and lower nappes of the inflow jet had errors less than 0.5 mm. Similarly, errors on piezometric depths were estimated to be less than 0.5 mm in the conduits. Water depths in conduits had estimated errors of the order of 2 mm in the inlet and about 5 to 10 mm in the more aerated flow in the outlet. The water surface elevations inside the chambers could be highly fluctuating with standard deviations of about 5 mm for small flow rates up to about 50 mm for large flow rates. Velocity measurements in the sharply contracted flow over the opening between chambers could have errors of the order of 0.1 m/s, measured with the anemometer. More streamlined flows in the falling jet were measured with the Prandtl tube with reading errors less than 1mm.

Prototype conditions were tested in a first set of experiments by varying the inflow rates (A series). A second set of experiments (B series) was designed to assess the sensitivity to the approaching Froude number. A wide range of flows were reproduced in series B at filling ratios of 54, 50, 43, 38, 28 and 22 %. The inflow was subcritical in some cases and supercritical in other experiments. In the C series, experiments were run at full pipe flow condition for which no plates were used. Series A, B and C had a constant section in the rectangular opening, that was opening width $b_w = 0.26$ m and height $h_w = 0.26$ m.

Experiments in series D and E were designed to investigate the contribution of each chamber to the overall performance of the manhole. The series D was run with a reduced opening width between the chambers. This reduced width produced a comparable depth of water in both chambers. The series E was run with reduced opening height and had an additional change in the drop heights; i.e. the drop in the first chamber $h_1 = 0.22$ m and the drop in the second chamber $h_2 = 0.48$ m. Primary

details of the experiments are given in Table 2.1.

Table 2.1. Experimental conditions

Series	F*	h ₁ (m)	h ₂ (m)	Rectangular	Comments
				opening (h _w x b _w)	
A	3.0 - 4.1	0.35	0.35	0.26 x 0.26	Prototype flow condition with incoming pipe slope S = 5.5%
B	0.6 - 7.4	0.35	0.35	0.26 x 0.26	Testing the effect of incoming Froude number by setting y ₀ /D = 54, 46, 40, 32, 22 & 14% and variable inflow rate.
C	-**	0.35	0.35	0.26 x 0.26	Incoming pipe running full
D	0.7 - 5.7	0.35	0.35	0.26 x 0.13	Testing comparable water depths chambers and using filling ratios of y ₀ /D = 14 & 32 %
E	0.8 - 5.7	0.22	0.48	0.13 x 0.26	Testing variation in drop height and using a filling ratio of y ₀ /D = 32 %

* Froude number in the inflow was calculated as $F = V_1 / \sqrt{(gy_h)}$, where V_1 is the approaching velocity and y_h is the hydraulic depth = A/T ; T being the top width and A , the wetted cross-sectional area of inlet pipe.

** Full pipe flow condition

2.2.1 *Flow patterns and regimes*

The flow behaviour inside the structure is rather complicated. It was obvious that the flow in the first chamber was primarily dominated by the inflow conditions, while in the second chamber, carrying less incoming momentum, was basically controlled by the downstream conditions. Except for very small discharges, the inflow entering the chambers undergoes considerable deflection after impingement. The jet, impacting on the chamber's bottom, forms two vertically-oriented circulating zones at both sides of the jet, and rotating in opposite directions (Fig. 2.3). The jet impacting on the front wall gets equally deflected, creating a component of the jet rising up (observe first chamber in Figs. 2.3c and 2.5c) which falls forming a water curtain along the wall.

Either free falling, surface jet, or submerged jet could be developed in the chambers as a function of tailwater depth and incoming conditions. **Regime I** was distinguished by a purely free falling condition in both jets. It happened at low discharges (Fig. 2.3a), i.e. when the dimensionless discharge Q^* was lower than about 0.61, where Q^* is defined as $Q/\sqrt{gD^5}$, where g is the acceleration due to gravity. For Q^* higher than 0.32, the outgoing pipe entrance became submerged. **Regime II** was recognized by a surface jet developed in the second chamber (referred to as **Surface Jet 2** in this paper). **Surface jet 2** occurred for Q^* between 0.61 and 1.00 while three different conditions were found in the first chamber: (1) A free surface flow running through the rectangular opening for $Q^* < 0.77$; (2) A submerged condition in the opening for $Q^* > 0.77$ from upstream; and, (3) Submergence at the opening, and a surface jet in the inlet flow for $Q^* > 0.96$. This last case is depicted in Fig. 2.3b. **Regime III** was defined by submergence of the opening from the downstream flow. It starts when Q^* was higher than about 1.00 as illustrated in Fig. 2.3c. This stage generated either an inflow surface jet for $Q^* < 1.30$ or a submerged jet otherwise. Finally, fully submerged flow as **Regime IV** was characterized in both chambers for Q^* larger than 1.30 (Fig. 2.3d). An outline of the types of flows is summarized in Table 2.2.

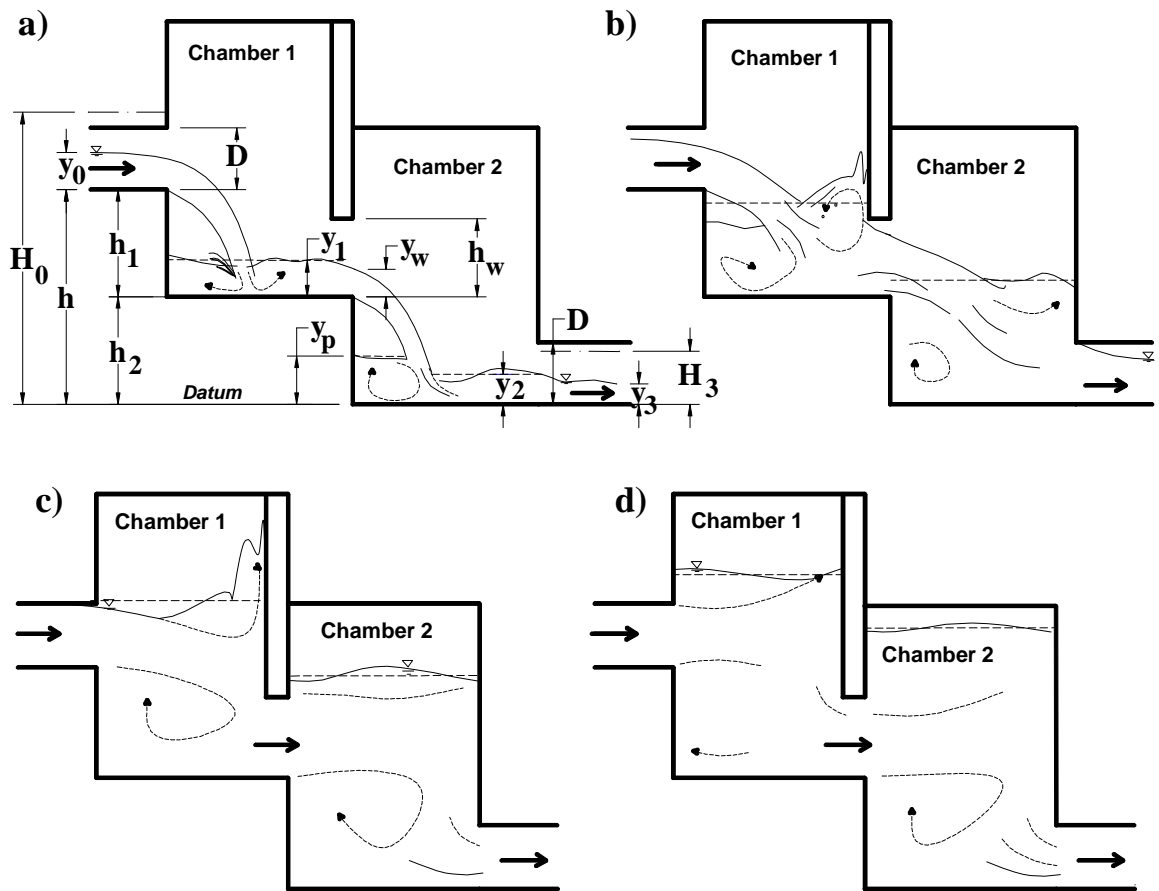


Figure 2.3 Definition sketches and flow regimes in the manhole: a) Free overfall; b) Surface jet 2; c) Submerged sharp-edged opening; d) Fully submerged

The averaged water depths in the first and second chamber, y_1 and y_2 , respectively, are correlated with Q^* in Fig. 2.4. Each water depth was divided by a characteristic length scale, i.e. y_1 by h_w , height of the rectangular opening for the first chamber and y_2 by D , the exit pipe diameter for the second one. This arrangement was found convenient for design purposes of the present geometry; yet, a more general approach will be presented in following paragraphs. The correlations in Fig. 2.4 suggest that the normalized water depth in chambers for all approaching Froude numbers tested ($0.5 < F < 7$) is not particularly dependent on the incoming flow conditions.

Table 2.2. Typical jet flows in chambers

1 st chamber		2 nd chamber		Other relevant features	
$0 < Q^* < 0.96$	Free falling jet 1	$0 < Q^* < 0.61$	Free falling jet 2	$Q^* > 0.32$	Submerged entrance of outgoing pipe
$0.96 < Q^* < 1.30$	Surface jet 1	$0.61 < Q^* < 1.00$	Surface jet 2	$Q^* > 0.77$	Submerged rect. opening from u/s
$Q^* > 1.30$	Submerged jet 1	$Q^* > 1.00$	Submerged jet 2	$Q^* > 0.96$	Submerged rect. opening from d/s (fully submerged)

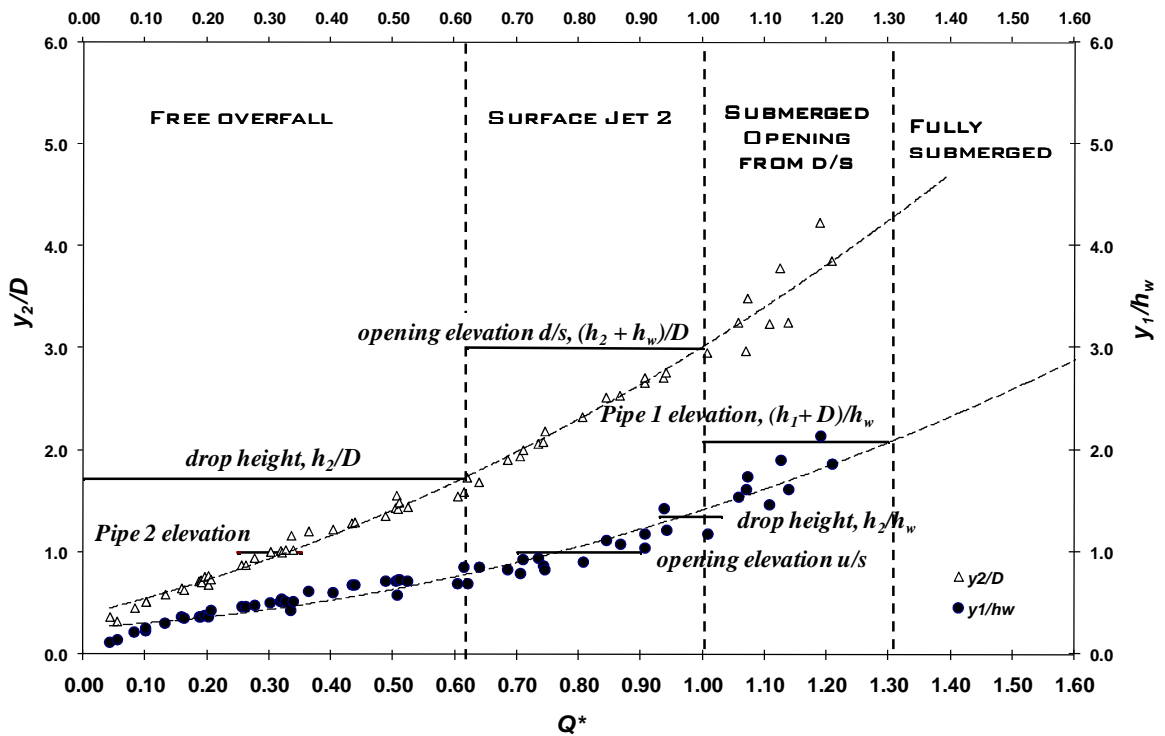


Figure 2.4 Flow regimes and onset conditions

2.2.2 Energy dissipation

Essentially, the mechanisms of energy loss in the stacked drop manholes can be four-fold: 1) impact on the bottom of the chamber; 2) impact on the front wall; 3) jet plunging into the pool; and 4) circulation in chambers. The impingement location is dependent on the inflow characteristics and geometry of the chambers. The process of impact can be explored considering the nappe characteristics of the falling jets. The nappe profiles of rectangular and circular sections behave differently. The vertical nappe thickness from a circular conduit expands almost linearly starting from the end depth y_e . Conversely, the nappe thickness decreases slightly in a jet coming from a rectangular conduit (Clausnitzer and Hager 1997).

Overall energy dissipation The total energy loss in a stacked drop manhole may be written as:

$$[2.1] \quad \Delta H = H_0 - H_3$$

where $H = z + y + \alpha \frac{V^2}{2g}$ is the total head, with z being the invert elevation above the datum, y the water depth, and V the mean velocity. α is the kinetic energy coefficient and was assumed to be 1 for the inflow and outflow sections. Subscript 0 indicates the incoming section, and subscript 3 the exit pipe about $5D$ downstream, see Fig. 2.3a. Thus H_0 and H_3 are the total head before and after the stacked manhole. The datum is fixed at the level of the invert elevation of the outlet pipe. The relative energy loss η is defined as:

$$[2.2] \quad \eta = \Delta H / H_0$$

Free overfall ($Q^* < 0.61$). Regime I presented the highest energy dissipation, i.e. between 93 % and 78 %. The dissipation appears to be caused by the impact of the falling jet. The impingement can either be on the bottom of the chamber or the front wall of the first chamber depending on the incoming jet momentum. The

impingement on the front wall occurred when the inflow Froude number was greater than 3, and $Q^* > 0.60$ (Fig. 2.5a and b). In the second chamber, the falling jet never hit the front wall. It plunged into the pool and eventually reached the bottom. In the first chamber, a circular hydraulic jump, which is a highly dissipative process, was observed at very low discharges. The flow through the rectangular opening presented approximately critical flow (less than 17 % difference in depth) when flowing partially full.

Surface jet 2 ($0.61 < Q^* < 1.00$). As the tailwater depth increased, the nappe changed in direction and the flow was lifted from the bottom becoming a surface jet. In regime II, the air pocket under the falling jet disappeared due to large water depths in the second chamber. In this regime, the rectangular opening section presented free surface flow or submerged flow from the upstream side. For the highest discharges of the range, $0.97 < Q^* < 1.00$, surface jet was also observed in the inlet flow. There was considerable air entrainment in the impingement zone of the first chamber. The resulting energy dissipation varied between 61 % and 78 %, being lower for the higher discharges.

Fully submerged jet ($Q^* > 1.30$). The water level in the chambers immersed the incoming jets inside the chambers. This type of flow was not tested in our setup and it is only included here for completeness. Extrapolating previous results, the energy dissipation is expected to be less than about 45 %.

Opening submerged from downstream side ($1.00 < Q^* < 1.30$). In regime III, the flow in the rectangular opening is submerged from the downstream side (chamber 2). The nature of this flow is depicted in Fig. 2.5c. For $Q^* > 1.2$, the formation of a long vortex rope, consisting of air bubbles, was observed following a transition from free falling to submerged jet (Fig. 2.6). This bubble vortex rope broke after it entered the exit pipe. Similar observations were reported in lateral or side channels when increased tailwater created submergence (Hager 1999). The energy dissipation achieved in this regime varied between 48 % and 64 %. This is the highest range of

discharges achieved in this setup.

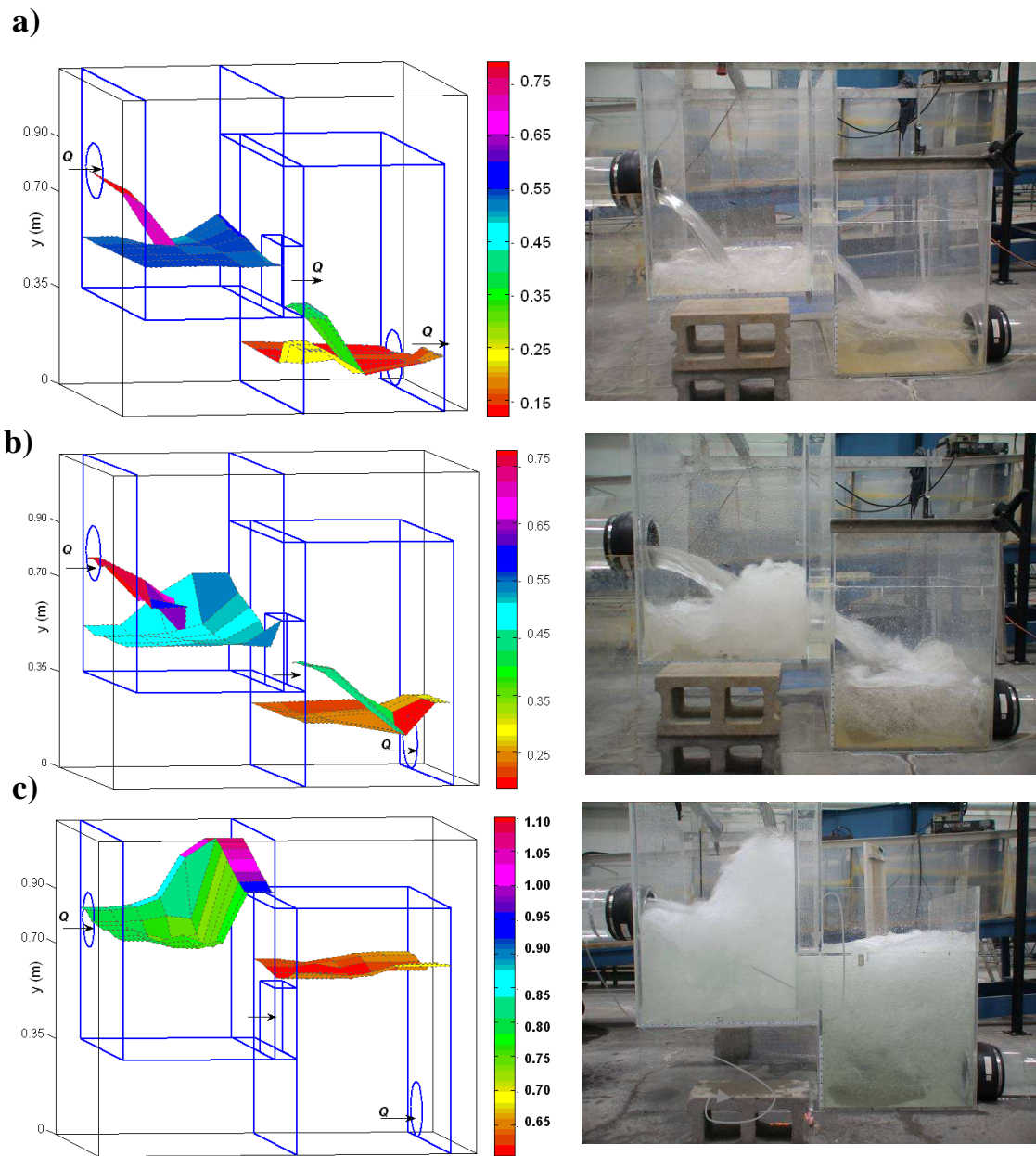


Figure 2.5 Water surface profiles of the flow in regime I at a) $Q^* = 0.2, F=0.8$. b) $Q^* = 0.44, F=2.3$; and regime III at c) $Q^* = 1.07, F=3$

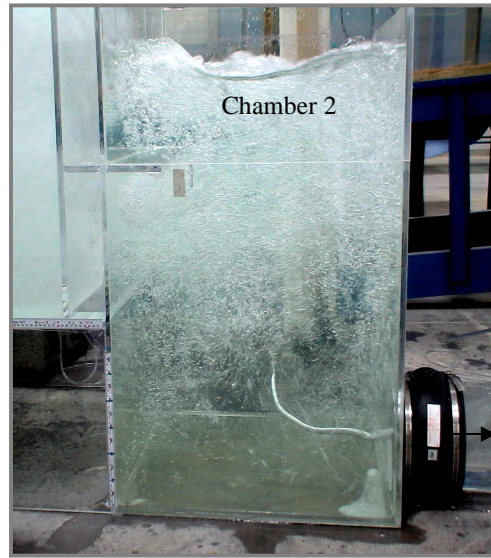


Figure 2.6 Rope like vortex for $Q^* > 1.2$ in chamber two

Energy loss per chamber Two chambers contribute differently to the overall energy dissipation. The first chamber dissipates most of the energy, while the second chamber appears to stabilize and absorb high turbulent variations. Both chambers, integrated in one structure, seem to have an advantageous compound behaviour. The individual contribution of each chamber to the total energy loss required the assessment of the total energy of the approaching flow, the flow passing through the opening between chambers and the outgoing flow.

Due to the location of the opening (offset to the inlet-outlet axial direction), the flow over the opening was contracted laterally and deflected asymmetrically as observed in the view facing upstream of Fig. 2.7. Under free overfall regime ($Q^* < 0.6$), the flow entering the second chamber behaves as a semi-confined falling jet. The velocity head of the flow passing through the opening section may be computed by dividing the wet cross sectional area into slices of constant width. The variation of velocity in each slice was small; hence, each slice was assumed to have the same flow velocity throughout. The energy head of the flow across the opening may be written as $H_i = h_2 + \alpha' \times y_{average} + \frac{\sum v_i^3 \times \Delta A}{2g \sum v_i \times \Delta A}$; where ΔA is the elementary area of each slide. Note that α' is a pressure coefficient accounting for the fact that the

pressure distribution at the end section is not hydrostatic. If the pressure distribution is considered hydrostatic, α' should be 1. The actual pressure distribution has been modified theoretically for different channel sections (Dey 2002) and studied experimentally in rectangular channels (Rajaratnam and Muralidhar 1968). Delleur et al. (1956) established α' from 0.6 to 0.3 for flow ranging from subcritical to supercritical for a rectangular channel. A value of α' equal to 0.5 was considered a good approximation at the end section of the rectangular opening.

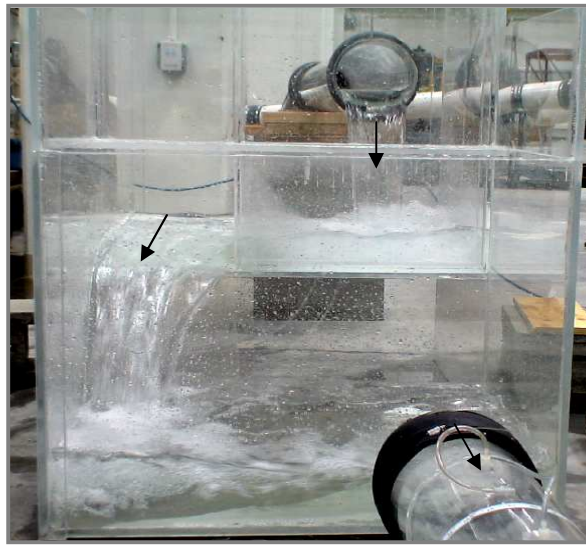


Figure 2.7 Deflection of flow over the rectangular opening at $Q^*=0.1$

The averaged energy head showed less than 10 % difference from a single-water-depth energy calculation. Hence, the total head at the rectangular opening was computed as $H_w = h_2 + \alpha' y_w + \frac{1}{2g} \left(\frac{Q}{C_c (y_w \times b_w)} \right)^2$, where b_w represents the width of the sharp-edged opening, h_2 is the drop height of the second chamber. H_w is the total energy head computed from a single depth measurement y_w at the center of the opening.

For $Q^*>0.61$ (beyond regime I), the energy of the flow across the opening was

computed by $H_w = y_2 + \frac{1}{2g} \left(\frac{Q}{C_c (y_w \times b_w)} \right)^2$, where the water surface height y_2 at section right after the opening replaces the piezometric level for the emerging jet into the second chamber. C_c is the contraction coefficient for the flow across the opening section.

When the sharp-edged rectangular opening gets submerged, it behaves as an orifice control. Based on the measurements of transverse water profiles, the contraction coefficient $C_c = A_c/A$ was found to vary between 0.74 and 0.94 in the opening between chambers, where A_c is the contracted area and A is the cross sectional flow area covered by the water depth (measured close to lateral wall) times the opening width (Fig. 2.8). An average value of 0.8 was considered representative for C_c at that opening. In any outlet, it is advantageous to avoid the formation of an orifice flow which would reduce the discharge capacity. It is convenient to provide a smooth entrance curve in both outlets (rectangular opening and outlet pipe) to maintain their carrying capacity.

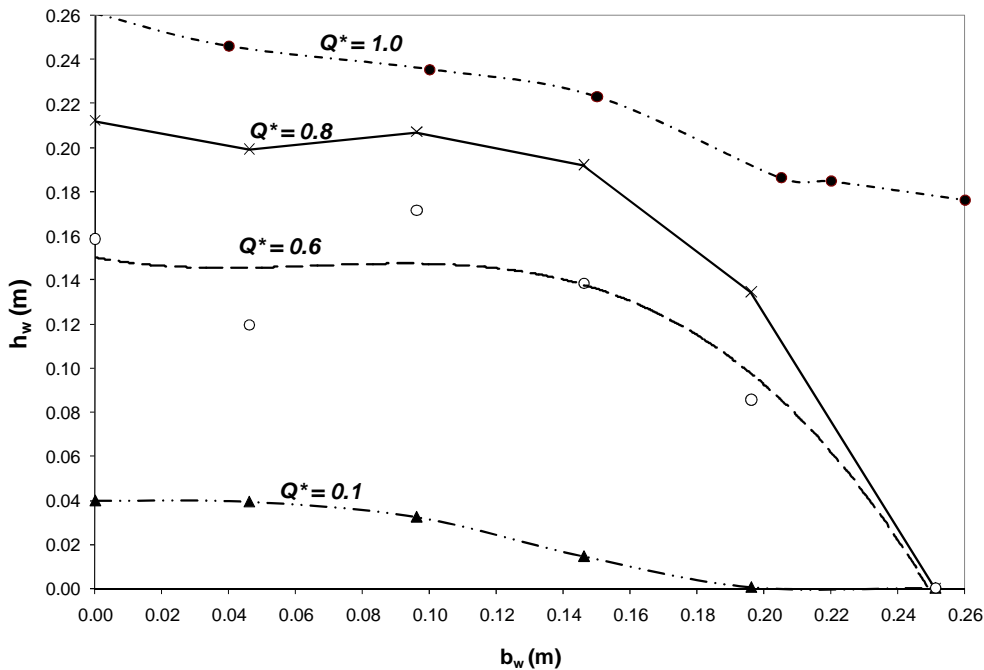


Figure 2.7 Water surface profiles of the flow passing through the rectangular opening facing

upstream

On average, the energy lost by jet impact and water circulation inside the first chamber corresponds to about 50 % of the approaching energy for series A to C. Accordingly, the losses achieved in the second chamber were of 26 % of the total averaged head loss of 76 % attained by all the processes inside the structure for series A to C (Fig. 2.9).

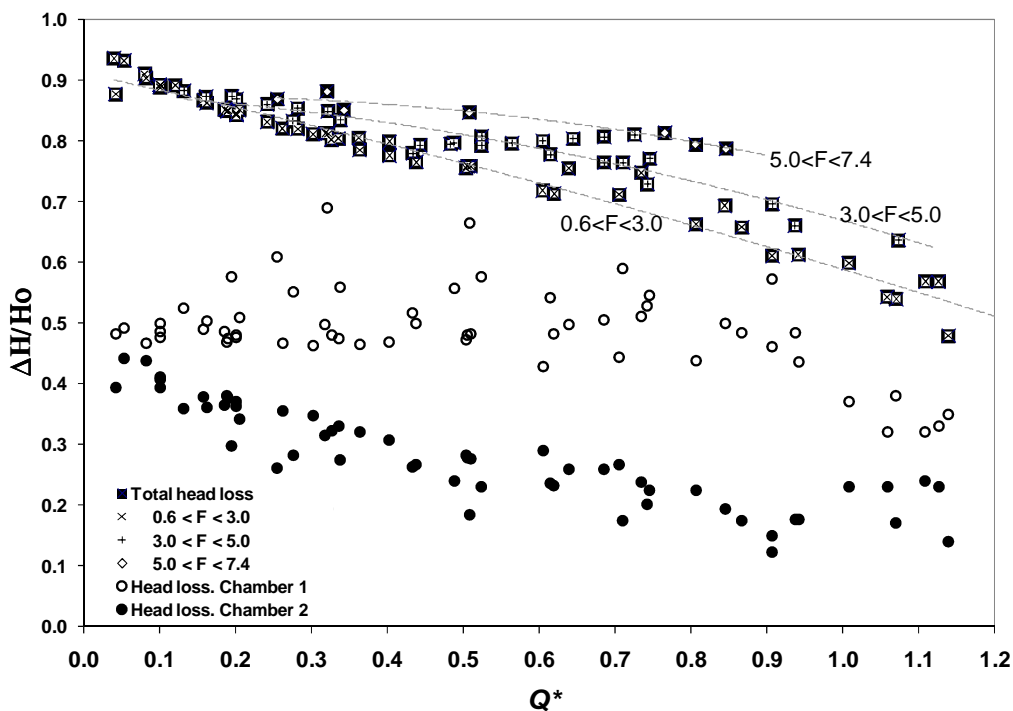


Figure 2.8 Energy head losses per chamber

The Froude number of the inflow does not appear to have a significant effect on the energy loss in our study in contrast to that in single drops. However, it is observable that for a given Froude number, with increasing discharge there is a decrease in the energy losses (Fig. 2.9). Analogous relationships were reported previously in single drops for subcritical and supercritical flows (Chamani and Beirami 2002). Similarly, for a given discharge, an increase in the Froude number showed a decrease in the relative energy losses in single drops, which differs from our results.

Neither the change in the drop height of the chambers nor the variation in the cross sectional area of the opening revealed any significant effect on the global head loss of the structure. As shown in Fig. 2.10, the contribution of the second chamber to the total head became important when its drop height increased; i.e. in series of experiments E. Its head loss became not only higher than the one of the first chamber but also of the same order of that of the first chamber when both chambers had the same drop height.

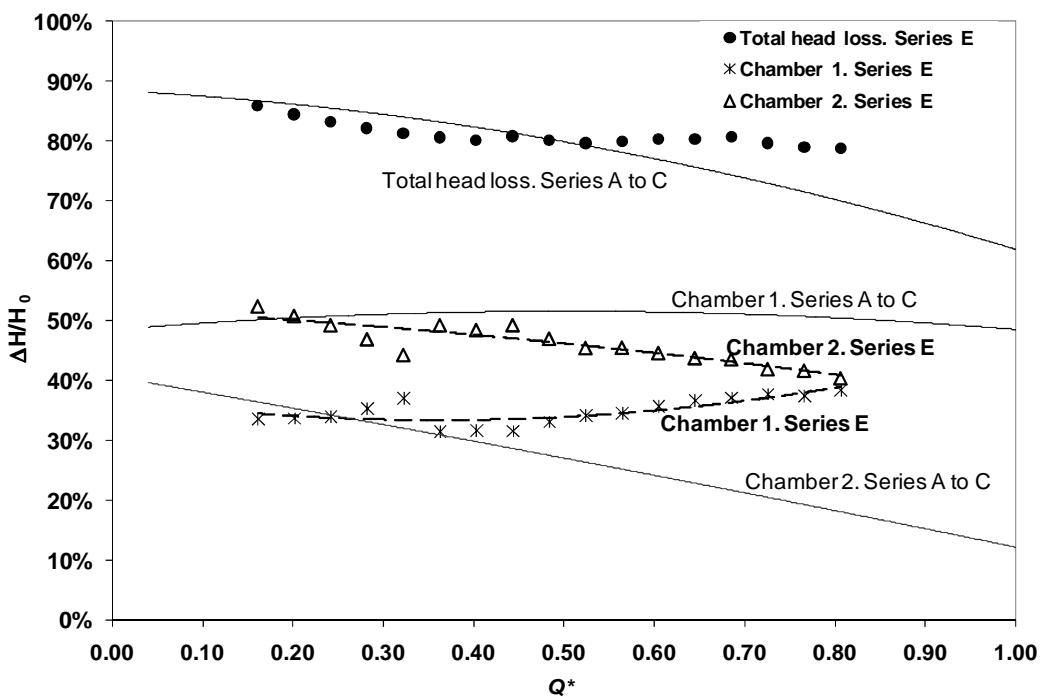


Figure 2.9 Comparison of energy head losses per chamber for series of experiments E

A closer assessment of the energy head components in the inflow and outflow shows that when the incoming Froude number F is less than about 3, the total inflow head is basically the piezometric head considering the datum at the invert elevation of the outlet pipe. The piezometric head is then approximately constant at the level of the drop height. As the approaching momentum increases, the incoming kinetic energy becomes important. For instance, for Froude numbers greater than five, the velocity head is as high as the piezometric head.

It is noteworthy to mention that the approaching momentum was not significantly carried down into the outlet pipe. For the experiments in E series with increased drop height in the second chamber, it appears that only for certain discharges ($Q^* = 0.44$ and 0.48) the momentum imparted by the falling jet was by some means carried down to the outlet pipe which increased its discharge capacity; even so, its final effect in the energy loss was negligible.

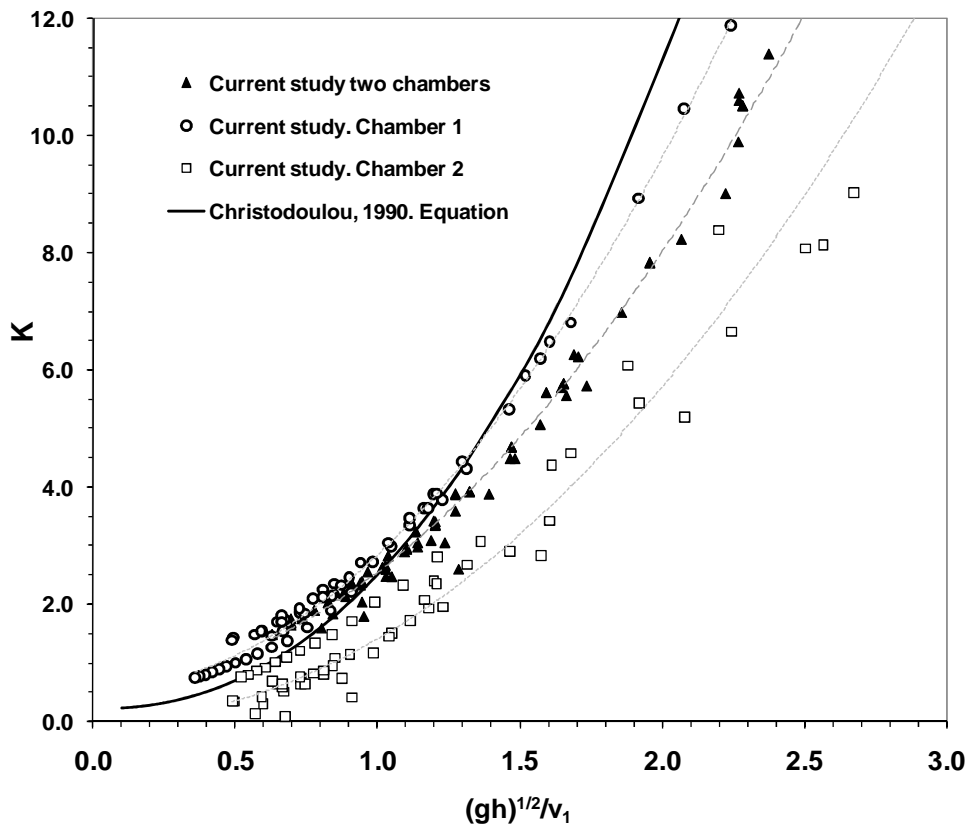


Figure 2.10 Energy loss coefficient as a function of the drop parameter

Comparison with typical manholes The loss coefficient K in a drop manhole was previously correlated with the so called drop parameter \sqrt{gh}/V_1 (Christodoulou 1991). Interestingly enough, this parameter shows high correlation with the energy losses in the stacked drop manhole (Fig. 2.11). When the impact processes are important, i.e. at large drop heights or high Froude numbers; one can argue that the

impact pressure is basically a function of the vertical velocity attained by the falling jet. Therefore, drop manholes of equivalent total height are expected to have comparable energy losses if the inflows are also equivalent. The loss in the first chamber is more closely correlated to the drop parameter than that in the second chamber. Due to the uncertainty in velocity measurements at the rectangular opening, the drop parameter for the second chamber was computed considering the mean velocity in the inlet pipe.

2.3 WATER DEPTH IN CHAMBERS

From a design standpoint, it is essential to anticipate the water depths in chambers to set their height related to a given discharge and pipe diameter. A typical Bernoulli equation can be applied along the streamline shown in Fig. 2.12 between points 1 and 2 in a submerged outlet of a drop manhole. Point 1 is located just upstream and Point 2 is located immediately downstream of the exit.

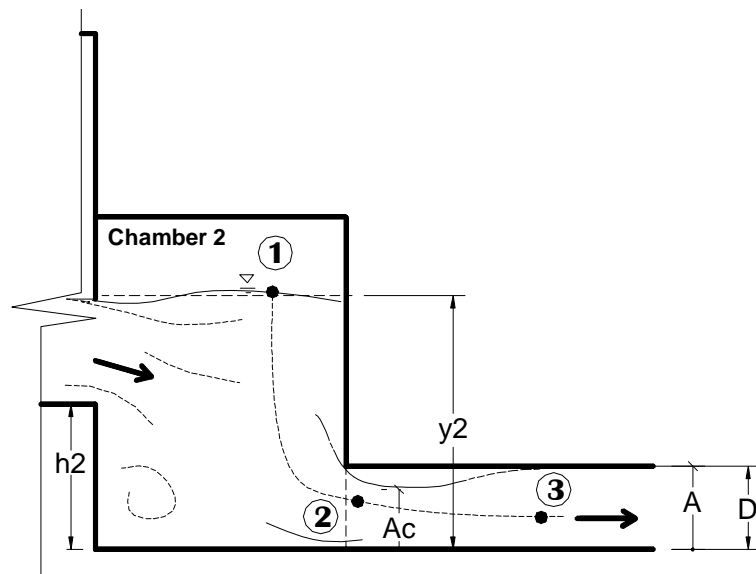


Figure 2.11 Sketch of the flow in chamber two

One can estimate the exit velocity as: $V_2 = \sqrt{2g(z_1 - z_2)}$, where z_1 and z_2 are the elevations of the corresponding points. Basic assumptions of this derivation include:

1) pressures at 1 and 2 are the same and equal to atmospheric, which is not really true for point 2; and 2) the approach velocity at point 1 is negligible. Further, if the depth in the chamber y can be approximated to $(z_1 - z_2)$, we have $Q = C_D \times A \sqrt{2gy}$, where C_D is the discharge coefficient and A is the area of the outlet. C_D should account for inaccuracies from applying the Bernoulli equation, simplifying assumptions, contraction of the flow by the sharp-edged outlet, residual pressure in 2 and internal friction.

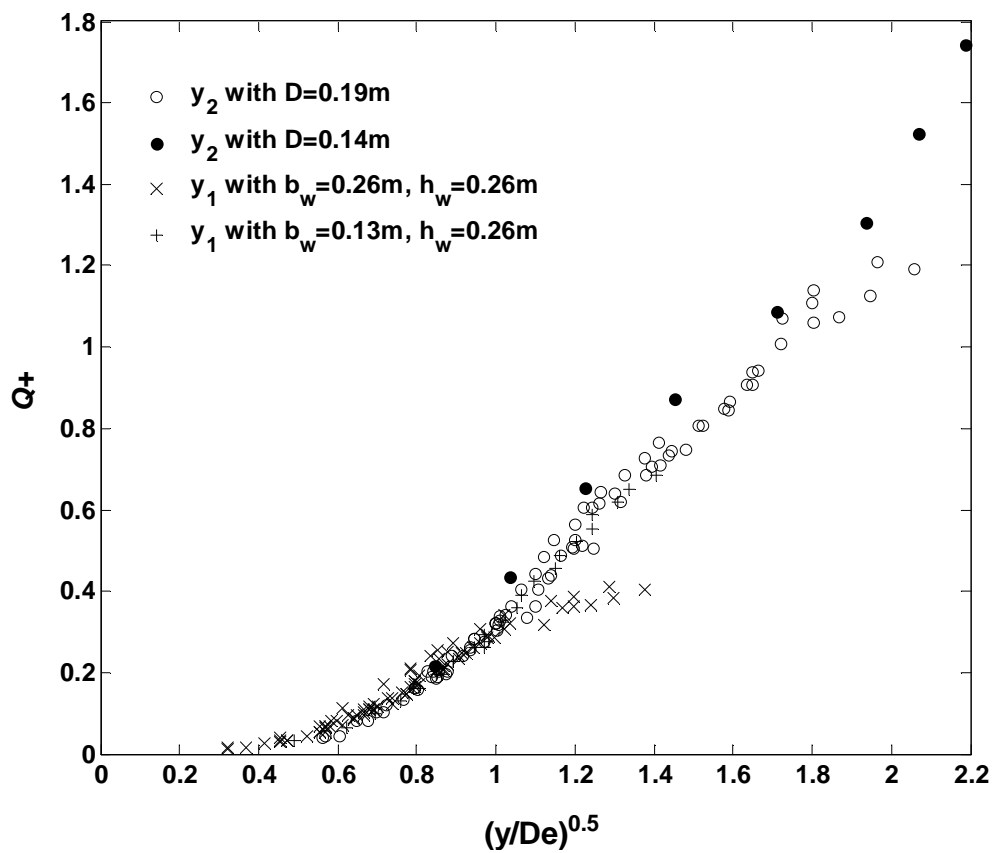


Figure 2.12 Non-dimensional water depths in chambers

Considering the theoretical velocity $\sqrt{2gy}$, a possible non-dimensional relationship can be established as $Q^+ = Q / \sqrt{gD_e^5}$. Q^+ should be then proportional to $\sqrt{y/D_e}$, where $D_e = \sqrt{4A/\pi}$ and A is the area of outlet section; i.e. in a stacked manhole, area

of the opening between chambers and area of the exit pipe. Fig. 2.13 illustrates the water depth in chambers associated with different geometries in the outlet. The water depth inside manholes can be easily predicted independent on the shaft geometry if the outlet is not highly perturbed by the inlet flow. Inside typical drop manholes having 90^0 (angle between inlet and outlet axial directions), the dimensionless water depth $\sqrt{y/D_e}$ presented a close correlation with Q^+ (Fig. 2.14, the continuous line represents the best-fit line to measurements). Conversely, the water depth in shafts was reported to be correlated to inflow conditions inside manholes with 180^0 - angle between inlet-outlet directions (de Marinis et al. 2007).

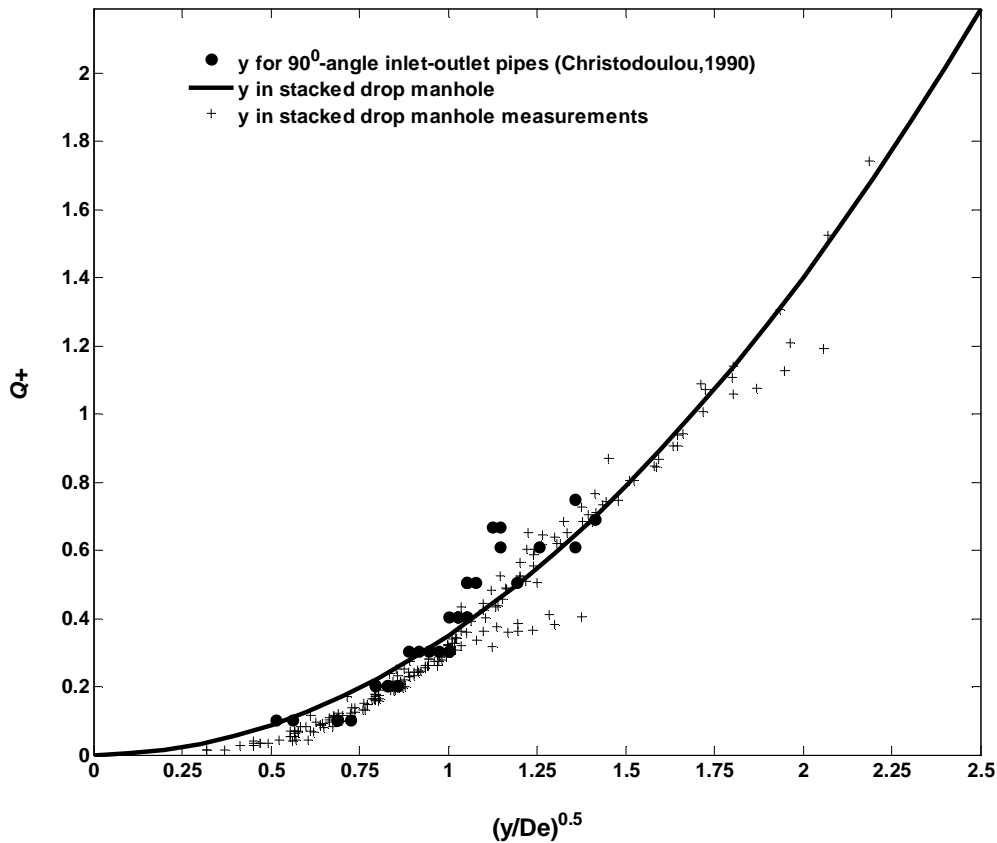


Figure 2.13 Comparison of depths of water in chamber

For small discharges, the water flowing through the outlet is not submerged. In the rectangular opening, the discharge is therefore expected to be a function of $y^{3/2}$ as in a

typical weir equation: $Q = C_D \frac{2}{3} \sqrt{2g} b_w y^{2/3}$. In Fig. 2.14, two weir equations ($C_D = 0.50$ and 0.40) are plotted in a dimensionless form and are compared to measurements at freefall condition in the opening. The series of data are clearly converging into straight lines in this arrangement, and they fall into two distinct lines due to individual discharge coefficients associated with each geometry. Since C_D is in fact a function of the discharge, for large Q^+ , few points do not fall in the constant- C_D weir equation.

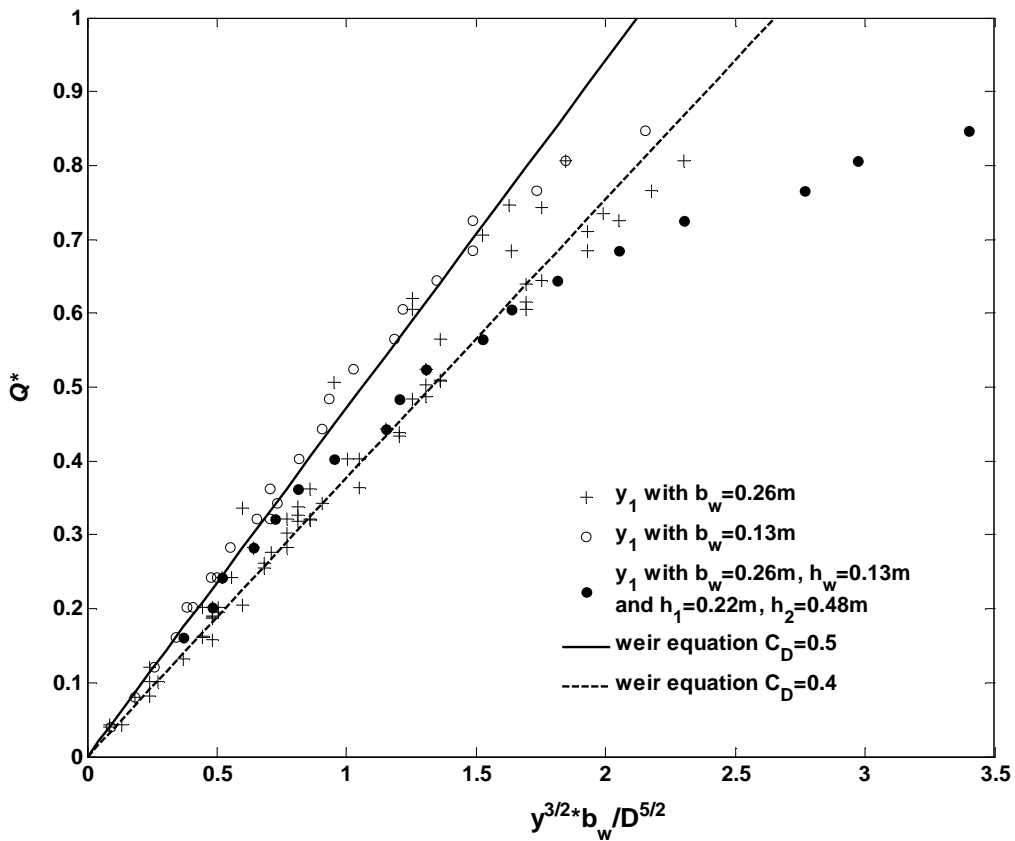


Figure 2.14 Non dimensional water depths in chambers in free fall regime

A more general classification of regimes can now be proposed for drop manholes regardless of its shaft (chamber) geometry; in which the water depth y in chamber is compared to the drop height h . 1) **Free overfall**, that is when $y \leq h$, will occur for $Q \leq C_D A \sqrt{2gh}$; where A is the outlet cross sectional area; 2) **Surface jet**, occurring

when $h < y \leq h + D$; where D = diameter of inlet section, is observed when $C_D A \sqrt{2gh} < Q \leq C_D A \sqrt{2g(h+D)}$; and, 3) **Submerged jet**, occurring when $y > h + D$, takes place correspondingly for $Q > C_D A \sqrt{2g(h+D)}$.

2.4 SUMMARY AND CONCLUSIONS

A shallow storm sewer system using stacked manholes was selected to resolve an elevation drop of 50 m in Windermere Subdivision in Edmonton, with a cost of about a quarter of a deeper storm sewer system. In this system, a novel design of drop manholes was applied to connect the sloping sewers and dissipate energy. This distinct design was built by stacking two identical chambers with an elevation drop between them. A detailed experimental investigation demonstrated that such a structure can achieve an energy dissipation of about 50 % to 90 % for the range of flow rates tested.

Given the uniqueness of the design, four distinctive regimes classified were related to the water depths in chambers and the particular geometry of the manhole. While the first regime (free overfall flow in both chambers) achieved an average energy dissipation of 86 %; the second regime (surface jet in chamber 2) diminished to about 70 %. The third (submerged opening from downstream) and fourth (fully submergence) regimes dropped to an average of 56 % and 45 % of total energy dissipation, respectively.

Evidently, the energy dissipation was associated with the inflow conditions, geometry of the design and outlet controls. However, small changes in the rectangular opening and drop heights in the chambers did not exhibit any significant effect on the global energy dissipation; a larger drop height in the second chamber apparently increased the energy dissipation achieved by that chamber. On the other hand, it was interesting to observe that at a constant Froude number the overall energy loss decreases with increasing discharge. Conversely, for a given discharge, an increase in Froude number showed an increase in the relative energy losses. In addition, a comparison

with typical drop manholes was done to assess the efficiency of energy dissipation in the stacked drop manhole.

The water depths inside the chambers of the structure were basically governed by the outlet controls and not directly dependent on the approaching flow conditions. A non-dimensional relationship was then established for predicting water depths based on the downstream control. Furthermore, a more general flow classification was proposed based on the water depth and the drop height inside a typical manhole for which the downstream controls are dominant.

This investigation has revealed a robust economical design option for hydraulic designers. The special configuration has proven adequate performance in terms of energy dissipation and water depths in chambers. Its potential applicability in outfalls was evident; hence, it is quiet appropriate to further investigate its attributes for standard usage.

References

- Calomino, F., Prega, G., Piro, P., and Veraldi, M.G. 1999. *Hydraulics of drops in supercritical flow*. 8 ICUSD, Sydney, Australia.
- Chamani, M.R., and Beirami, M.K. 2002. *Flow characteristics at drops*. Journal of Hydraulic Engineering-ASCE, **128**(8): 788-791.
- Chanson, H. 2004. *Hydraulics of rectangular dropshafts*. Journal of Irrigation and Drainage Engineering, **130**(6): 523-529.
- Chanson, H. 2007. *Air entrainment processes in a full-scale rectangular dropshaft at large flows*. Hydraulic Research, **45**(1): 43-53.
- Christodoulou, G.C. 1991. Drop manholes in supercritical pipelines. Journal of Irrigation and Drainage Engineering, **117**(1): 37-47.
- City-of-Calgary, T. 2000. Stormwater management and design manual. Wastewater and drainage. City of Calgary. Calgary.
- Clausnitzer, B., and Hager, W.H. 1997. Outflow characteristics from circular pipe. Journal of Hydraulic Engineering, **123**(10): 914-917.
- de Marinis, G., Rudy, G., Francesco, G. and H., H.W. 2007. Circular drop manholes. Preliminary experimental results. 32nd Congress of IAHR, Venice, Italy, IAHR.
- Delleur, J.W., Dooge, J.C., and Gent, K.W. 1956. Influence of slope and roughness on the overfall. J. Hydraul. Div. ASCE, **82**(HY4): 1038_30-1038_35.
- Dey, S. 2002. Free overfall in open channels: State-of-the-art review. Flow Measurement and Instrumentation, **13**(5-6): 247-264.
- Gargano, R., and Hager, W. 2002. Supercritical Flow across sewer manholes. Journal of Hydraulic Engineering, **128**(11): 1014-1017.
- Guo, Q., and Song, C.C.S. 1991. Dropshaft hydrodynamics under transient conditions. Journal of Hydraulic Engineering, **117**(8): 1042-1055.
- Hager, W.H. 1990. Vortex drop inlet for supercritical approaching flow. Journal of Hydraulic Engineering, **116**(8): 1048-1054.
- Hager, W.H. 1999. Wastewater Hydraulics. Theory and practice. Springer, Berlin. 628p
- Kusuda, T., and Arao, S. 1996. Energy losses at circular drop manholes. Proc. 7th Int. Conf. on Urban Storm Drainage, Hannover.
- Pedersen, F.B., and Mark, O. 1990. Head losses in storm sewer manholes: submerged jet theory. Journal of Hydraulic Engineering, **116**(11): 1317-1328.
- Rajaratnam, N., Mainali, A., and Hsung, C.Y. 1997. Observations on flow in vertical dropshafts in urban drainage systems. Journal of Environmental Engineering, **123**(5): 486-491.

- Rajaratnam, N., and Muralidhar, D. 1968. Characteristics of rectangular free overfall. *Journal of Hydraulic Research*, **6**(3): 233-258.
- Vischer, D.L., Hager, W.H. 1995. Vortex drops. Chap. 9. *Energy Dissipators: Hydraulic Structures Design Manual*. Balkema, A.A., Rotterdam, The Netherlands: pp. 167-181.
- Williamson, S. (2001). Drop structure design for wastewater and stormwater collection systems. Monograph 14. New York, Parsons Brinckerhoff Inc.: p.131.
- Zhao, C.-H., Zhu, D.Z., Sun, S.-K., and Liu, Z.-P. 2006. Experimental study of flow in a vortex drop shaft. *Journal of Hydraulic Engineering*, **132**(1): 61-68.

CHAPTER 3: HYDRAULICS OF SYMMETRIC STACKED DROP MANHOLES*

3.1 INTRODUCTION

Drop manholes are commonly used in urban drainage systems in order to reduce the slope of sewer pipes by allowing a drop at pipe junctions (i.e. manholes). Most municipality guidelines in North America restrict the height of drop manholes to about 1m (e.g. City of Calgary 2000). There is no theoretical or experimental basis supporting this limit except for the concern of excessive aeration and erosion in the drainage system. An effort to extend the drop height of standard drop manholes is pursued by investigating an alternative design herein. A stacked drop manhole (SDM) is constructed by stacking two identical drop manholes at an elevation difference (Fig. 3.1) (Camino et al. 2009). Such structures will allow the designers to extend the applicable range of the drop height.

Despite the extensive use of drop manholes in urban drainage systems, our understanding of their hydraulics is relatively limited. Local energy losses in drop manholes were studied firstly by Gayer (1984). The losses were correlated to a parameter that incorporates the inflow velocity and the drop height. Similarly, Christodoulou (1991) related the local losses and pool depths to a dimensionless number, so called drop Froude number F_D , which was essentially the same as the one proposed by Gayer. More recently, a detailed investigation was conducted on supercritical flows in circular drop manholes (Granata et al. 2010). Granata et al. (2010) were able to classify flow regimes based on the parabolic trajectory of the

* The content of this chapter has been published in the Journal of Irrigation and Drainage Engineering, ASCE as Camino, G.A., Zhu, D.Z. and Rajaratnam, N. (2011). "Hydraulics of stacked drop manholes." *J. Irrig. Drain. Eng.*, ASCE, 137(8): 537-552.

falling jet and the geometry of the shaft. They obtained empirical relations for local energy losses related to F_D as well as pool depths in terms of drop height, shaft diameter and flow rate. So far, however theoretical treatment of flows inside drop manholes supporting the empirical relations remains to be found.

Camino et al. (2009) conducted a model study on a special offset SDM for its construction in Edmonton, Canada. A sequence of stacked drop manholes was proposed instead of a large dropshaft of drop up to 50m. It was estimated that the SDM option was able to cut down the total cost by about 70% from the large dropshaft option of about \$1 million (Canadian dollars). Offset and symmetric SDM refer to the alignment of the inflow-outflow direction with the centerline of the opening section connecting the two chambers (Fig. 3.1). A symmetric SDM is proposed herein to extend previous results on the offset design to a more compact and simplified arrangement that could help to standardize its usage.

The US Army Corps of Engineers (USACE 1997) advise that drop structures for vertical conveyance should dissipate the energy associated with the elevation drop, remove the air entrainment associated with the falling jet and impinging flow, and minimize head losses when the tunnels are surcharged. Furthermore, pool depths inside the chamber shafts should be assessed to avoid overflows in urban drainage systems. This experimental investigation systematically examines the effect of: 1) inflow conditions; 2) pipe elevation differences; and, 3) passage between chambers, on the energy head of the outgoing flow and pool depths in chambers to secure proper hydraulic performance. Flow regimes in the offset SDM study were related to the water levels in chambers; i.e. based on downstream conditions (Camino et al. 2009). Flow regimes in a symmetric SDM combine the effect of both inflow and outflow controls. A critical flow condition associated with pool depths was recognized and a theoretical treatment based on the integral momentum equation is pursued. In addition, a fully surcharged state is recreated by imposing a downstream pressure. Detailed velocity profiles at the horizontal center plane of the opening are measured under surcharged flow and energy loss coefficients are obtained. Finally, bulk air

flows are measured in a large height SDM (drop height $h = 8D$, where D is the inlet pipe diameter) and compared with drop structures of comparable drop height. Overall, this study aims to assess the performance of SDMs and at the same time further our understanding on flows inside drop manholes.

3.2 EXPERIMENTAL PROGRAM

Experiments to test major design parameters of an SDM were focused on a model of a symmetrical SDM (Fig. 3.1b). The experiments investigated the effect of drop height, passage between chambers and the pressure in the outlet pipe on the energy loss, pool depths and air flows. Additional experiments were conducted in an offset SDM, with equal configuration as the Windermere model (Camino et al. 2009). This part of the study investigated the effect of the alignment between the opening in-between chambers and the inlet-outlet longitudinal axis. A model structure of a symmetric SDM was built using Plexiglas and transparent pipes. Two chambers with identical squared geometry ($3D$ -width by $3D$ -length where D refers to the inlet and outlet pipe diameters of 0.19m) were mounted at two drop heights h_1 and h_2 ; and a rectangular opening was located connecting the chambers. A flow straightener was inserted right after a jet-box in the inlet conduit to avoid flow concentrations and set an inflow depth independent of the flow rate (Gargano and Hager 2002).

Piezometer taps of 1.6mm diameter were drilled at 0.28m intervals ($1.5D$) in the inlet and outlet pipes. Pool depths were recorded at six locations in each chamber. When the water levels were unevenly increased by localized jet impingement, pool depths were averaged at less perturbed locations, i.e., behind the falling jet. While water flow rates (up to 60L/s) were recorded with a magnetic flow meter, the air flow rates were obtained from air velocity measurements using a hotwire anemometer (Omega Model HHF42, www.omega.com). Two air vents were fitted in two air tight lids at the top of each chamber for that purpose. The accuracy of the device was 1% of the full scale or 5% of the measurement. Water velocities were recorded in certain locations using a Prandtl tube of 3mm diameter or a SonTek MicroADV of 50Hz (www.sontek.com) as

appropriate.

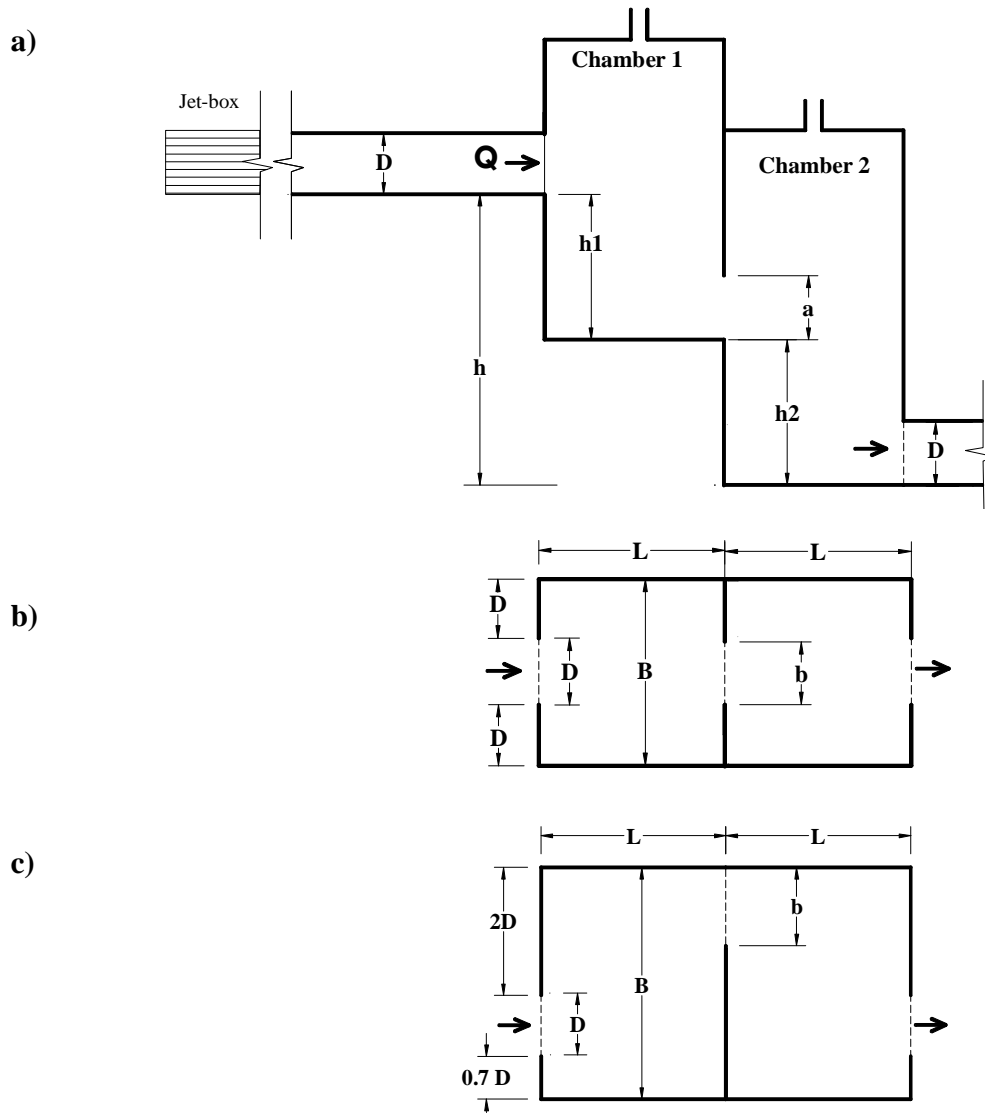


Figure 3.1 Setup of a SDM: a) Sectional view; b) Plan view of a symmetric SDM; c) Plan view of an offset SDM

The experiments consisted of four series with a total of 300 runs (Table 3.1). About 250 runs were tested in a symmetric design and remaining runs on the offset design. Series A concentrated on the effect of drop heights in a symmetric design. The effect of plunging pool depth was studied by resizing the opening section in series of experiments B. Series C observed the effect of the downstream end pressure by using a butterfly valve at the end of the outlet conduit. Finally, series D considered the

effect of the offset alignment of the opening with respect to the pipes axis.

Table 3.1. Summary of experimental conditions

Series	Alignment	L x B	h	h ₁	h ₂	a	b	Valve
			8D	4D	4D			
A	Symmetric	3D x 3D	6D	4D	2D	D	D	open
			4D	2D	2D			
B	Symmetric	3D x 3D	8D	4D	4D	0.5D	D	open
C	Symmetric	3D x 3D	4D	2D	2D	D	D	½ open
D	Offset ⁺	3.2D x 4D	3.7D	1.8D	1.8D	1.36D	1.36D	open

+ A second offset arrangement was tested having an increased diameter in the outlet pipe to $D_{out}=1.25D$

3.3 FLOW PATTERNS AND REGIMES

3.3.1 First Chamber

Flow patterns inside the first chamber of a SDM are analogous to the ones in plunging dropshafts (Chanson 2002). Three flow types are distinguished in the first chamber of the SDM based on the inflow impingement location and chamber geometry. A **Regime I** (RI) refers to a drop type flow which is observed at small flow rates. RI is featured by a free falling jet from the inflow maintaining partially full flow through the opening between chambers and outlet pipe (Fig. 3.2a). A **Regime III** (RIII) refers to a dropshaft type flow and is characterized by an inflow jet impinging on the front wall (Fig. 3.2c). Often, RIII is observed in large plunging

dropshafts due to its slender shaft geometry. A transitional **Regime II** (RII) is recognized between regime I and III when one or both nappes of the falling jet impinged in the surroundings of the in-between opening (Fig. 3.2b).

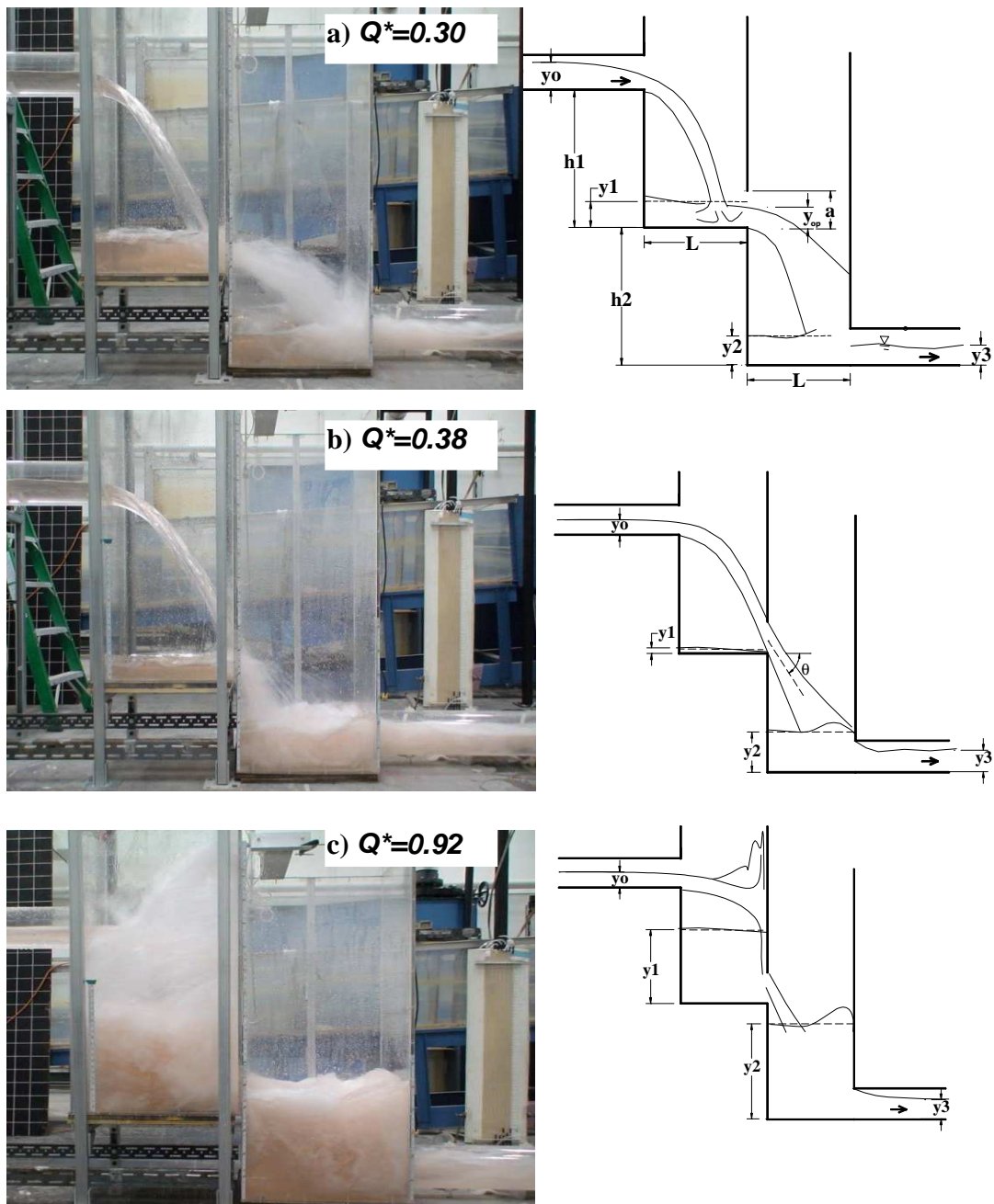


Figure 3.2 Flow types: a) Regime I. Drop flow; b) Regime II. Transitional flow; c) Regime III. Dropshaft flow

A plot of dimensionless pool depths y_l/D_e with respect to a dimensionless discharge $Q^* = Q/\sqrt{gD^5}$ is shown in Fig. 3.3; where $D_e = (4A_w/\pi)^{1/2}$, A_w is the area of flow across the rectangular opening, and g is the acceleration due to gravity.

Fig. 3.3 illustrates that small pool depths in RI get further reduced as the upper nappe of the inflow jet approaches the opening. Fully conveyance of the inflow jet across the opening (RII) shows minimum water depths. Pool regains depth as the lower nappe leaves the opening with increasing flow rate and at a faster pace. A transitional regime prevails over larger range of flow rates for small h/L ratios and larger opening heights; L refers to the length of each chamber.

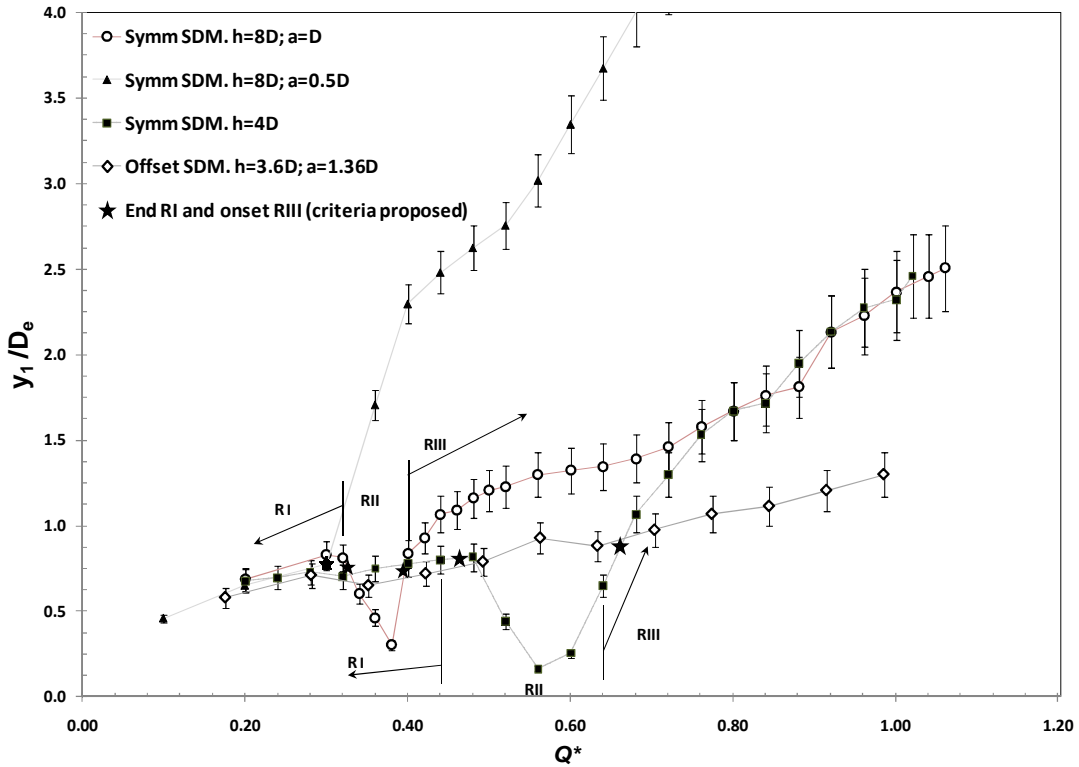


Figure 3.3 Dimensionless pool depths inside the first chamber of a SDM

Transitional regime (Regime II) could serve as dividing criteria of more distinctive Regimes I and III. The trajectory of a free falling jet from a circular conduit was correlated experimentally by Clausnitzer and Hager (1997) with the approaching Froude number, water depth and end depth in inflow. Assuming a simple parabolic

trajectory, RII occurs when $h_1+(y_o/2-a/2)$ approaches $C_I(g/2)(L/V_o)^2$ where h_1 is the drop height of the first chamber, y_o is the inflow water depth, V_o is the inflow velocity, a is the opening height and C_I is an experimental coefficient. From experiments, C_I below 0.8 produced RI flows, and C_I above 1.4, RIII flows in the SDM. Values of C_I of 0.6 and 1.5 were obtained for corresponding conditions in circular drop manholes (Granata et al. 2010) and 0.505 and 1.01 in rectangular dropshafts with subcritical inflows and $h/L=1.683$ (Chanson 1998), neglecting the difference $(y_o/2-a/2)$. This approach could be further refined accounting for the upper and lower nappes of the falling jet, the residual pressure and velocity profiles at the end section, the jet thickness contraction and the pool depth. Yet, for practical purposes the expression is kept in its simplest form.

3.3.2 *Second Chamber*

Flow patterns inside the second chamber are linked to upstream conditions and outflow controls. Due to the initial turbulence intensity and aeration level, the flow out of the opening between chambers disintegrates shortly after leaving the opening section. After impingement, regime I flow in the first chamber gets deflected horizontally towards the opening and into the second chamber. As the upper nappe of inflow approaches the opening (RII), the flow through the opening gets immediately deflected down about 30° angle (θ is the deflected angle of the outflow from the opening with the horizontal; see Fig. 3.2b). Finally, regime III flow in the first chamber gets deflected at the entrance to the second chamber into θ between 60° to 40° (Fig. 3.2c).

Once the outlet entrance gets submerged from the upstream pool depth, two conditions are of practical interest: 1) when the outflow runs as full pipe flow; and, 2) when an orifice type of flow is developed in the outlet pipe (Fig. 3.4). Zhao et al. (2004) argued that the transition from full pipe flow into orifice flow in junction manholes was independent of the outlet slope; instead, it was induced by the inlet waves formed at the entrance to the outlet pipe. Similar disturbances, yet more drastic due to the elevation difference are relevant in this transition in the second chamber of

a SDM. A swell is formed when the jet discharges into the second chamber and hits its bottom. A full pipe flow at the exit is prone to develop when swells are observed. Thus, the angle of deflection of the flow issued from the in-between opening appears to be a significant feature in the transition from orifice flow to full pipe flow. An oscillatory state between a full pipe flow and partially full flow was observed in a small height SDM ($h=4D$) at $Q^*=0.90 \sim 1.00$ for about 30 secs every 180 secs.

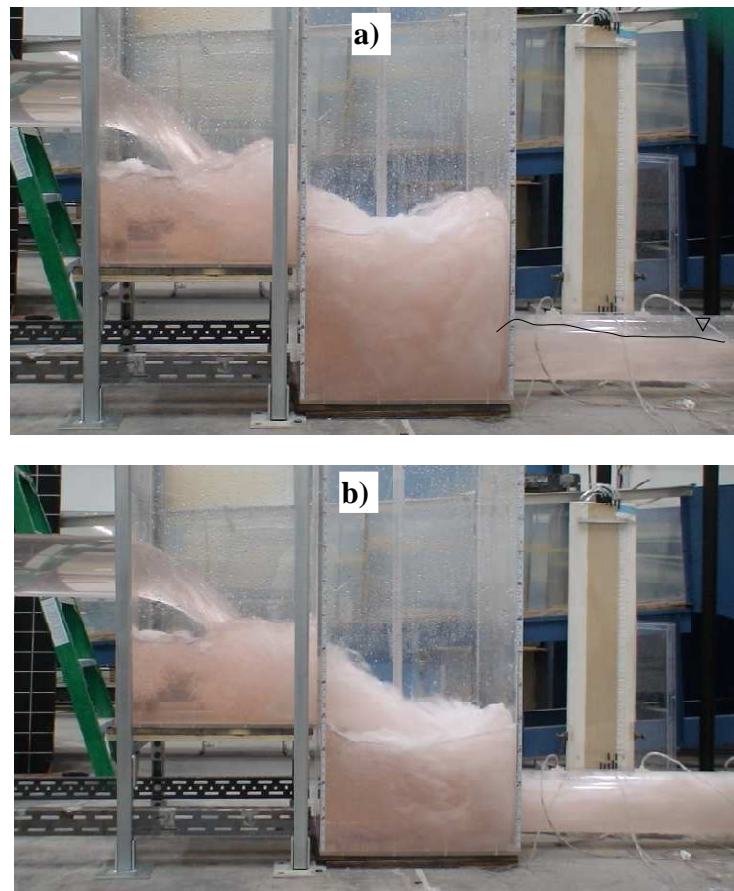


Figure 3.4 Two flow regimes in the second chamber of a small height SDM: a) orifice flow in outlet at $Q^*=0.92$; b) full pipe flow in outlet at $Q^*=0.96$

A fully surcharged flow regime could appear when the water surface in the chambers rises above the pipes crowns and the opening between chambers. Even though, there is a close connection between surcharged flows in drop manholes and in straight-through or combining junction manholes, the latter has received significantly more

attention. Extensive velocity and pressure distributions were measured and mapped inside combining junctions (Ramamurthy and Zhu 1997; Shumate and Weber 1998; Zhao et al. 2006). From these investigations, flow patterns, separation zones and regions of highest turbulence intensities are well defined in combining junctions.

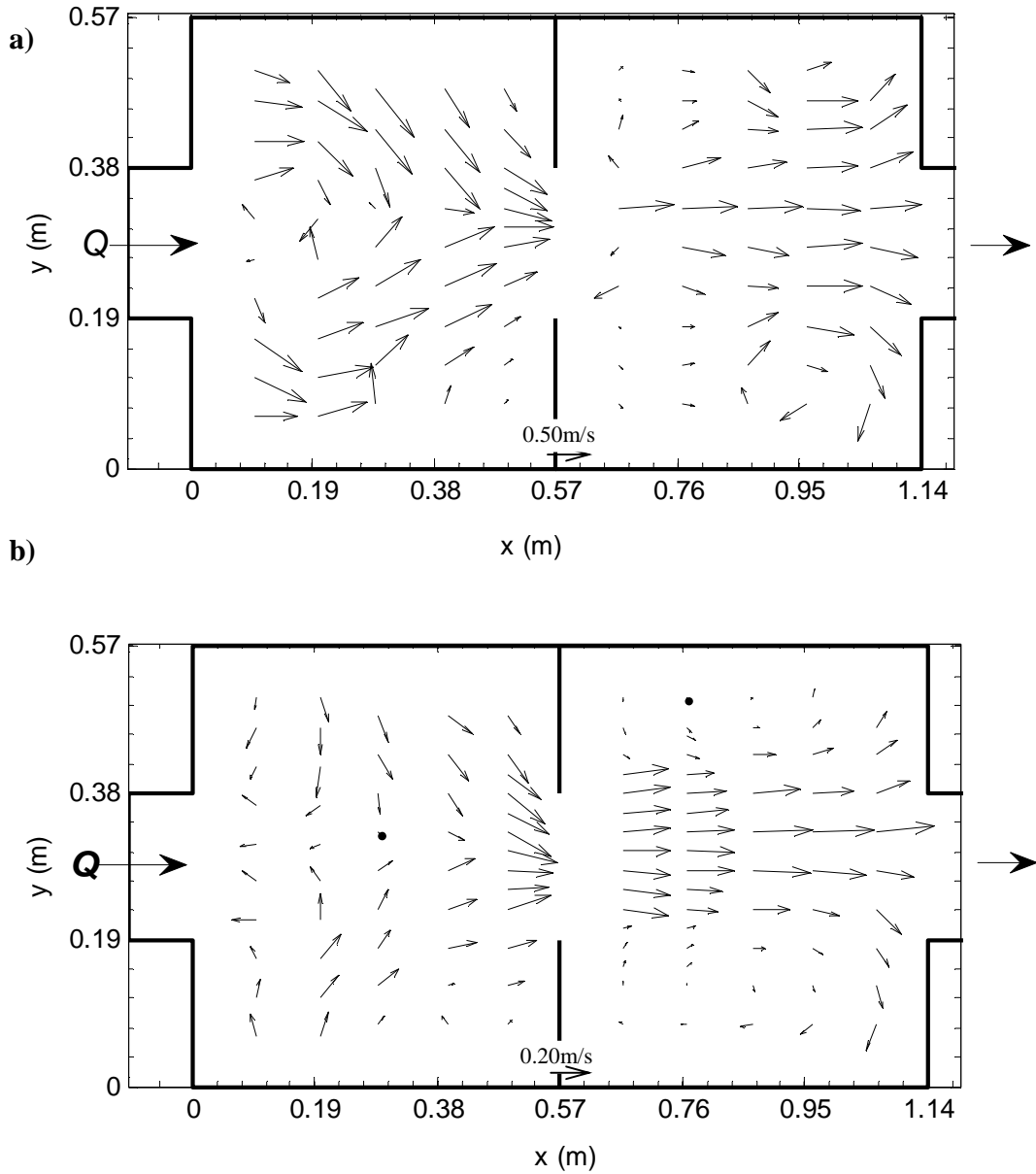


Figure 3.5 Velocity distribution of a fully surcharged flow on the horizontal center plane at the level of the opening section between chambers. a) $Q^*=0.80$; b) $Q^*=0.38$

The two plots in Fig. 3.5 show clearly the convergence of the flow to the opening between chambers. The jet from the opening can be observed to diffuse as it approaches the outlet creating zones of recirculation on both sides. The flow is reasonably symmetrical about the central plane. In addition, experimental measurements of velocity and pressure profiles of the jet out of the opening are plotted in appendix 3.A; i.e. Figs. 3.14 and 3.15 for free falling flow (RI) and fully submerged flow across the opening, respectively.

3.4 THEORETICAL FRAMEWORK

Large pool depths develop under a dropshaft type flow (RIII), inside the first chamber of a symmetric SDM (Fig. 3.2c). While this condition can be considered critical in terms of pool depths for the first chamber, an orifice flow in the outlet pipe is for the second chamber. Predictions on pool depths could be made by applying the integral momentum equation in control volumes CV_1 and CV_2 along the longitudinal axis x (Fig. 3.6).

3.4.1 *First chamber under a dropshaft type flow*

Under regime III, the inflow jet hits the front wall and is deflected along the wall forming a splash upwards and a main flow sliding down. The major component of the deflected jet is in the vertical direction. Provided that the inflow is free falling and hitting on the front wall, the pool depth in the first chamber y_1 could be derived from the momentum equation in CV_1 (Fig 3. 6a) in Eq. [3.1]:

$$[3.1] \quad F_{1u} - F_{1d} - F_w = \rho Q V_{wx}$$

where F_{1u} and F_{1d} represent the pressure forces on the upstream and downstream walls of CV_1 and F_w , the pressure force at the vena contracta of the flow out of the opening between chambers. V_{wx} is the x -component of the mean flow velocity at the vena contracta. Noteworthy is that CV_1 refers to the volume below the impingement zone. A normalized pool depth y_1/D_e is derived in Eq. [3.2] from the momentum

analysis detailed in appendix 3.B.

$$[3.2] \quad y_1 / D_e = \left(-1 + \sqrt{1 + \left(\frac{1}{\varphi_1} - 1 \right) \left(1 + \frac{2 \cos \theta}{a \varphi_1 C_c} \frac{Q^2}{g A_w^2} \right)} \right) / \left(\frac{D_e}{a} \left(\frac{1}{\varphi_1} - 1 \right) \right)$$

Where φ_1 is a coefficient relating the effective to hydrostatic pressure force; a is the height of the opening; and, C_c is the contraction coefficient relating the area of the vena contracta to the area of flow across the opening A_w .

3.4.2 Second chamber for submerged flow with orifice outflow

Zhao et al. (2004) established a distinction in surcharged junction manholes between an orifice flow at the exit of the junction-chamber with open-channel flow in the outlet pipe and a full pipe flow in the outlet pipe. Even though, they demonstrated that the flow structure inside the pool was basically unchanged under both situations, the water surface elevation was appreciably affected by the outflow type as it happens in the second chamber of a SDM. Zhao et al. provided evidence that the most critical condition considering the water level in a surcharged manhole is observed when an orifice flow is featured in the outgoing flow.

The momentum equation in CV_2 (Fig. 3.6b) yields an expression for the pool depth in the second chamber (Eq. [3.3]), provided that the flow exiting the first chamber is not submerged, and an orifice flow in the outlet pipe is maintained. The details of the derivation are illustrated in appendix 3.B.

$$[3.3] \quad \frac{y_2}{D} = \left(-1 + \sqrt{1 + \frac{2D}{A} \left(\frac{1}{\varphi_2} - 1 \right) \left(\frac{Q^2}{g \varphi_2 A^2} \left(\frac{1}{C_{c3}} - \frac{\cos \theta}{C_c} \frac{A}{A_w} \right) + \frac{D}{2} \left(\frac{C_{c3}^{2.2}}{\varphi_2} + 1 \right) \right)} \right) / \left(\left(\frac{1}{\varphi_2} - 1 \right) \frac{D^2}{A} \right)$$

where $A = \pi D^2 / 4$, C_{c3} is the contraction coefficient of the outgoing flow; and, φ_2 is a second coefficient relating the effective to hydrostatic pressure force.

Once the contraction coefficients C_c and C_{c3} and the effective pressure coefficients φ_1 and φ_2 are rationally assumed, pool depths in the chambers for the conditions established can be computed with Eqs. [3.2] and [3.3]. To find the values of C_c , a square chamber (0.38m x 0.38m) was constructed of plexiglass. A dropshaft type flow was simulated by a vertical inlet pipe attached to the wall where an orifice was situated flush with the bottom of the chamber. The outflow was issued freely into the air. The inlet pipe was located within few millimetres below the water surface to avoid air entrainment that prevented measurements in the SDM under RIII. Three velocity profiles were measured with a Pitot tube at the falling jet out of the orifice; from which the values of velocity coefficients $C_v = 0.97, 0.79$ and 0.76 for $Q^*=2.8, 1.9$ and 1.6 were computed. Similarly, values of discharge coefficient $C_d = 0.62, 0.59$ and 0.62 were directly computed from its definition. Considering $C_c = C_d/C_v$, a mean value of $C_c=0.7$ was obtained which compared fairly well with the mean of direct measurements of $C_c= 0.75 \pm 3.4e-2$ using a point gauge. The angles of deflection θ varied between 60° and 40° in the flow out of the opening of the SDM; a value of $\text{Cos } \theta = 0.64$ was adopted for the computations.

Smith (1995) proposed a value of contraction coefficient of 0.7 for orifice flow in circular-pipe culverts with a square-edged entrance. Zhao et al. (2004) measured values between 0.7 and 0.8 in orifice flows out of a junction chamber. In the present experiments values of C_{c3} between 0.45 and 0.75 were measured. An average value of 0.6 was used. Finally, a pressure force on the front wall was considered equivalent to the force on a sluice gate. Roth and Hager (1999) proposed an experimental expression for the ratio of effective to hydrostatic pressure forces:

$$[3.4] \quad \varphi_{1,2} = 0.75 + 0.25 \exp\left(-2.15(d/y)^{1.15}\right)$$

where d is the gate opening and y the approach flow depth . Considering d equal to the height of the opening and y as y_1 the pool depth, mean value of $\varphi_1=0.87$ and $\varphi_2 = 0.90$ were computed.

Predictions on pool depths are compared with measurements in Fig. 3.7. The pool depths derived in Eqs. [3.2] and [3.3], pursuing a purely hydraulic approach, are theoretical depths of unaerated flow. Falvey (1980) states that the observed flow depth of the air-water mixture (y_b) in drop structures could be decidedly different than a flow depth with no aeration. In a SDM not only a number of air entrainment mechanisms are present but also large bubble residence times are observed. Photographs from a high-speed camera at a side wall of the chambers were used to get average void fractions based on the relative area occupied by the respective phases. Estimations of air trapped within the turbulent vortical structures inside the chambers were gained from the sectional void fractions.

When assuming an even distribution of air throughout the water flow, the depth of the mixture could be predicted based on the air concentration C (Falvey 1980); that is, $y_b/y = 1/(1-C)$. The actual pool depths in the SDM; i.e. corresponding to the air-water composite, denote an increase of 1.8 and 1.25 with respect to the theoretically derived depths for the first and second chamber, respectively. As these factors relate measured to computed depths, they also account for additional simplifying assumptions made in the model, such as disregard of bed and wall frictional resistance, horizontal momentum from the water veil on the side walls or forces due to jet impingement below the pool. Note that the predicted pool depths do not consider the splash formed at impingement. A free board of about $2D$ above the inlet pipe is recommended for supercritical inflows.

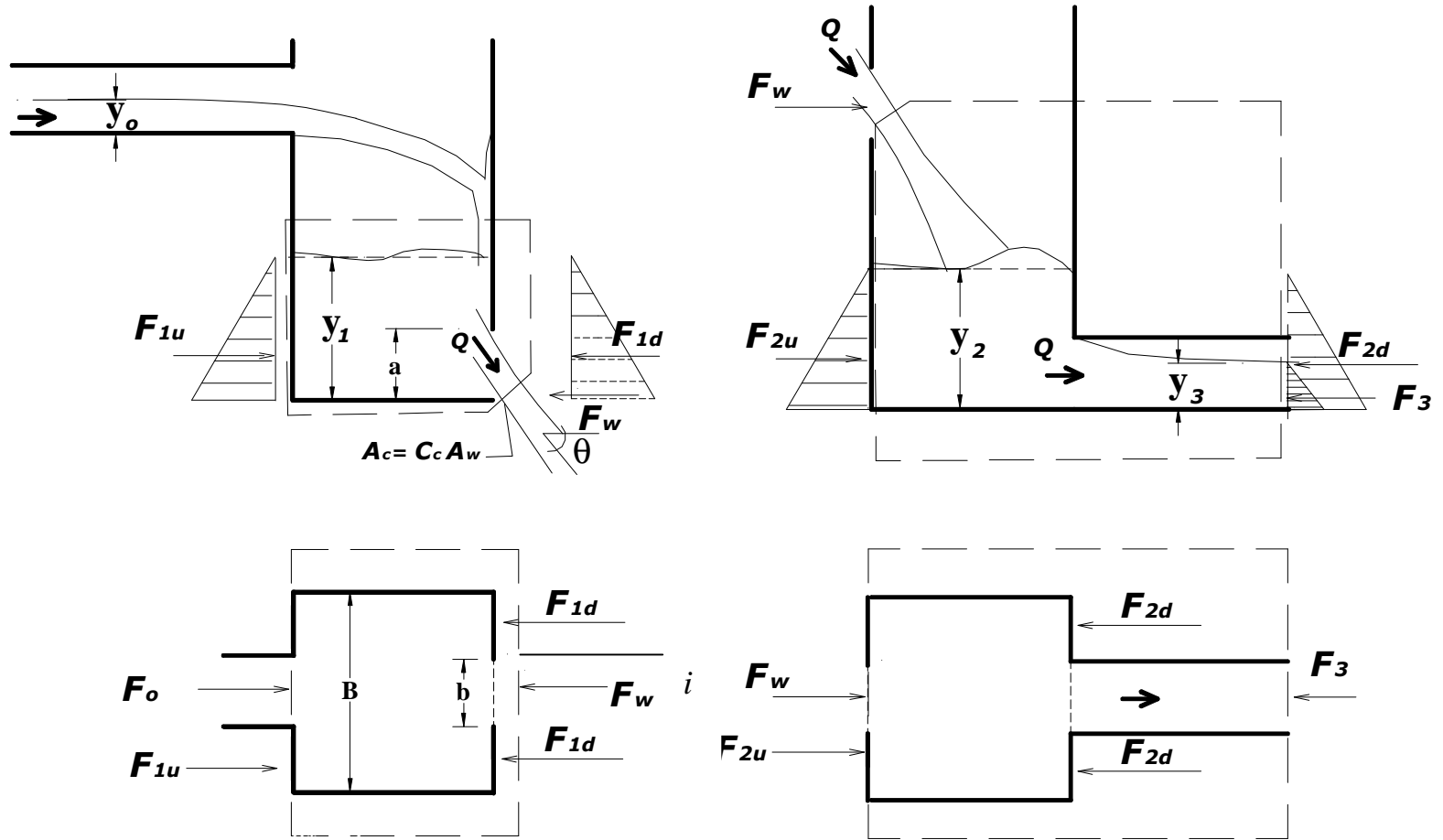


Figure 3.6 Control volumes in a SDM: a) first chamber (CV_1); b) second chamber (CV_2)

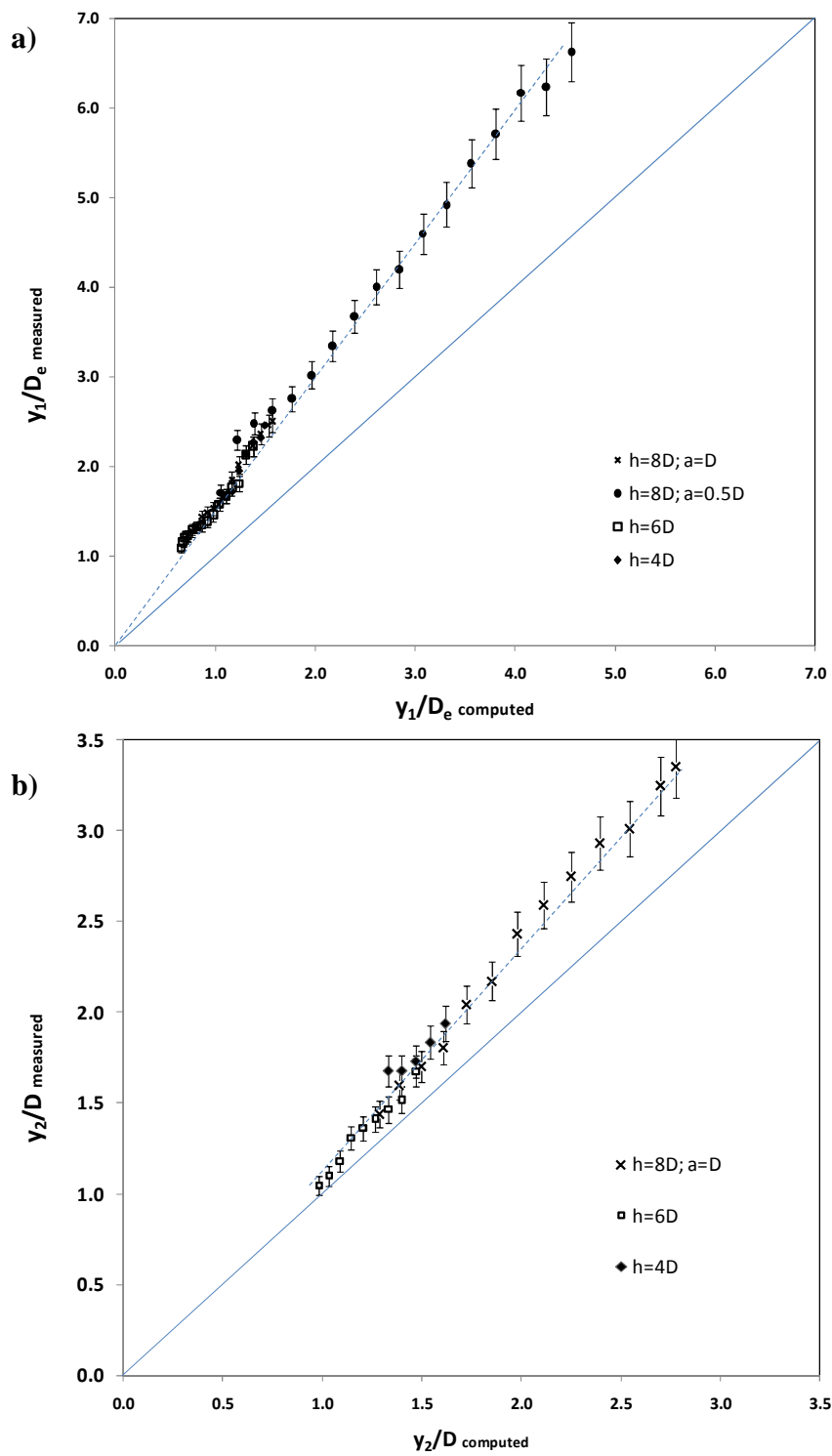


Figure 3.7 Predictions on non-dimensional pool depths in: a) the first chamber and, b) the second chamber

3.4.3 Orifice flow equation

Interestingly, from the momentum equation, pool depths are related to the square of the flow rates. Expressed in a dimensionless form, $\sqrt{y_1/D_e}$ is directly proportional to $Q^+ = Q/\sqrt{gD_e^5}$. Fig. 3.8a shows a linear relation of $\sqrt{y_1/D_e}$ with Q^+ for all experiments under RIII. This relation could be expressed as a classical orifice flow equation: $Q = C_d A_w \sqrt{2gy_1}$ where C_d is the discharge coefficient. Fig. 3.8b illustrates the dependence of C_d on a dimensionless pool depth D_e/y_1 in direct association to flows under sluice gates for both free flow and submerged flow conditions (Rajaratnam and Subramanya 1967). Values of C_d for small opening heights ($a=1/2D$) are in the upper range 0.61 to 0.42 and for large opening heights ($a=D$), between 0.45 and 0.28. Three points in a surcharged regime show an almost constant value in the upper range.

A more general relation of C_d could be derived from an energy equation between section i (Fig. 3.6a at vertical inflow jet right before plunging) and the vena contracta of the jet out of the opening as illustrated in appendix 3.C. Solving the energy equation simultaneously with the continuity equation yields:

$$[3.5] \quad C_d = C_c C_v / \sqrt{\alpha_c - C_c^2 C_v^2 (A_w/A_o)^2}$$

where α_c is the kinetic energy correction factor. While α_c could be assumed close to unity for free jets; the velocity coefficient C_v , A_w/A_o and C_c are likely to be affected by y_1/D_e which is expressed by the experimental relation $C_d = -0.39(D_e/y_1) + 0.63$ obtained in Fig. 3.8b.

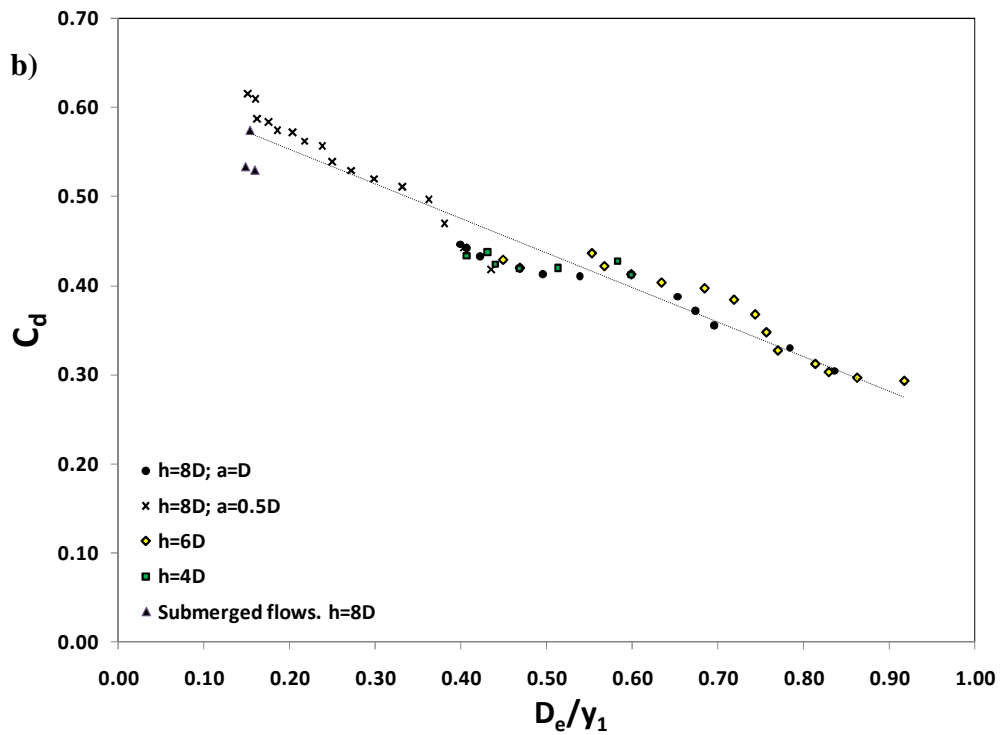
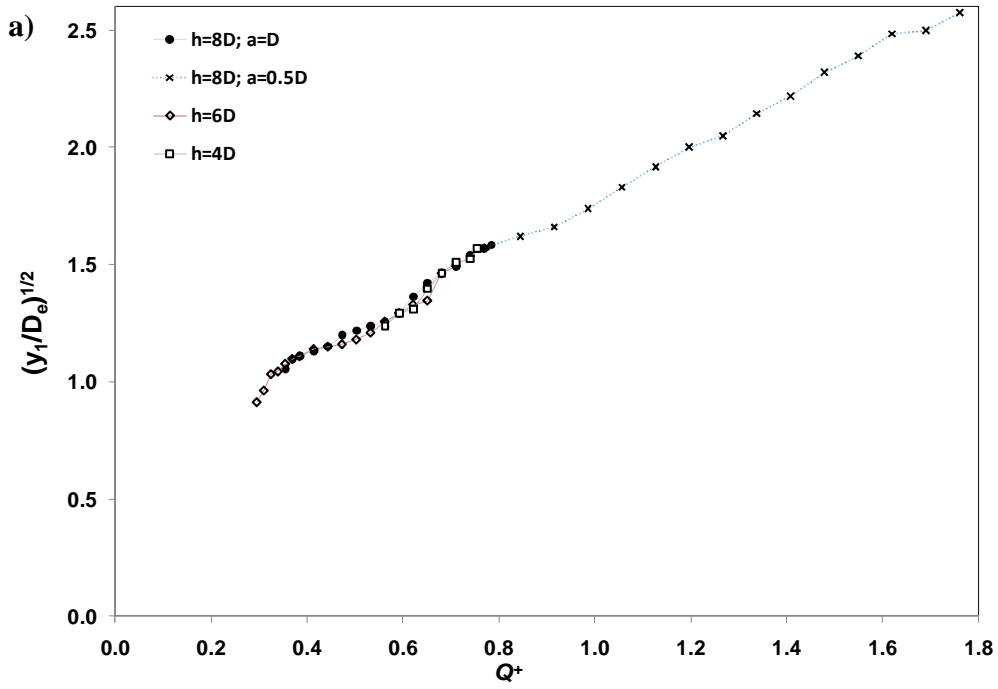


Figure 3.8 a) Dimensionless pool depth in the first chamber for all runs under RIII; b) discharge coefficient in the outflow of first chamber of symmetric SDMs

3.5 ENERGY DISSIPATION

Major energy losses inside SDM are caused by a) jet impingement on chamber boundaries; b) recirculating flows inside the chambers; c) plunging jets into pools; and d) abrupt transitions created by contractions and expansions of the geometry of the manhole. The head losses in a stacked drop manhole are defined as:

$$[3.6] \quad \Delta H = H_o - H_3$$

where: $H = z + y + \alpha V^2 / 2g$ is the total head, z is the invert elevation above the datum, y the water depth, V the mean velocity and α , the kinetic energy coefficient for non-uniform flow. This last coefficient is assumed to be unity in inflow and outflow sections. The subscripts 0 and 3 correspond to inlet and outlet sections. The datum is fixed at the level of the invert elevation of the outlet pipe.

The overall efficiency on energy dissipation of SDM, expressed by $\eta = \Delta H / H_o$, ranges between 70 to 95% (Fig. 3.9). A mild decrease of the relative energy loss with an increase in flow rate is perceived in all series. An examination of the energy terms revealed that more than 90% of the elevation head (i.e. the drop height) and about 50% of the inflow velocity head is lost within the structure. From the momentum analysis, some predictions on the energy loss could be made when the entrance to the outflow is submerged and an orifice flow is featured in the outlet conduit (Fig. 3.9). The residual energy is then given by: $H_3 = C_{c3}D + Q^2 / 2g (C_{c3}A)^2$. This approximation is restricted to the critical condition in the second chamber and is sensitive to the contraction coefficient C_{c3} . Alternatively, a linear fit between a non-dimensional energy head loss and a non-dimensional kinetic energy head for all experimental series is illustrated in Fig. 3.10. Same linearity was also found in circular drop manholes (Granata et al 2010); although less of the kinetic energy from the inflow was lost on average in a circular drop manhole than in a SDM.

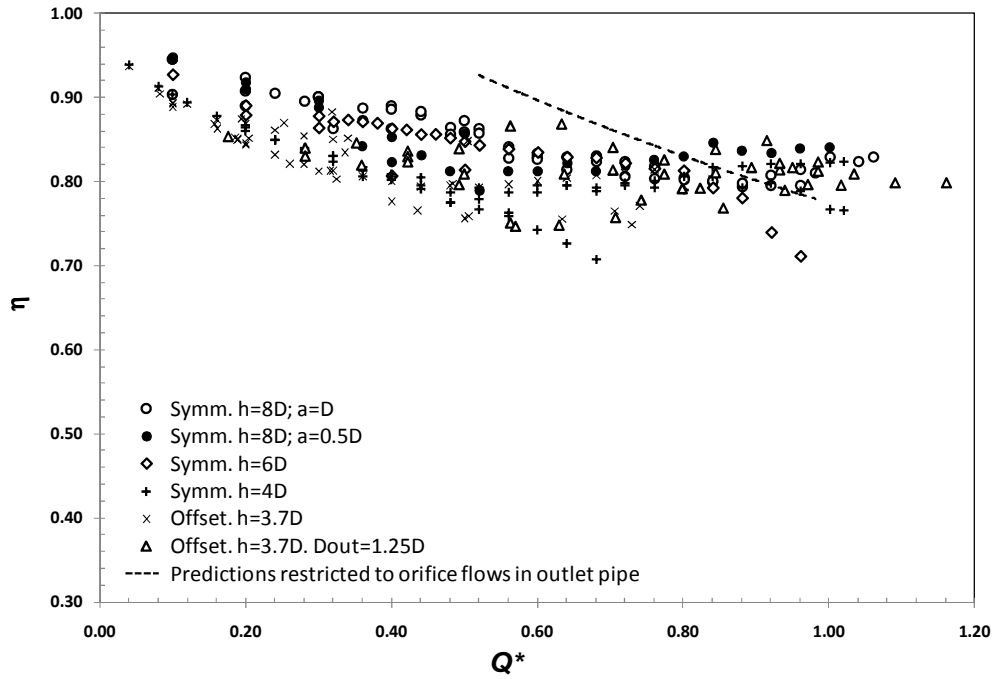


Figure 3.9 Relative energy losses inside SDMs of diverse configurations with respect to Q^*

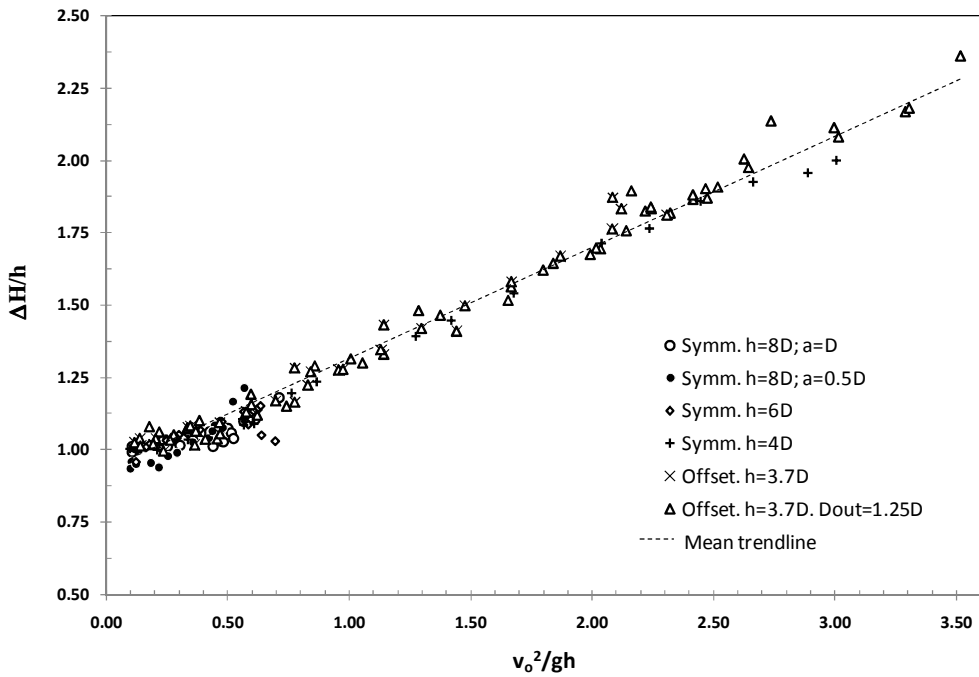


Figure 3.10 Dimensionless energy losses as a function of dimensionless velocity head in SDMs

Considering a local loss coefficient K , defined by $K=(H_o-H_3)/(V_o^2/2g)$, a single

relation was found for all configurations of drop manholes and SDMs (Fig. 3.11) with the drop Froude number F_D (Gayer 1984; Christodoulou 1991; Hager 1992). This parameter characterizes the inflow velocity V_o with the gravity action over an elevation drop h by $F_D=V_o/(gh)^{1/2}$. F_D in SDM is computed considering h as the total elevation drop. A close correlation was obtained between K and F_D in an offset (Camino et al. 2009) and symmetric configurations (Fig. 3.11). Interestingly enough, rectangular open-channel drops, studied extensively (Moore 1943; Rajaratnam and Chamani 1995; Chamani and Beirami 2002), are also a function of this parameter (Fig. 3.11). An empirical equation was fitted for different configurations of SDMs:

$$[3.7] \quad K = 0.75 + 1.90(1/F_D)^2$$

More physical insight can be gained expressing Eq. [3.7] as:

$$[3.8] \quad \Delta H = 0.75V_o^2 / 2g + 0.95h$$

Eq. [3.8] shows that on average about 75% of the approaching kinetic energy and 90% of the elevation head is lost within the structure which agrees well with the analysis done on each energy term. A close inspection of each series of experiments revealed that the actual amount of kinetic energy lost in the structure depends on the drop height, being larger for smaller drop height SDM. Only about 40% of the kinetic energy is dissipated in the large SDM ($h=8D$) and up to 80% in the small SDM ($h=4D$).

It is obvious that in a surcharged regime the first term of Eq. [3.8] has no contribution to the loss as the approaching kinetic energy is equivalent having both pipes full. Instead, losses due to abrupt changes in the geometry of the SDM become important. When the manholes get surcharged, it is advantageous to minimize the energy losses as not to back up water into tributary sewers. Very little work has been done on surcharged flows in drop manholes. Kusuda and Arao (1996) studied the energy losses in circular drop manholes with bell-mouth and squared-edged exits under

surcharged conditions. Their experimental study showed maximum loss coefficients close to 2.0 for square-edged exits.

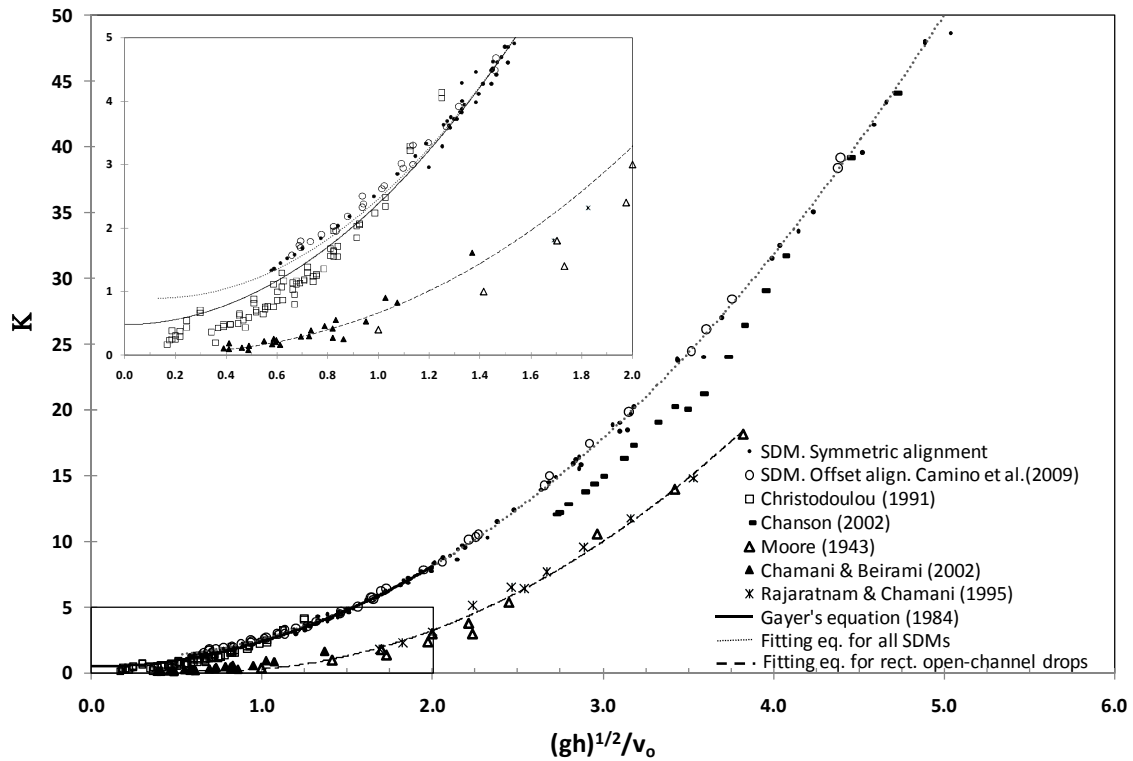


Figure 3.11 Local head coefficients related to the drop Froude number

As compared to surcharged rectangular junctions, the chambers of a surcharged SDM show larger losses possibly due to the rectangular opening in between the chambers; which resembles an orifice plate when submerged. Loss coefficients of $K=0.20$ in surcharged squared junctions of $L=3.3D$ were reported by Sangster et al. (1958). Marsalek (1984) obtained $K=0.334$ for a $L=2.26D$ squared junction; while Zhao (2004) reported $K=0.596$ for a junction with $L=3D$ having 5cm bottom sump. The joint loss in the two chambers of a SDM should add to an upper limit value of 1.2. Needless to say that losses in a surcharged SDM can also be estimated by the combined action of entrance loss ($K=1.0$), exit loss ($K=0.5$) and loss due to the opening; which is largely dependent on the level of submergence. The SDM was tested under surcharged flow by imposing a downstream pressure of half closure of

the valve located at the end of the outgoing pipe. Average loss coefficients of $K=2.7$ for the SDM of large opening height and $K=6.4$ for the SDM of small opening height were registered in those tests.

3.6 AIR ENTRAINMENT

The bulk air demanded by a drop manhole is a product of the combined action of mechanisms of air movement, air entrainment and air release. Edwini-Bonsu and Steffler (2006) recognized that a manhole could act as a source of fresh air or eventually as an escape of odorous disturbances. The relative importance of different processes affecting the interaction air-water will define an overall balance. In general, drop manholes could introduce air into the system by mechanisms including: 1) air drag by the falling jet or air boundary layer formation; 2) air entrainment by jet impingement on the boundaries of manhole and/or plunging into the water pool; and, 3) free surface aeration due to surface disturbances of the cushion pool. As compared to dropshafts, mechanisms associated to air drag may not be as significant due to the smaller drop height of the SDM. However its relative contribution could increase considerably when the outlet runs partly full. In this latter case, the water flow drives an air flow in the outflow headspace (Gargano et al. 2008).

Plunging and impinging jets may be the most significant aeration processes inside the SDM. Air flows measured inside the large height SDM are reported in terms of the dimensionless air discharge Q_a/Q , Q_a being the air flow rate and Q the water flow rate (Fig. 3.12). Overall, the dimensionless air flow was high for small water flow rates decreasing as Q^* increases. Deeper plunge pool in the first chamber is produced by reducing the opening height from D to $0.5D$. Apparently when the impinging mechanism is predominant, larger air entrainment occurs. The plunging air mechanism may entrain less air comparably due to smaller velocity of the jet as the pool depth reduces the drop height. In addition, deeper water cushion allows air bubbles to be released back to the chamber; hence less air is transported to the downstream conduit as is illustrated in Fig. 3.13. Air demand in the second chamber

of an SDM of large opening ($a=D$) were less than in the first chamber as the second chamber has larger pool depth. Similarly, the first chamber of a small opening SDM showed reduced air entrainment due to increased pool depth. When the depth of the pool increases, the recirculated air entrainment, understood as the air bubbles entrained by discrete vortices and released upwards, increases (Ervine and Ahmed 1984). The water in the second chamber after being subjected to the contracting opening becomes diffused into a disintegrated jet. The air entrainment is as high as to transform part of the disintegrated jet into spray in which case the energy dissipation could be large. This is due to the drag force exerted to the dispersed flow.

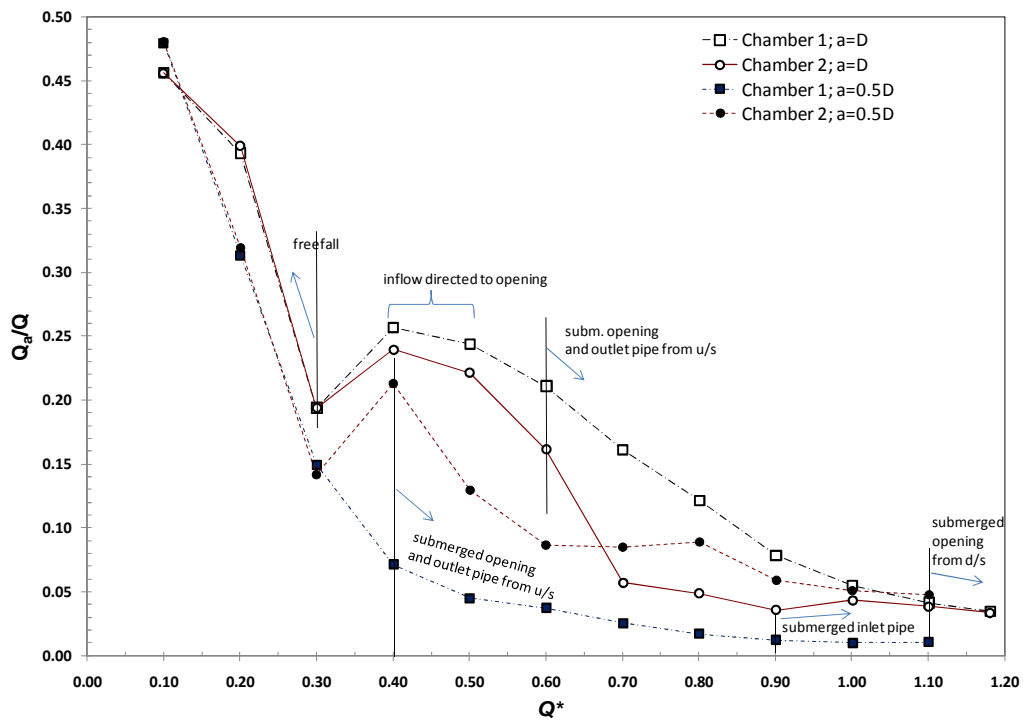


Figure 3.12 Dimensionless air flow rates inside the chambers of a symmetric SDM of large height ($h=8D$) of two opening heights

At high water flow rates, beyond $Q^*=0.80$, an intermittent inflow and outflow was experienced in the vent on top of the second chamber. The direction of the air flow could not be differentiated by the hotwire anemometer. Referring to Fig. 3.13, total air demanded by the SDM is compared with: 1) Rajaratnam et al. (1997) with

$h/D_s=6.63$ where D_s is the shaft diameter; and, 2) Gargano et al. (2008) in drop manholes, for $h/D_s=7.5$. Overall the role of the water cushion appears to be favourable in limiting the air entrainment in the SDM as it reduces the drop height and hence the jet velocity at impact. Ervine (1998) argued that the aeration is extremely sensitive to the degree of surface disturbances and internal turbulence in the upstream jet. In this regard, the turbulence intensity of the falling jet and highly disturbed free surface pool could contribute greatly as the water cushion has a large interfacial area.

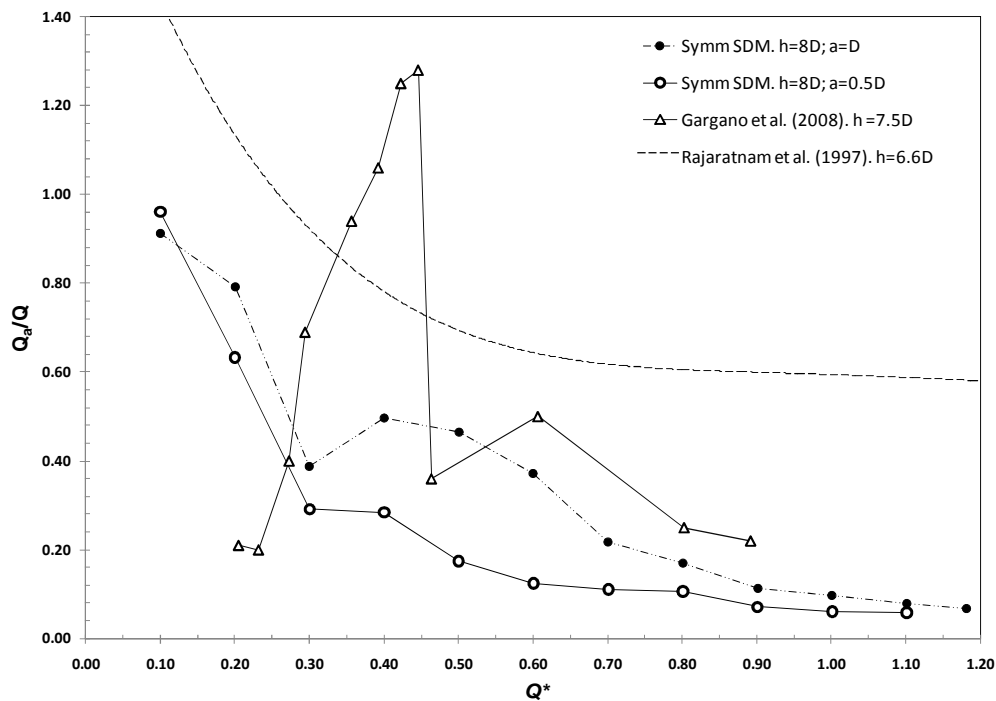


Figure 3.13 Dimensionless air flow rates inside: 1) symmetric SDMs of two opening heights, 2) a single drop manhole (Gargano et al. 2008), and 3) a dropshaft (Rajaratnam et al. 1997)

3.7 SUMMARY AND CONCLUSIONS

An experimental investigation on stacked drop manholes was carried out on two model structures with symmetric and offset alignments. Three flow regimes were classified in the first chamber: 1) A regime RI featured by a free falling jet hitting the bottom of the chamber and maintaining open-channel flow throughout the structure;

2) A regime RIII characterized by an inflow jet impinging on the front wall; and, 3) A transitional regime RII when one or both nappes of the falling jet impinged in the surroundings of the in-between opening. In the second chamber, once the outlet entrance was submerged, two types of flow were featured: 1) when the outflow runs as full pipe flow; and, 2) when an orifice type of flow is developed in the outlet pipe.

From momentum considerations, predictions on pool depths and energy losses were derived for a critical condition; i.e. a dropshaft type flow in the first chamber and an orifice outflow in the second chamber. Empirical factors were required to adjust pool depth predictions with corresponding measurements. Relative energy head losses (η) ranged between 70 to 95% inside the SDM. A mild decrease on η was observed with an increase in flow rate. Under surcharged flow conditions, average loss coefficients of $K=2.7$ for the SDM of large opening height and $K=6.4$ for the SDM of small opening height were recorded. Finally, air flow rates were recorded in a SDM for the largest total drop height ($h=8D$) and two opening heights. Overall less air was entrained into the structure once submergence of the opening from downstream occurred as compared to other drop structures of similar height. The increased drop height tested in this design showed an adequate performance being efficient in dissipating energy and producing moderate air entrainment in the system.

From a design standpoint, a square geometry of $3D \times 3D$ in the chambers of a symmetric SDM is found sufficient to allow major mechanisms of recirculation and plunging. No added dissipating benefit is observed from a larger section ($3.2D \times 4D$) of an offset SDM. A rectangular opening of large height ($a=D$) produces small losses under surcharged condition being efficient in dissipating energy under free fall operation. A drop height of $8D$ does not show excessive air entrainment as compared to other drop structures; however, a noticeable reduction in air transported into the outlet pipe is observed once the opening is submerged from downstream. Air vents in both chambers are required to supply the air demand. A free board of about $2D$ above the inlet pipe is recommended for supercritical inflows.

Notation

a, b = height and width of the rectangular opening in-between chambers

A = flow cross-sectional area normal to the direction of the flow

A_w = area of flow across the rectangular opening

B, L = width and length of each chamber

C = air concentration

C_I = experimental coefficient

C_c = contraction coefficient of the flow across the opening

C_{c3} = contraction coefficient of the outgoing flow

C_d = discharge coefficient

C_v = velocity coefficient

$CV_{1,2}$ = control volume 1 and 2.

D = pipe diameter

D_e = equivalent diameter = $(4A_w/\pi)^{1/2}$

D_s = shaft diameter

F_o = approaching Froude number

$F_{1u, 2u}$ = pressure forces on the upstream walls of CV_1 and CV_2

$F_{1d, 2d}$ = pressure forces on the downstream walls of CV_1 and CV_2

F_w = pressure force at the vena contracta of the flow out of the opening

F_3 = pressure force from the outgoing flow

F_D = drop Froude number

g = acceleration due to gravity

$h_{1,2}$ = drop height of chamber 1 and 2, respectively

$h = h_1 + h_2 =$ total drop height

$H_o =$ total energy head in the incoming flow

$H_3 =$ residual energy in the outgoing flow

$K =$ coefficient of local head-loss

$Q =$ water flow rate

$Q_a =$ air flow rate

$Q^* = Q/(gD^5)^{0.5} =$ dimensionless discharge

$Q^+ = Q/(gD_e^5)^{0.5} =$ dimensionless discharge

$V =$ mean velocity

$V_m =$ maximum velocity

$V_{wx} =$ x -component of the mean flow velocity at the vena contracta

$x =$ axial coordinate in the direction of the inlet and outlet pipes;

$y_{0,3} =$ central water depth in the incoming and outgoing pipe, respectively

$y_{1,2} =$ characteristic depth of water in chamber 1 and 2

$y_b =$ flow depth of the air-water mixture

$y_{op} =$ flow depth across the rectangular opening

$\alpha =$ kinetic energy coefficient for non-uniform flow

$\Delta H =$ energy head loss

$\Delta y = y_1 + h_2 - y_2$

$\eta = \Delta H/H_o =$ efficiency in energy dissipation

$\rho =$ water density

$\phi_{1,2} =$ coefficient relating effective to hydrostatic pressure on walls of CV₁ and CV₂

$\theta =$ deflected angle of the outflow from the opening with the horizontal

Subscripts

0 = inlet pipe section

1 = chamber 1

2 = chamber 2

3 = outlet pipe section

w = sharp-edged rectangular opening or zero-height weir section

APPENDIX 3.A: FLOW CHARACTERISTICS OVER THE OPENING IN-BETWEEN CHAMBERS.

Velocities and pressures at the vertical centerline of the jet out of the in-between opening were measured with a Pitot tube. Firstly, a freely falling jet into the second chamber was considered having regime RI in the first chamber. The velocity profiles were normalized by the maximum velocity of each profile V_m and the local coordinate y normalized by its value $y_{1/2}$ when V equals $V_m/2$ (Fig. 3.14). The local coordinate was measured upwards perpendicular to the flow direction from the lower nappe of the jet at the section of measurement. Secondly, three levels of submergence in a small height SDM ($h=4D$) were set using a valve at the end of the outgoing pipe. A fairly uniform velocity and pressure distributions across the vertical centerline of the flow out of the opening are illustrated in Fig. 3.15. The elevation difference between the water surface in chambers equals to 0.40 m, 0.20 m and 0.125 m for $Q^*=0.50$, 0.83 and 1.09, respectively.

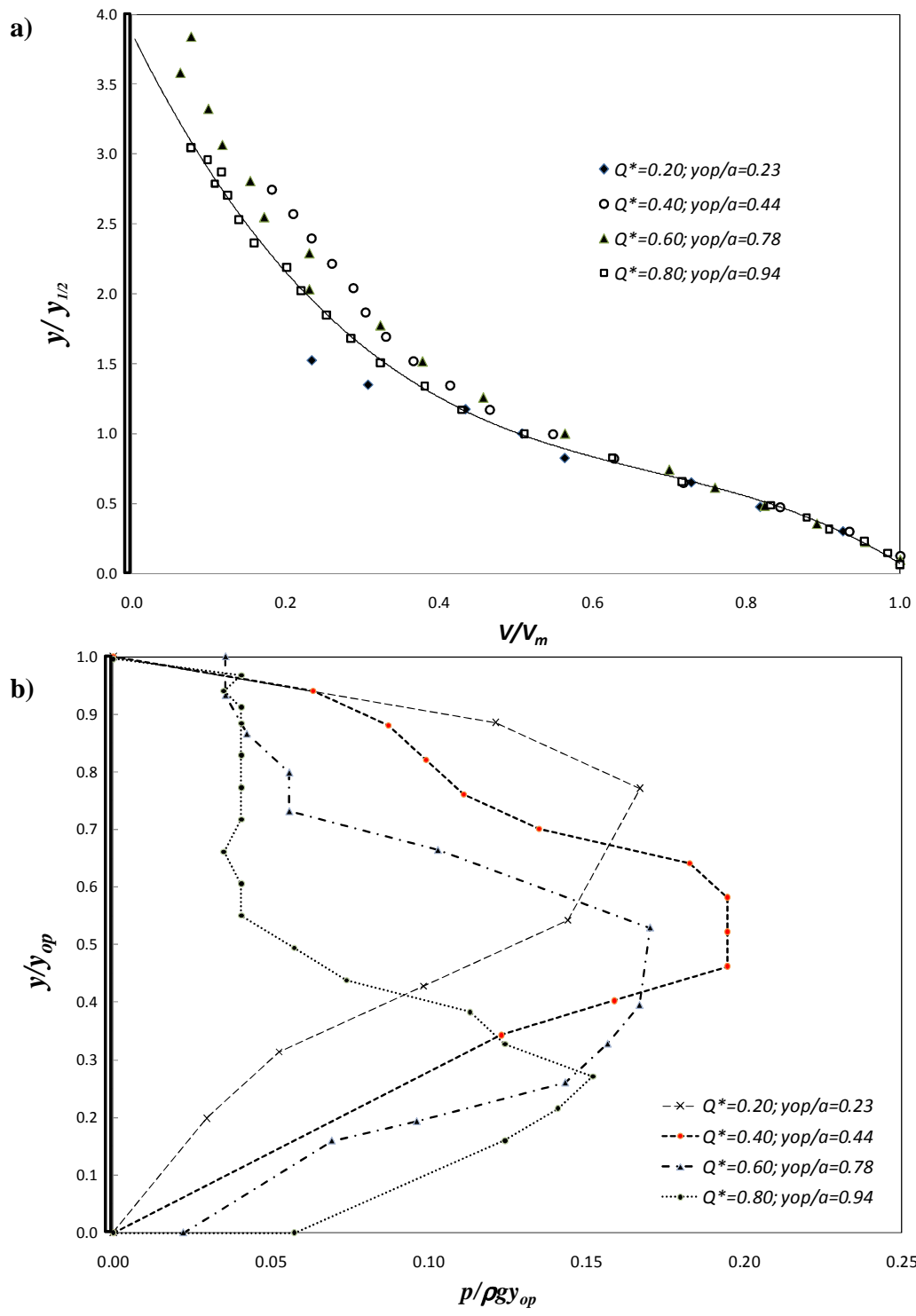


Figure 3.14 a) Normalized velocity profiles; b) normalized pressure profiles in the centerline of the jet out of the opening between chambers of a SDM ($h_I=4D$) under RI.

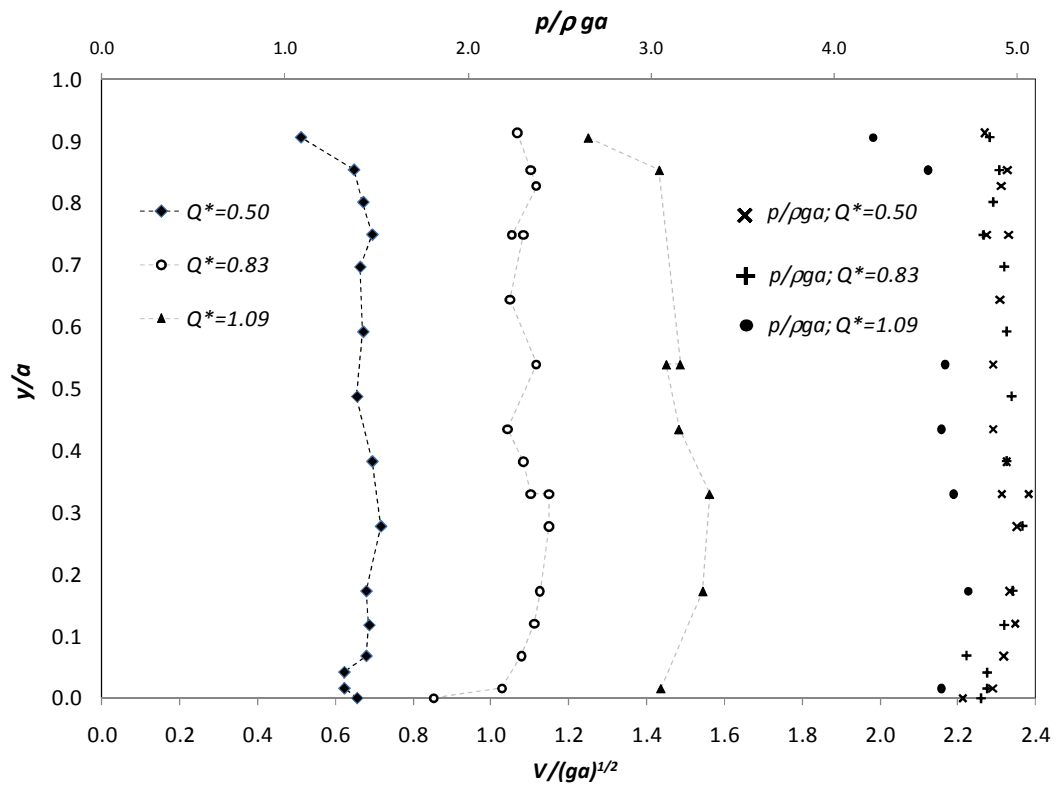


Figure 3.15 Normalized pressure and velocity profiles in the centerline of the jet out of the opening under fully surcharged flow inside a small height SDM ($h=4D$)

APPENDIX 3.B: ONE-DIMENSIONAL MOMENTUM ANALYSIS.

Control volume CV₁

Recalling the momentum equation in CV₁ in Eq. [3.1]:

$$[3.1] \quad F_{1u} - F_{1d} - F_w = \rho Q V_{w_x}$$

While F_{1u} is assumed to follow a hydrostatic pressure distribution, F_{1d} is expected to deviate from a hydrostatic pressure distribution in the front-to-jet wall due to a curved streamlining into the exit of the first chamber. Accordingly, a coefficient φ_1 relating the effective to hydrostatic pressure force is considered for F_{1d} for the area above the opening. F_w is assumed to be negligible as long as water flows freely out of the first chamber.

$$[B1] \quad F_{1u} = \frac{1}{2} \rho g y_1^2 B$$

$$[B2] \quad F_{1d} = \frac{1}{2} \rho g y_1^2 (B-b) + \varphi_1 \left[\frac{1}{2} \rho g y_1^2 b - \rho g A_w \left(y_1 - \frac{a}{2} \right) \right]$$

Substituting Eqs. [B1] and [B2] in [3.1], gives:

$$[B3] \quad (1-\varphi_1) \frac{1}{2} \rho g y_1^2 b + \varphi_1 \rho g A_w \left(y_1 - \frac{a}{2} \right) = \frac{\rho Q^2}{C_c A_w} \cos \theta$$

where: B represents the width of the chambers; a and b , the height and width of the opening (Fig. 3.6a); and, C_c is the contraction coefficient relating the area of the vena contracta to the area of flow across the opening A_w . Dividing Eq. [B3] by $\rho g A_w \varphi_1$, it yields:

$$[B4] \quad \left(\frac{1}{\varphi_1} - 1 \right) \frac{1}{2a} y_1^2 + y_1 - \left(\frac{Q^2 \cos \theta}{\varphi_1 g A_w^2 C_c} + \frac{a}{2} \right) = 0$$

The quadratic Eq. [B4] could be solved for y_1 as presented in Eq. [3.2]:

$$[3.2] \quad y_1 / D_e = \left(-1 + \sqrt{1 + \left(\frac{1}{\varphi_1} - 1 \right) \left(1 + \frac{2 \cos \theta}{a \varphi_1 C_c} \frac{Q^2}{g A_w^2} \right)} \right) / \left(\frac{D_e}{a} \left(\frac{1}{\varphi_1} - 1 \right) \right)$$

Control volume CV₂

The momentum equation for CV₂ is given by:

$$[B5] \quad F_w + F_{2u} - F_{2d} - F_3 = \frac{\rho Q^2}{A} \left(\frac{1}{C_{c3}} - \cos \theta \frac{A}{C_c A_w} \right)$$

where C_{c3} is the contraction coefficient of the outgoing flow. While a hydrostatic pressure force could be assumed on the upstream wall F_{2u} , an effective pressure force in the downstream wall F_{2d} is a more realistic assumption. F_{2d} is corrected from a hydrostatic pressure force by φ_2 . The pressure in the vena contracta F_w is considered negligible as is a free jet; and a hydrostatic pressure force in the partially full flow of the outlet pipe F_3 is accounted. An approximate relation $A_3 = (y_3/D)A$ with an error of less than 5% for $y/D > 0.4$ could be applied where $A = \pi D^2 / 4$, y_3 is the water depth in the outlet pipe and D the diameter of the outlet pipe. The pressure force in the pipe is then given by: $F_3 = (1/2) \rho g A D (y_3 / D)^{2.2}$ with less than 3% error for $y/D > 0.5$ (Zhao et al. 2004). The forces on walls are:

$$[B6] \quad F_{2u} = \frac{1}{2} \rho g y_2^2 B$$

$$[B7] \quad F_{2d} = \frac{1}{2} \rho g y_2^2 (B - D) + \varphi_2 \left[\frac{1}{2} \rho g y_2^2 D - \rho g A \left(y_2 - \frac{D}{2} \right) \right]$$

Substituting expressions [B6] and [B7] in [B5] with some algebraic arrangements yields:

$$[B8] \quad \left(\frac{1}{\varphi_2} - 1 \right) \frac{D}{2A} y_2^2 + y_2 - \left[\frac{Q^2}{g \varphi_2 A^2} \left(\frac{1}{C_{c3}} - \frac{\cos \theta}{C_c} \frac{A}{A_w} \right) + \frac{D}{2} \left(\frac{C_{c3}^{2.2}}{\varphi_2} + 1 \right) \right] = 0$$

Solving the quadratic expression [B8] for the pool depth in the second chamber simplifies:

$$[3.3] \quad \frac{y_2}{D} = \left(-1 + \sqrt{1 + \frac{2D}{A} \left(\frac{1}{\varphi_2} - 1 \right) \left(\frac{Q^2}{g \varphi_2 A^2} \left(\frac{1}{C_{c3}} - \frac{\cos \theta}{C_c} \frac{A}{A_w} \right) + \frac{D}{2} \left(\frac{C_{c3}^{2.2}}{\varphi_2} + 1 \right) \right)} \right) / \left(\left(\frac{1}{\varphi_2} - 1 \right) \frac{D^2}{A} \right)$$

Assuming solely hydrostatic pressure forces on the walls ($\varphi_2=1$), an expression of y_2/D essentially the same as the one for surcharged junctions with no lateral inflow, is obtained (Zhao et al. 2004).

APPENDIX 3.C: ORIFICE FLOW EQUATION.

While C_c could be considered constant, the velocity coefficient C_v is expected to change for each condition as it accounts for the energy losses. A more general relation of C_d could be derived from an energy equation between section i (Fig. 3.6a at vertical inflow jet right before plunging) and the vena contracta of the jet out of the opening.

$$[C1] \quad H_i = z_i + \frac{p_i}{\rho g} + \frac{V_i^2}{2g} = z_c + \frac{p_c}{\rho g} + \frac{\int_o^{y_c} V dy V^2 / 2g}{\int_o^{y_c} V dy} + \Delta H$$

where H_i is the total head at section i , z is the elevation from the datum at the center of the jet at the section of the vena contracta, p is the pressure, ΔH is the head loss and V is the velocity, y_c refers to the depth at the vena contracta. Subscripts i and c correspond to section i and vena contracta, respectively.

$$[C2] \quad y_1 + \frac{V_i^2}{2g} = \alpha_c \frac{V_c^2}{2g} + \Delta H$$

where α_c is the kinetic energy correction factor. Eq. [C2] could be reduced to:

$$[C3] \quad V_c = \sqrt{2g(H_i - \Delta H) / \alpha_c}$$

The energy loss between the two sections is expressed by introducing the velocity coefficient C_v , such that $V_c = C_v \sqrt{2g / \alpha_c (y_1 + V_i^2 / 2g)}$. Accordingly

$$\Delta H = (1 / C_v^2 - 1) \alpha_c V_c^2 / 2g$$

Solving this equation simultaneously with the continuity equation yields:

$$[C4] \quad Q = \left(C_c C_v / \sqrt{\alpha_c - C_c^2 C_v^2 (A_w / A_o)^2} \right) A_w \sqrt{2gy_1}$$

from where $C_d = C_c C_v / \sqrt{\alpha_c - C_c^2 C_v^2 (A_w / A_o)^2}$.

References

- Camino, G. A., Zhu, D. Z., Rajaratnam, N. and Shome M. (2009). "Use of a stacked drop manhole for energy dissipation: A case study in Edmonton." *Can. J. Civ. Eng.*, 36: 1037-1050.
- Chamani, M. R. and Beirami, M. K. (2002). "Flow characteristics at drops." *J. Hydraul. Eng., ASCE*, 128(8): 788-791.
- Chanson, H. (1998). "Hydraulics of Roman aqueducts: steep chutes, cascades and dropshafts". *Research Report Series*. Queensland, University of Queensland, Department of Civil Engineering: I-R-5.
- Chanson, H. (2002). "An experimental study of Roman dropshaft hydraulics." *J. Hydraul. Res.*, 40(1): 3-12.
- Christodoulou, G. C. (1991). "Drop manholes in supercritical pipelines." *J. Irrig. Drain. Eng., ASCE*, 117(1): 37-47.
- City of Calgary (2000). "Stormwater management and design manual". *Wastewater and Drainage*. Calgary, City of Calgary.
- Clausnitzer, B. and Hager, W. H. (1997). "Outflow characteristics from circular pipe." *J. Hydraul. Eng., ASCE*, 123(10): 914-917.
- Edwini-Bonsu, S. and Steffler, P. M. (2006). "Modeling ventilation phenomenon in sanitary sewer systems: A system theoretic approach." *J. Hydraul. Eng., ASCE*, 132(8): 778-790.
- Ervine, D. A. (1998). "Air entrainment in hydraulic structures: A review." *Proc. Inst. Civ. Eng. Water Marit. Energy*, 130(3): 142-153.
- Ervine, D. A. and Ahmed, A. A. (1984). The process of aeration in closed conduit hydraulic structures. *Proc. Symposium on Scale Effects in Modelling Hydraulic Struct.*, Esslingen, Germany, September 3-7, 1984.
- Falvey, H. T. (1980). "Air-water flow in hydraulic structures." *Water & Power Resour. Serv.* E. M. 41. Denver, U.S.A., USBR.
- Gargano, R., Granata, F. and de Marinis, G. (2008). Il trasporto d'aria nei pozzetti di salto circolari. *Proc. 31 Convegno Nazionale di Idraulica e Costruzioni Idrauliche*, Perugia, September 9-12, 2008.
- Gargano, R. and Hager, W. H. (2002). "Supercritical flow across sewer manholes." *J. Hydraul. Eng., ASCE*, 128(11): 1014-1017.
- Gayer, J. A. (1984). On the hydraulic role of manholes in urban storm drainage systems. *Proc. 3rd Int. Conf. on Urban Storm Drainage*, Goteborg, 1984.
- Granata, F., de Marinis, G., Gargano, R. and Hager, W. H. (2010). "Hydraulics of circular drop manholes." *J. Irrig. Drain. Eng., ASCE*: Posted ahead of print 16 July 2010.
- Hager, W. H. (1992). "Drop manholes in supercritical pipelines - Discussion." *J. Irrig. Drain. Eng., ASCE*, 118(5): 832-832.

- Kusuda, T. and Arao, S. (1996). Energy losses at circular drop manholes. *Proc. 7th Int. Conf. on Urban Storm Drainage*, Hannover, 1996.
- Marsalek, J. (1984). "Head losses at sewer junction manholes." *J. Hydraul. Eng., ASCE*, 110(8): 1150-1154.
- Moore, W. L. (1943). "Energy loss at the base of a free overfall." *ASCE Transactions*, 108: 1343-1361.
- Rajaratnam, N. and Chamani, M. R. (1995). "Energy loss at drops." *J. Hydraul. Res.*, 33(3): 373-384.
- Rajaratnam, N., Mainali, A. and Hsung, C. Y. (1997). "Observations on flow in vertical dropshafts in urban drainage systems." *J. Environ. Eng., ASCE*, 123(5): 486-491.
- Rajaratnam, N. and Subramanya, K. (1967). "Flow equation for the sluice gate." *J. Irrig. Drain. Div., ASCE*, 93(IR3): 167-186.
- Ramamurthy, A. S. and Zhu, W. (1997). "Combining flows in 90° junctions of rectangular closed conduits." *J. Hydraul. Eng., ASCE*, 123(11): 1012-1019.
- Roth, A. and Hager, W. H. (1999). "Underflow of standard sluice gate." *Exp. Fluids*, 27(4): 339-350.
- Sangster, W. M., Wood, H.W., Smerdon, E.T. and Bossy, H.G. (1958). "Pressure Changes at Storm Drain Junctions". *Eng. Series Bulletin*. E. E. Station, University of Missouri.
- Shumate, E. D. and Weber, L. J. (1998). Experimental description of combining flows at an open channel junction. *Proc. International Water Resources Eng. Conf.*, Memphis, Tennessee, USA, 3-7 August 1998.
- Smith, C. D. (1995). *Hydraulic Structures*. Saskatchewan, University of Saskatchewan Printing Services.
- USACE (1997). Chapter 6. Design Considerations. *Engineering and Design - Tunnels and Shafts in Rock*. EM 1110-2-2901.
- Zhao, C. H., Zhu, D. Z. and Rajaratnam, N. (2004). "Supercritical sewer flows at a combining junction: A model study of the Edworthy trunk junction, Calgary, Alberta." *J. Environ. Eng. Sci.*, 3(5): 343-353.
- Zhao, C. H., Zhu, D. Z., Sun, S. K. and Liu, Z. P. (2006). "Experimental study of flow in a vortex drop shaft." *J. Hydraul. Eng., ASCE*, 132(1): 61-68.

CHAPTER 4: JET DIFFUSION INSIDE A CONFINED CHAMBER *

4.1 INTRODUCTION

Energy loss by jet diffusion in confined jets can be very effective within short distances from the jet exit (Rajaratnam et al. 1993; Liu et al. 2006). Even though there is an extensive theory for turbulent jets issuing into a large stagnant environment, its application is limited for confined settings. Either by the presence of a solid boundary or a free surface, the hydrodynamic behavior of confined jets depends strongly on the bounding surfaces. Studies on confined jets in ducts have shown that a stable eddy or region of recirculation is formed which eventually degenerates to fully developed pipe flow if the duct is long enough (Rajaratnam, 1976). Similarly, jet mixing and entrainment is dramatically affected in shallow water jets due to the finite extent of the ambient fluid restricted by a free surface above and a solid wall below (Rodi 1982; Shinneeb et al. 2010). The jet velocity was shown to decay much faster in fishways with tight enclosures than in jets issued in large stagnant ambient (Liu et al. 2006).

In urban drainage systems, the energy losses attained within the pools formed at the bottom of drop structures such as dropshafts and drop manholes can be significant (Rajaratnam et al. 1997; Camino et al. 2009). The dissipative capacity is believed to be due partly to the diffusion of the plunging jets in the pool. The purpose of the present study is to investigate vertical water jets diffusing inside a confining chamber pool with focus on energy dissipation. A circular jet issuing vertically into a pool was setup to examine: 1) the effect of the level of confinement or enclosure size; and, 2)

* Part of the content of this chapter has been submitted to the Journal of Hydraulic Research

the effect of the location of entry. Measurements of the velocity decay in the centerline of the confined jets, velocity profiles in center planes were obtained. A relationship was also developed to assess the capacity to dissipate energy of a confined jet enclosed within a chamber of only few diameters in length.

4.2 EXPERIMENTAL ARRANGEMENT AND PROGRAM

Fig. 4.1 shows the experimental setup. Water from an underground sump was pumped through a clear pipe producing a full pipe flow condition. After an initial horizontal section, the inflow pipe turned into a vertical pipe for a length of 800mm. A number of researchers have used long tubes to produce jets so that the jet possesses either a fully developed laminar or turbulent velocity profile on emergence (McCarthy and Molloy 1974). The total length of the pipe is assumed to be large enough ($> \sim 30d$, d is the diameter of the inlet pipe) to produce a fully developed velocity profile at the emergence of the jet. The jet was discharged into a plexiglass chamber of square section ($L^2 = L_y \times L_z = 0.38\text{m} \times 0.38\text{m}$ with L being the length scale of the chamber size). An outlet pipe of 152mm in diameter was connected at right angle to a wall of the chamber with its invert at the level of the chamber's bottom. A valve was placed at the end of the outlet pipe to produce any desired downstream pressure which would control the water level in the chamber.

Series of experiments were run to observe the effect of the location where the jet entered the chamber and its confinement with respect to the chamber's enclosure (Table 4.1). Experiments were run with three jet locations, one having the inlet pipe attached to the wall having the outlet which will subsequently be called outlet-wall. A second jet position was at the center of the chamber and a last location attached to the wall opposite to the outlet-wall. This last wall is called front-wall hereafter. Two values of the inlet pipe diameter $d=102\text{mm}$ and 152mm were used, thus the confinement $L/d=3.7$ and $L/d=2.5$, respectively, where $L=0.38\text{m}$. The water surface in the chamber was kept slightly above the inlet pipe to avoid air entrainment which could undermine the accuracy of the velocity measurements (Liu 2004). The jet

Reynolds number ($R_o = U_o d / \nu$ where U_o is the uniform jet exit velocity and ν is the kinematic viscosity) was set to a sufficiently high value (between 9.5×10^4 and 2.4×10^5) as to produce a turbulent jet and at the same time assure a full pipe flow in the inflow.

Table 4.1. Experimental conditions

Inlet pipe diameter (mm)	$L_y \times L_z$ (m ²)	L/d	h_o (m)	Location of entry	Outlet pipe diameter (mm)
102	0.38 x 0.38	3.7	0.942~0.974	C; EOW	152
152		2.5	0.878~0.937	C; EOW; EFW	

C = centered entry; EOW = eccentric (outlet-wall) entry; and, EFW = eccentric (front-wall) entry

The flow rate, Q_o , was measured in the inflow line with a magnetic flowmeter. Point velocity measurements were obtained using acoustic Doppler velocimeters (ADV) at the centerline jet axis and center planes XY and XZ perpendicular and parallel to the outlet-wall (Fig. 4.2). The acoustic Doppler devices were tilted up to about seven degrees with respect to the vertical to access the sampling volume in the centerline streamwise axis. Russello et al. (2006) tested the Vectrino-ADV at different angles of tilting and observed that the wake left by the probe head does not reach the sampling volume showing an almost ideal response compared to PIV velocity results. Due to limitations in accessibility, the maximum velocity at each section was assumed to be at the centerline of the jet. Pressure readings were taken at a number of locations in the downstream pipe using piezometers. Water depths were measured in the chamber using graduated meters.

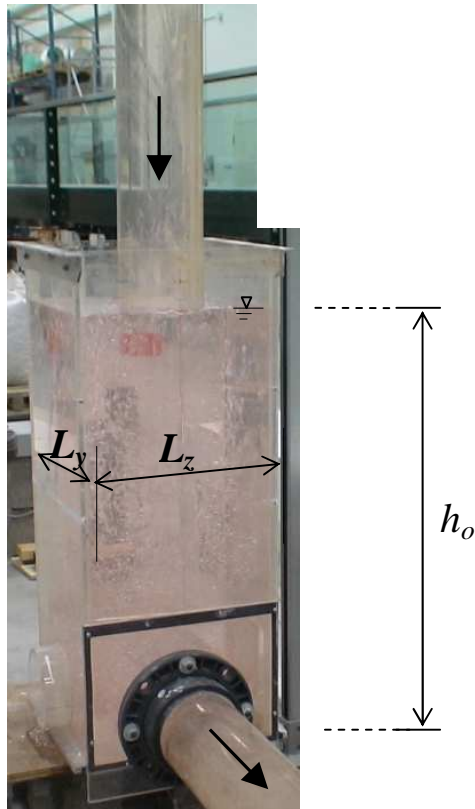


Figure 4.1 Experimental setup with definition sketch of the rectangular chamber

The vertical efflux from the pipe, acts very much like a submerged jet and the piezometric pressure could be assumed to be approximately constant in the pool. While the volume flux steadily increases along the jet axial direction due to entrainment, the kinetic energy flux rapidly decreases through the production of turbulence and viscous dissipation. The momentum flux in a free turbulent jet is conserved if the entrained fluid enters the jet perpendicular to the flow in the jet. The solid boundaries of a confined chamber produce circulation in the surrounding fluid opposite to the direction of the inflow. The negative momentum of the counterflow that is entrained by the jet will reduce the inflow momentum making the jet to slow down rapidly. Further, the jet travelling through the pool will not only be affected by the presence of the bottom which makes the jet an impinging jet, but also by the flow

redirection into the outlet pipe. All these would make the jet behave in a manner very different from that of the simple jet in a large ambient essentially at rest.

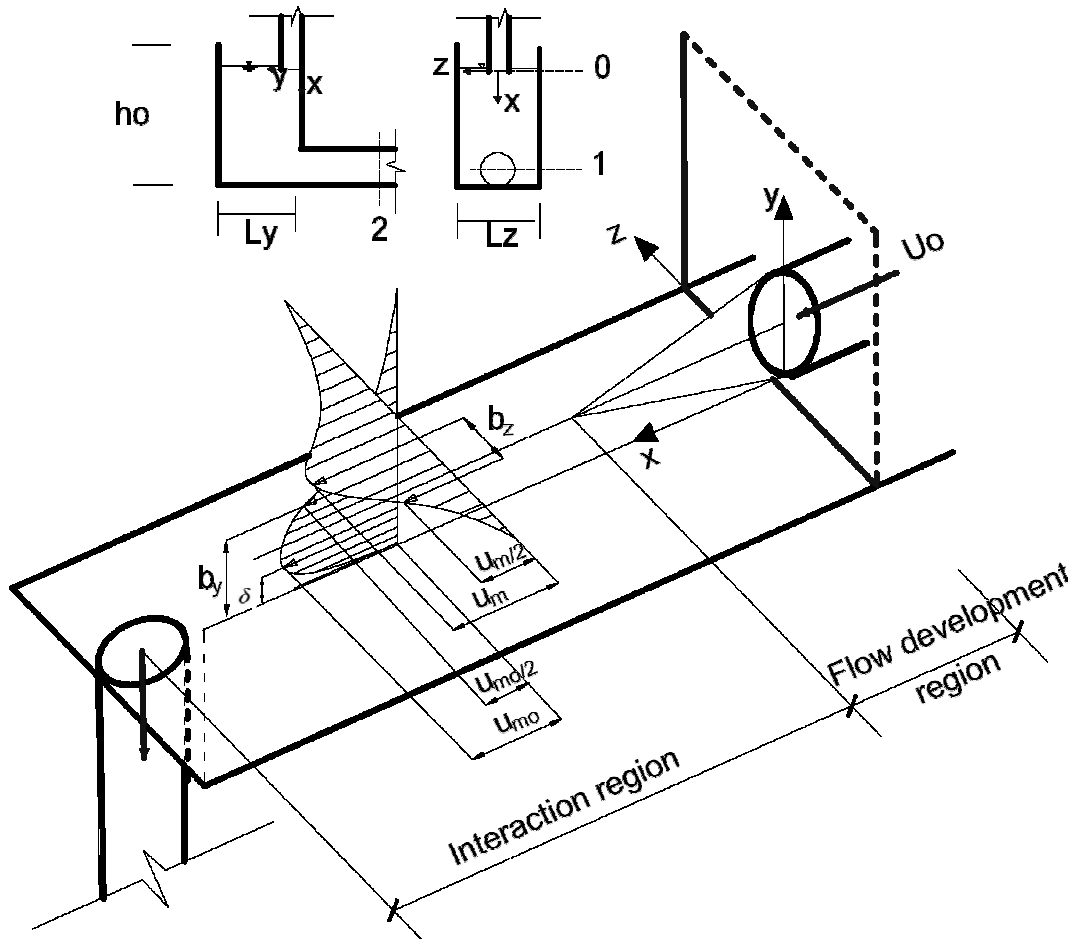


Figure 4.2 Velocity structure of a circular bluff wall jet (inside a manhole chamber)

4.3 METHOD TO COMPUTE ENERGY LOSSES

Although the complications imposed by the confinement of the chamber limit an analytical derivation of the complete flow development, it is possible to develop an expression to predict energy losses based on the theory of turbulent jets. This approach was proved valid on flows inside small size manholes with straight throughflow (Pedersen and Mark 1990).

The total energy per unit volume at the exit of the jet E_T (section 0 in Fig. 4.2) can be expressed as:

$$[4.1] \quad E_T = \rho g h_o + \frac{\rho U_o^2}{2}$$

where h_o represents the depth of water in the chamber, ρ is the water density, g is the acceleration due to gravity, and $\rho U_o^2/2$ is the dynamic pressure at the entry level of the jet. It is assumed that the pressure distribution in the chamber is hydrostatic, i.e. the piezometric pressure remains constant across the pool; including sections 0 and 1. A valid assumption considering that the abrupt change in the cross-sectional area ratio between the inlet jet pipe and the chamber will produce flow separation zones, very much as the flow in a sudden expansion, in which the pressure downstream the expansion remains approximately constant in that region (Mehta 1981; Canbazoglu and Bozkir 2004)

The energy dissipation in the pool is believed to be accomplished mainly by jet diffusion (Rajaratnam et al. 1993). A circular jet of diameter d , emerging from a nozzle with a (close to) uniform velocity (U_o) tangential to a wall, becomes a three-dimensional wall jet or bluff wall jet (Fig. 4.2). Two regions related to the maximum velocity decay are recognized along the axial direction: a) the potential core region; and, b) the radial-type decay region (Rajaratnam 1976). Downstream of the potential core, in the region of fully developed flow, the distribution of the time-averaged axial velocity is similar in the y -direction in the central plane where $z=0$ (Law and Herlina 2002). Thus the velocity at the central plane ($z = 0$), u_m , can be scaled by its maximum velocity u_{mo} , $u_m/u_{mo} = f_1(\eta_y)$ where f_1 denotes a functional relation, and $\eta_y = y/b_y$ with b_y being the distance in y -direction where $u_m = u_{mo}/2$. Similarly, the change of the u velocity with z can be expressed as $u/u_m = g_1(\eta_z)$, where $\eta_z = z/b_z$ and b_z is the distance in z -direction where $u = u_m/2$.

The velocity distribution in a center plane XZ parallel to the wall is well approximated by a Gaussian distribution, Eq. [4.2] (Wu and Rajaratnam 1990). Law and Herlina (2002) showed that there is no difference in the shape of the velocity

profile between two-dimensional and three dimensional wall jets at the symmetry plane XY. A normal distribution, of the form in Eq. [4.3], underestimates slightly (less than 4%) the total flow passing across a section with a wall-jet type velocity profile.

$$[4.2] \quad \frac{u}{u_m} = g_1(\eta_z) = \exp(-0.693\eta_z^2)$$

$$[4.3] \quad \frac{u_m}{u_{mo}} = f_1(\eta_y) = \exp(-0.693\eta_y^2)$$

In the fully-developed flow region, u_{mo} is inversely proportional to x and both length scales grow linearly with the longitudinal distance x . Padmanabham and Gowda (1991) made a review of the growth rate of three dimensional wall jets, the values suggested by Rajaratnam and Pani (1974) are $db_y/dx = 0.045$ and $db_z/dx = 0.21$.

The kinetic energy flux E at any distance x is given by Eq. [4.4].

$$[4.4] \quad E = \int_0^{L_y+L_z/2} \int_{-L_z/2}^{L_z/2} \rho \frac{u^2}{2} u \, dy \, dz$$

where L_y and L_z are the length and width of the chamber cross section, respectively. The limits of integration assume negligible effect of the recirculation within the chamber.

$$[4.5] \quad \frac{E}{E_o} = \frac{1}{A_o} \int_0^{L_y+L_z/2} \int_{-L_z/2}^{L_z/2} \left(\frac{u}{U_o} \right)^3 \, dy \, dz$$

where A_o is the area of the jet at the emergence, E_o is the initial kinetic energy flux ($=Q_o\rho U_o^2/2$) and $Q_o (= U_o A_o)$. Using the functional relationships f_1 and g_1 ,

$$[4.6] \quad \frac{E}{E_o} = \left(\frac{u_{mo}}{U_o} \right)^3 \frac{1}{A_o} \int_0^{L_y+L_z/2} \int_{-L_z/2}^{L_z/2} \left[f_1(\eta_y) g_1(\eta_z) \right]^3 dy dz$$

Implementing the Gaussian distributions of Eqs. [4.2] and [4.3] into [4.6]:

$$[4.7] \quad \frac{E}{E_o} = \left(\frac{u_{mo}}{U_o} \right)^3 \frac{1}{A_o} \int_0^{L_y+L_z/2} \int_{-L_z/2}^{L_z/2} e^{-(1.44\eta_z)^2} dz e^{-(1.44\eta_y)^2} dy$$

Eq. [4.7] then yields:

$$[4.8] \quad \frac{E}{E_o} = \frac{\pi}{4.158 A_o} b_y b_z \left(\frac{u_{mo}}{U_o} \right)^3 \operatorname{erf} \left(1.44 \frac{L_y}{b_y} \right) \operatorname{erf} \left(0.72 \frac{L_z}{b_z} \right)$$

Furthermore, as the flow rate in the jet increases in the streamwise direction due to the entrained flow from the ambient water, in a steady state situation, the outlet is not able to accommodate the added flow resulting in a retarding flow turning back against the jet flow. At an axial distance x from the nozzle, the jet flow rate Q is given by:

$$[4.9] \quad \frac{Q}{Q_o} = \frac{\pi}{1.386 A_o} b_y b_z \left(\frac{u_{mo}}{U_o} \right) \operatorname{erf} \left(0.832 \frac{L_y}{b_y} \right) \operatorname{erf} \left(0.416 \frac{L_z}{b_z} \right)$$

From Eqs. [4.8] and [4.9], one can get the kinetic energy head $\frac{E}{\rho g Q}$ at a section x in the streamwise direction of the jet. If E_1 represents the kinetic energy flux at a section across the chamber aligned with the axis of the outlet pipe (section 1 in Fig. 4.2), the total energy head at section 2 in the outlet pipe (H_2) is obtained with Eq. [4.10]. Subscript 2 represents a section of the exit pipe sufficiently away from the disturbance due to the entrance to the outlet and before the exit valve.

$$[4.10] \quad H_2 = h_o + \frac{E_1}{\rho g Q} - h_c - h_f$$

where h_c represents the losses due to sudden contraction into the exit pipe associated mainly to the expansion downstream of the vena contracta in the pipe, and h_f is the

loss due to pipe friction. Contraction losses can be evaluated using Borda-Carnot loss formula $h_c \approx (1/C_c - 1)^2 V^2/2g$ where C_c is the experimentally determined contraction coefficient of the outgoing flow and V is the mean velocity downstream the contraction. Friction losses in a pipe are given by $h_f = \frac{fl}{4R} V^2/2g$; where f is the friction factor, l is the length of the pipe, and R is its hydraulic radius. E_l computes the kinetic energy flux considering only the dominant streamwise velocity component in that section. The energy flux converging into the outlet should be considered as the one contained in the portion of the jet flow in which the discharge equals the inflow discharge Q_o and before any deflexion due to impingement occurs.

Finally, the total relative energy losses η from the emergence of the jet (inlet pipe at section 0) to the exit pipe (at section 2) can be obtained by:

$$[4.11] \quad \eta = \frac{\Delta H_{02}}{H_o} = 1 - \frac{h_o + \frac{E_1}{\rho g Q} - h_c - h_f}{H_o}$$

where ΔH_{02} represents the energy head loss from section 0 to section 2. H_o is the initial energy head given by:

$$[4.12] \quad H_o = h_o + U_o^2/2g.$$

An average rate of energy dissipation $\bar{\epsilon}$ can be obtained in the water volume of the pool approximately by:

$$[4.13] \quad \bar{\epsilon} = \frac{\rho g Q_o \Delta H_{01}}{\rho h_o L_y L_z}$$

where $\Delta H_{01} = H_o - H_1$, being H_o and H_1 the energy head of the jet at sections 0 and 1. Predictions on relative energy losses and average energy dissipation rates are compared with measurements in the following paragraphs.

4.4 EXPERIMENTAL RESULTS

4.4.1 *Data quality analysis*

Velocity measurements were obtained using a MicroADV and a Vectrino-ADV. Both acoustic instruments use the Doppler shift principle to measure flow velocity by signalling acoustic targets in the flow (Kraus et al. 1994; Lohrmann et al. 1994; SonTek 1997). The sampling volume of both ADVs is a cylinder; 4.5mm in diameter and 5.6mm in height for the SonTek MicroADV (SonTek 1997); and 6mm in diameter and a user-selectable height between 3 and 15mm for the Nortek Vectrino (Nortek 2004). While the MicroADV can measure flow velocities from about 0.001 to 2.5m/s with an accuracy of $\pm 1\%$ of the measurement range; the Vectrino-ADV measures a velocity range from 0.01 to 4m/s with accuracy of $\pm 0.5\%$ of measured value. A redundant fourth receiver velocity component of the Vectrino can be used in various processing schemes to improve the accuracy of turbulent measurements.

A study to evaluate the time required achieving a converged value of mean velocity, turbulence intensity, and Reynolds shear stress was carried out to minimize the error due to a finite sampling time. An average was computed by increasing the number of samples used to define the parameter until the computed value does not change more than a stipulated value set 5%. The sampling time providing converged statistics within the 95% confidence interval was obtained within the first 30s in the axial direction while the velocity in the transverse direction was at least 180s. The mean velocity was found to control the sampling time of mean. From this analysis the convergence time was set to 180s and 300s for certain points in the vicinity of the outlet.

The correlation coefficient (COR) and the signal-to-noise ratio (SNR) are the main parameters to assess the quality of velocimeter measurements. Recommended values of SNR are greater than 15dB and values of COR greater than 70% for a good description of turbulence flow properties (SonTek, 1997). The minimum value of

COR (30%) required for the mean flow velocities was easily achieved with the MicroADV. More stringent correlation coefficients essential for the turbulence statistics could only be attained using the Vectrino-ADV (COR>70%). The operating frequency, i.e. the pulse repetition rates at which the sound is emitted, is higher in the MicroADV (up to 16MHz) than in the Vectrino (up to 10MHz). However, the maximum rate at which it is possible to get useful data from the instrument depends also on the data acquisition strategy, which is higher with the Vectrino (up to 200Hz) than with the MicroADV (50Hz).

The capability of the ADV to resolve turbulent fluctuations depends on the sampling conditions and characteristics of the flow. Garcia et al. (2005) argued that the turbulence parameters could be affected considerably if the sampling strategy is not adequate due to the presence of noise. They proposed a dimensionless parameter $F = (f_R L_r)/U_c$ where f_R is the user-defined frequency with which velocity data are recorded, U_c is the convective velocity and L_r is energy-containing eddy length scale, as a criterion to check the amount of energy filtered and aliased. As the dimensionless number $f_R L_r/U_c$ increases, a smaller portion of the energy is both filtered and aliased. The convective velocity was obtained using Taylor's frozen turbulence hypothesis (Heskestad 1965; Wu and Patterson 1989) and the length scale (L_r) was calculated using the integral length scale described by Wu and Patterson (1989) as $L_r = \sqrt{L_s^2 + L_n^2 + L_z^2}$. L_i is calculated on the basis of an integral time scale from the power spectrum with $i = s, n, z$ (Pope 2000; Goring and Nikora 2002). Garcia et al. (2005) demonstrated that F values above 20 assure a good representation of the turbulence of the flow producing reasonably small losses in the moments but at the same time resolves important portions of the spectrum. In this study, values of F below 20 were corrected with the proposed Acoustic Doppler velocimeter performance curves (Garcia et al. 2005).

Using ADV measuring technique, spikes in the signal are sometimes detected when: 1) the flow velocity is beyond the preset measurement range; 2) contamination from pulses reflected from the boundaries (Goring and Nikora 2002); and 3) air bubbles

(Liu et al. 2002). In this study, a phase-space thresholding method (PSTM) proposed by Goring and Nikora (2002) was used to remove the spikes from the contaminated ADV data. The noise energy level, on the other hand, could be computed using the spectral-analysis method (Voulgaris and Trowbridge 1998). The total noise was corrected by extending the inertial subrange $-5/3$ slope in the velocity spectrum down to the Nyquist frequency. The area under the modified velocity spectrum curve is the turbulence intensity corrected for noise.

4.4.2 *Velocity decay*

The kinetic energy of the flow is related to the maximum velocity, so that the maximum centerline velocity in the jet at different distances in the axial direction can be used to measure the dissipative capacity of the chamber by jet diffusion (Rajaratnam et al. 1993). In the fully developed region of a bluff wall jet, u_{mo} is proportional to $1/x$ in which x is the axial distance from a suitable virtual origin at distances sufficiently away from the nozzle (about $10d$ beyond potential core (Rajaratnam 1976)). The confined jet under analysis impinges on the bottom at $x/d=5.8$ for $L/d=2.5$ and $x/d=9.3$ for $L/d=3.7$. There is a strong interaction of the jet with the ambient fluid due to the bottom and walls of the chamber, and the ambient fluid produces counter-flow velocities which will increase turbulence and hence energy losses.

In Fig. 4.3, the centerline velocity decay of a confined jet ($L/d=3.7$ and 2.5) issuing at the center of the chamber is compared to the maximum velocity decay of a free circular jet and other jets found in the literature. One can observe, first, that there is a flow development region, in which the approximate average velocity at the jet exit remains constant along the centerline. This region is reduced from a distance of $6d$, typical of free circular jets, to about half that size. Second, the centerline velocity beyond the flow development region apparently decays with a linear relation to the axial distance, a region that can be called the interaction region where u_{mo}/U_o is proportional to x/d for the two levels of confinement tested. For practical purposes, a

linear relationship for a centered jet is presented in Eq. [4.14] for $L/d=2.5$ and Eq. [4.15] for $L/d=3.7$ with correlation coefficients equal to 0.927 and 0.981, respectively.

$$[4.14] \quad u_{mo}/U_o = -0.17(x/d) + 1.46$$

$$[4.15] \quad u_{mo}/U_o = -0.12(x/d) + 1.40$$

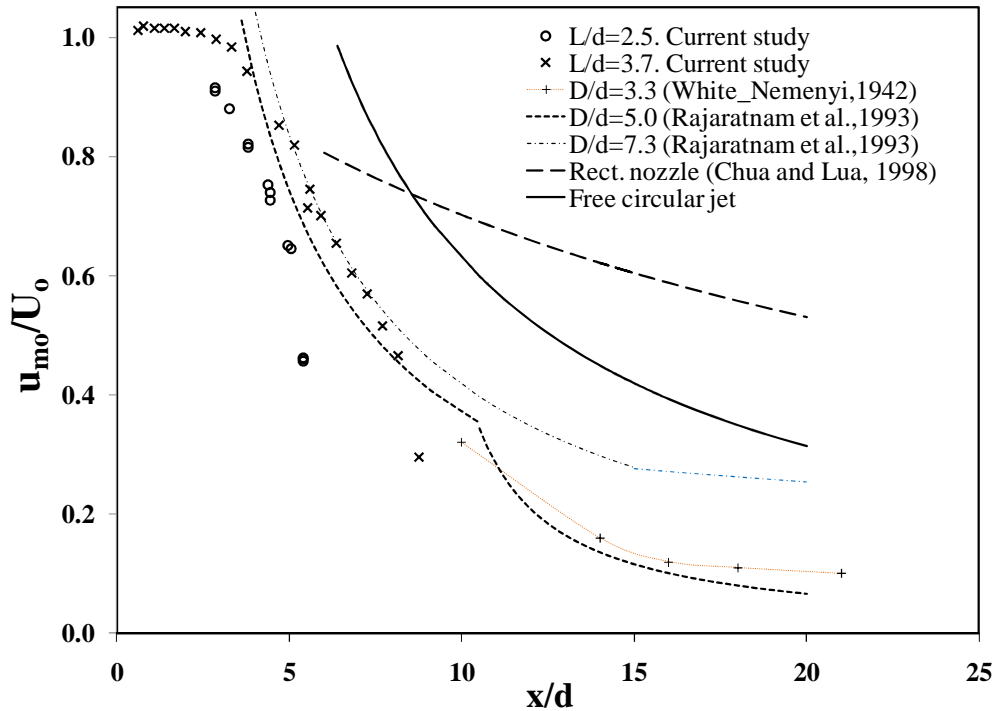


Figure 4.3 Maximum velocity decay in the streamwise direction of centered jets

The velocity decay of a three-dimensional wall jet emerging from circular nozzle in Fig. 4.3. was expressed in a power-law form by Padmanabham and Gowda (1991): $u_{mo}/U_o = a(x/h)^{-n}$, where: a is a constant, h is the distance normal to the plate from one edge of the circular orifice and n is the exponent describing the decay of the maximum velocity. Eccentrically located jets apparently produce a linear relationship (i.e. decay at a constant rate) up to about $x/d=5$ for $L/d=2.5$ and $x/d=7$ for $L/d=3.7$ (Fig. 4.4). A second gradient is observed in eccentric jets. The effect of the shear layers generated by the two lateral walls and front wall might be the main reason for this pattern. The second gradient produces a faster decay rate than that of a bluff wall

jet with no confinement. Overall, a confined jet appears to diffuse more rapidly both in the potential core region and the interaction region than a free jet due to reverse flows acting against the inflow jet direction.

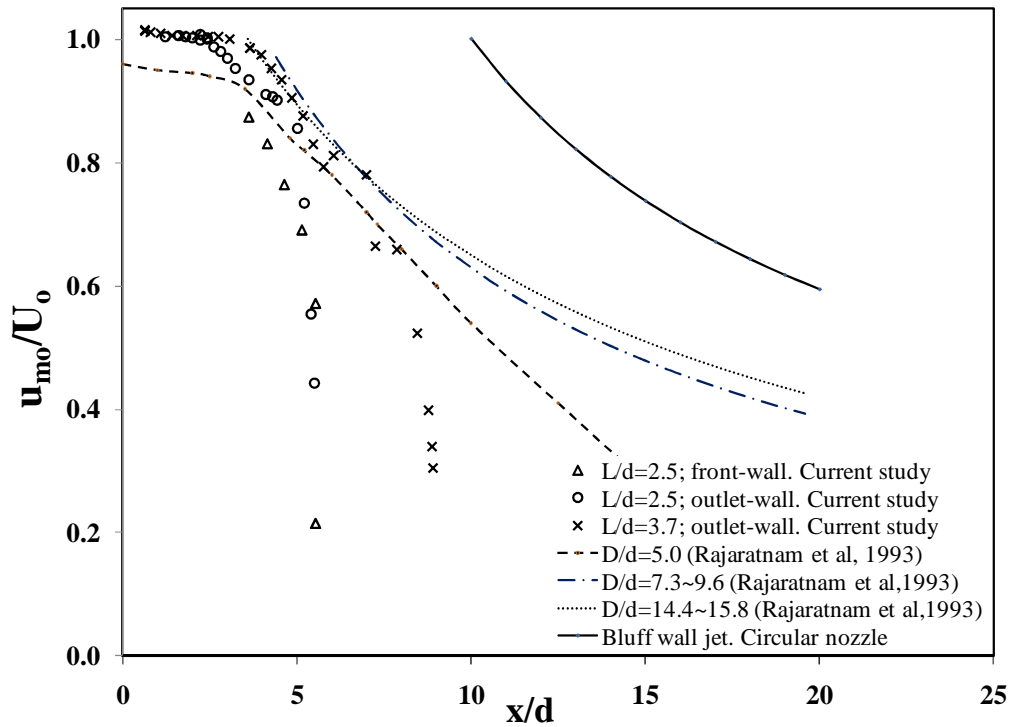


Figure 4.4 Maximum velocity decay in the streamwise direction of eccentric jets

Beltaos and Rajaratnam (1974) studied the effect of jet impingement on flat surfaces. They stated that the jet develops identically to a free jet up to $0.86h_o$ (h_o is the impingement height); beyond there, the jet undergoes considerable deflection. Both, the jet impingement and the presence of an outlet at the bottom of the chamber will have an effect on the velocity field in the chamber. Shammaa et al. (2005) studied the approaching velocity into a finite-size circular orifice in an infinite ambient flow. The approaching flow can be calculated as about $0.3U_o$ at a distance equal to half the orifice diameter. Our measurement, however, showed a small component of the centerline velocity in the y -direction (v) towards the outlet in the confined jet at the level of the centerline of the outlet. The velocity component v attains a maximum of $0.20U_o$ at about $x/d=5.4$ for $L/d=2.5$, and about $0.12U_o$ at $x/d=8.5$ for $L/d=3.7$. These

velocities are much smaller compared to the streamwise velocity component u ($0.55U_o$ and $0.53U_o$ respectively) and even less in terms of the kinetic energy. Therefore, it is reasonable to assume negligible effect of the lateral centerline velocity components in the analysis of the energy loss by jet diffusion.

4.4.3 *Velocity profiles*

The velocity profiles in two perpendicular planes (XZ and XY) crossing the centerline jet axis (Fig. 4.2) are plotted in a dimensionless form. The velocities in the streamwise direction are normalized with the length scale b_z and b_y for the z and y directions, respectively (Fig. 4.5 and Fig. 4.6). Within the potential core, the velocity profiles of a confined jet show a distribution similar to that of a top-hat velocity efflux. As compared to a free jet, there is an upward velocity component expressed as negative values. This reverse flow produces recirculation regions symmetrically on both sides of the jet in the plane XZ (Fig. 4.6) and a single vortex in the plane XY of the jet (Fig. 4.5).

An empirically fitted equation for a two-dimensional wall jet (Verhoff 1970) presents certain agreement with the profile at the furthest axial section ($x/d=8.48$) up to $z/b_z=2.0$, beyond this point, negative velocity components are recorded. This agreement suggests that the velocity profiles of a two-dimensional and a three-dimensional wall jet are similar to a confined setting in the plane XZ. Even though the core of the jet ends at about $x/d=3.5$, the velocity profiles do not collapse into a similar curve for the sections measured. Conversely, less confined jets attained similarity after $6d$ and $8d$ (Chua and Lua 1998); the side walls in Chua and Lua's study are at $37.5d$ away from the centerline jet.

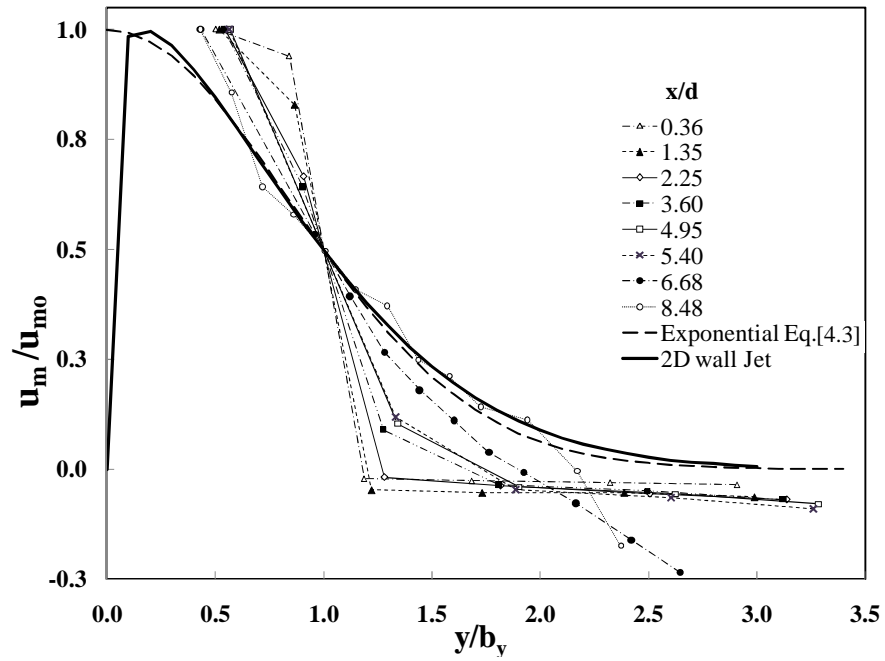


Figure 4.5 Mean velocity distribution of an eccentric jet (center plane XY)

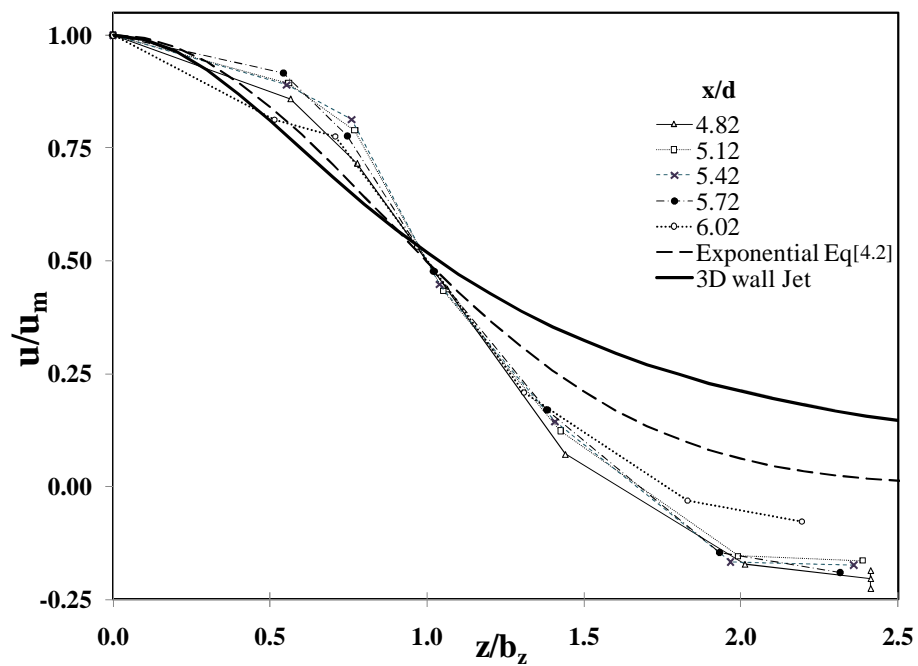


Figure 4.6 Mean velocity distribution of an eccentric jet (center plane XZ)

Velocity profiles in plane XZ show symmetry to the plane $z=0$. Again the velocities do not become similar for the length of measurement (Fig. 4.6). The measured profiles are compared with a circular free jet from Rajaratnam (1976) and an empirical distribution for circular three dimensional wall jets presented by Herlina and Law (2002):

$$[4.16] \quad \frac{u}{u_m} = \frac{1}{(0.965z/b_z)^2+1}$$

Before half width ($z/b_z=1$), the velocity profiles are underestimated by both the free jet and the three dimensional wall jet curves. Beyond this point the counter-flow clearly imposes an upward component (i.e. negative values) from about $z/b_z=1.6$.

4.4.4 Turbulence characteristics

Even though the turbulence levels are different in confined jets, bluff jets and free jets, the same sharp increase in short distances from the nozzle is observed in all of them (Fig. 4.7). The turbulence intensities in the longitudinal direction increase as the jet travels downstream. Larger values correspond to more confined jet enclosures for the same distance downstream of the nozzle pipe. The r.m.s of the turbulence intensity in the streamwise direction ($\sqrt{u'^2}$) normalized by the maximum velocity in each section (u_{mo}) is illustrated in Fig. 4.7a. For $L/d=2.5$ and 3.7 , it is seen to start with an initial value of 0.15 and 0.08, respectively; and it increases to a maximum value of about 0.4 and 0.6 at $x/d=5.5$ and $x/d=8.6$, respectively. Measurements of $\sqrt{u'^2}$ normalized with the jet efflux velocity U_o are presented in Fig. 4.7b. They are compared to the turbulent fluctuations of a less confined jet (Chua and Lua 1998), for which $\sqrt{u'^2}/U_o$ has an initial value close to zero that increases almost linearly up to about $10d$ in the axial direction. Noteworthy is that the jet tested by Chua and Lua (1998) was produced at laminar initial conditions $R_o < 8000$ at emergence (Fig. 4.7b). The increasing trend is typical of jets with a laminar top-hat profile.

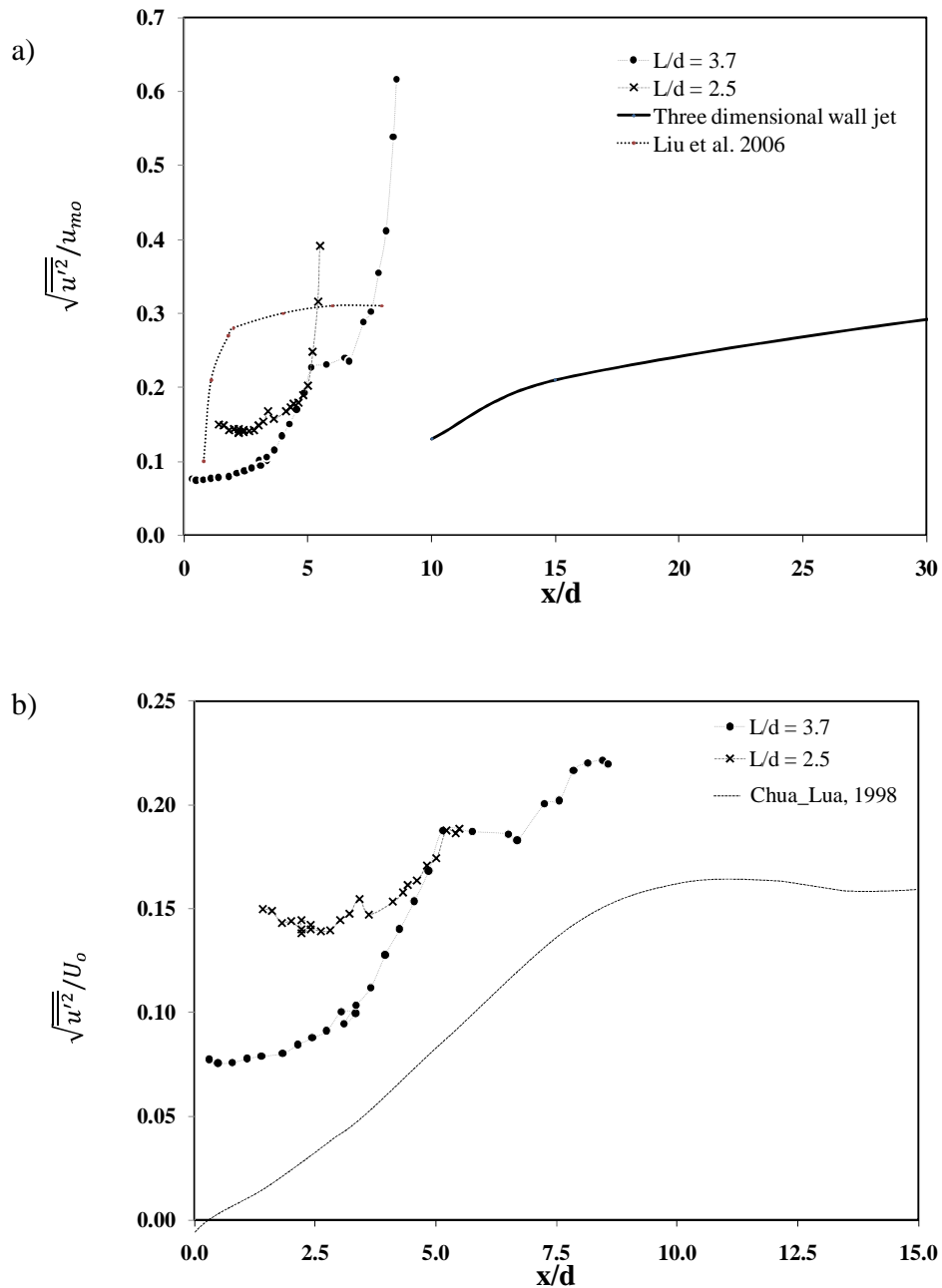


Figure 4.7 Normalized turbulence intensities in the streamwise direction: a)

$$\sqrt{\overline{u'^2}}/u_{mo}; \text{ b) } \sqrt{\overline{u'^2}}/U_0$$

The magnitudes of $\sqrt{\overline{v'^2}}/u_{mo}$ and $\sqrt{\overline{w'^2}}/u_{mo}$ are less than that of $\sqrt{\overline{u'^2}}/u_{mo}$ within the reach of measurements, being larger in the y -direction, possibly due to the wall and the formation of the boundary layer. In an axisymmetric free circular jet,

$\sqrt{u'^2} / u_{mo}$ remains dominant as far as 100 diameters downstream (Wyganski and Fiedler 1969), reaching an almost asymptotic value close to 0.3. The radial component $\sqrt{v'^2} / u_{mo}$ seems to increase very slowly throughout up to a value of 0.19 at $150x/d$ (Panchapakesan and Lumley 1993). The normalized turbulence intensities of the confined jet do not seem to reach asymptotic values in any velocity component within the reach of the measurements. While in a free jet, the two radial components of the turbulence intensities are of the same order, in the case of the confined turbulent jet, the normalized turbulent intensity in the y -direction $\sqrt{v'^2} / u_{mo}$ stays at about 0.06 up to $x/d=3.5$ from where it lies within 30% below the streamwise component $\sqrt{u'^2} / u_{mo}$. The magnitude of $\sqrt{w'^2} / u_{mo}$ in the z -direction has a value of about 0.045 in that same region.

The mean kinetic energy per unit mass is defined as: $K = (u^2 + v^2 + w^2)/2$; where u , v , and w are the mean velocities of the flow in the x , y and z directions, respectively. The values of dimensionless mean kinetic energy $K^{0.5}/U_o$ for the center planes (XY and XZ in Fig. 4.2) crossing the centerline jet axis present a decay in the streamwise direction at an almost constant rate which is comparatively smaller than the rapid decay observed in the transverse directions in both x and y . The turbulent kinetic energy per unit mass K' is defined by $K' = (\overline{u'^2} + \overline{v'^2} + \overline{w'^2})/2$; where u' , v' , and w' are the fluctuating velocities in the x , y and z directions, respectively. Values of $K'^{0.5}$ for the centerline jet are always below 25% of the inflow velocity U_o which suggest zones of low turbulence intensities and relatively large energy dissipation. The bulk of the mean kinetic energy in the center planes XY and XZ is concentrated in the core of the inflow jet (Fig. 4.8). While, the mean kinetic energy in the diffusion region accounts to about 40% of the total (center plane XY), it corresponds to about 60% in the center plane XZ. The recirculating zones, which have negative momentum with respect to the direction of the inflow jet, possibly contribute to the rapid decay in the transverse direction in both jets; similar behaviour has been reported in fish passages (Liu 2004).

The distribution of the Reynolds shear stress shows larger values registered in the axis of the vortices formed in each recirculating zone. That is, a single vortex in the XY plane while two in the XZ plane as the jet pierces the stored water volume in the center. The analysis of typical power spectra $G_u(f)$, $G_v(f)$ and $G_w(f)$ for the turbulent velocity components u' , v' and w' , respectively, where f is the frequency and the spectral density is divided by the corresponding turbulence intensity showed the appearance of the inertial subrange marked by $-5/3$ slope. The Kolmogorov hypothesis states that at sufficiently high Reynolds number, the high-wave number portion of the velocity spectra adopts a universal form. Applying a one-dimensional spectrum of the axial velocity $G_u(k)$ in the inertial subrange (Hinze 1975), we have:

$$[4.17] \quad G_u(k) = A\varepsilon^{2/3}k^{-5/3}$$

where k is the wave number, ε is the rate of energy dissipation and A is a universal Kolmogorov constant with a value of 0.49 for local isotropic turbulence (Pope 2000). The value of ε was obtained doing a non-linear fit in the inertial subrange of the relation $G_u(k)$ and k for the measured values. For a turbulent flow of a sufficiently large Reynolds number, the local isotropic state will be established in the small scale region of spectrum (Monin and Yaglom 1971). It was found that the correlation coefficient spectrum falls rapidly to zero at high wave numbers, which is a consequence of local isotropy. Therefore, the Kolmogorov $-5/3$ law of local isotropic turbulence (Hinze 1975) could be used to estimate the dissipation rate as a first approximation as implemented in other confined settings (Liu et al. 2006)

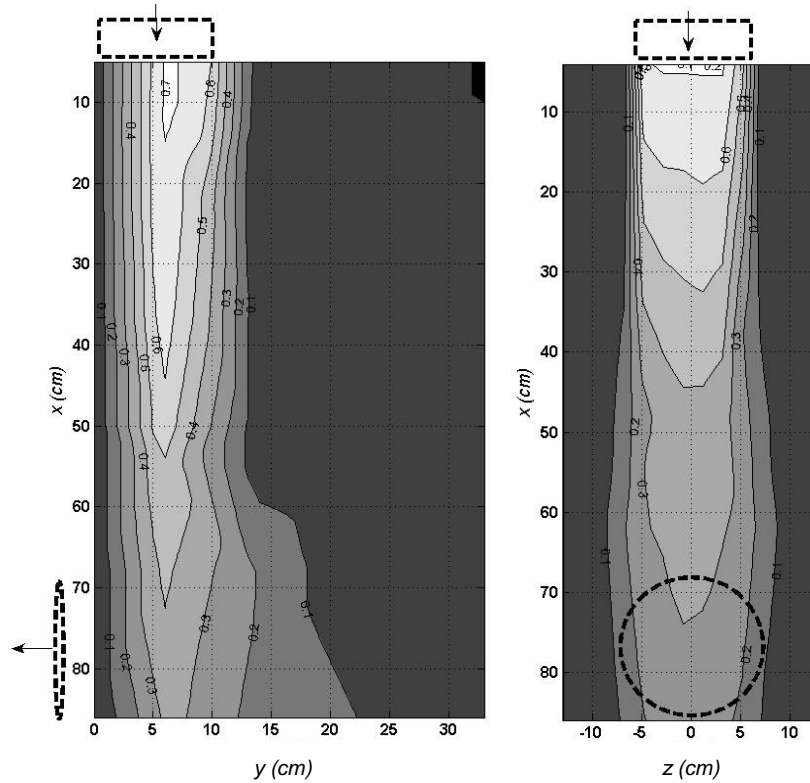


Figure 4.8 Distribution of dimensionless mean kinetic energy $K^{0.5}/U_o$ in center planes XY and XZ

4.5 MODEL PREDICTIONS

To verify the proposed method to compute the energy losses from section 0 to 2, a set of experiments were run under two levels of confinement in an eccentric jet position. Fig. 4.9 shows the comparison between the relative energy losses measured and the corresponding computed values from Eq. [4.11]. The obtained results fall closely to the best fit line, producing a maximum underestimation of 5% for the largest energy losses in a less confined jet ($L/d=3.7$). Note that the losses in the chamber by jet diffusion could represent anywhere between 9 to 0.21 times the losses associated to the entrance to the exit pipe and friction. For the numerical computations of contraction losses, contraction coefficients for a suppressed orifice (flushed with the bottom) were used. Values between 0.45 and 0.75 were measured experimentally (Camino et al. 2011). For practical application, an average value of 0.6 could be used.

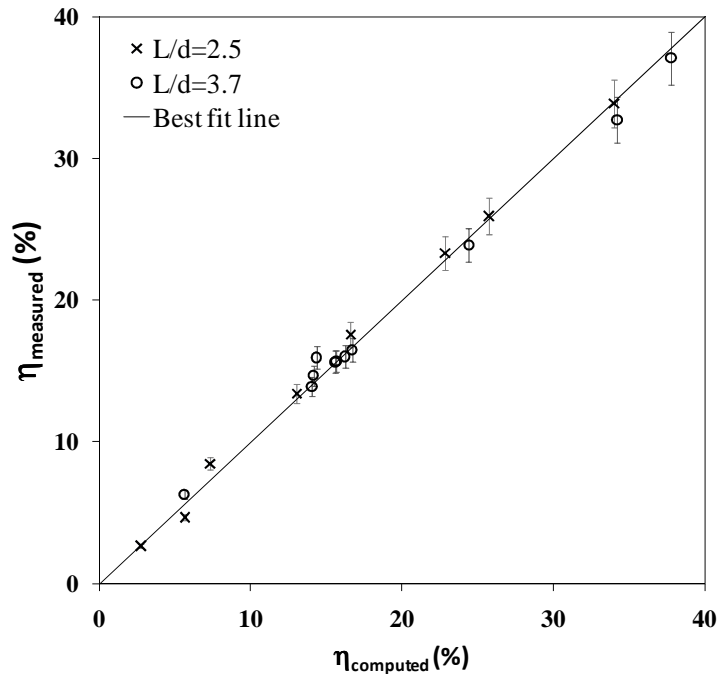


Figure 4.9 Comparison of relative energy losses of the flow from jet onset to exit in outlet pipe

Computed rates of energy dissipation rate for the two levels of confinement show larger dissipation rate along the centerline velocity for smaller level of confinement, i.e. $L/d=3.7$. The computed rates are in all the cases equal or smaller than $1.0\text{m}^2/\text{s}^3$ per unit mass or $1000\text{W}/\text{m}^3$. The average energy dissipation rates per unit mass obtained with Eq. [4.13] are 0.492 and $0.129\text{m}^2/\text{s}^3$ for $L/d=3.7$ and 2.5 , respectively. Implementing Eq. [4.17], rates of energy dissipation of 0.431 and $0.0458\text{m}^2/\text{s}^3$ for $L/d=3.7$ and 2.5 , respectively, were obtained. These results show a reasonable first approximation obtained by assuming the Taylor hypothesis in the center line jet measurements.

4.6 CONCLUSIONS

Energy dissipation inside the pool formed at the base of drop structures is contributed by mechanisms such as jet diffusion. Experimental observations of a circular jet

sliding vertically in a confined chamber showed that a more confining enclosure ($L/d=2.5$) will produce more rapid diffusion of the jet than a less confining condition ($L/d=3.7$) and always larger than the one observed in a free jet. The solid boundaries of a confined chamber produce circulation in the surrounding fluid opposite to the direction of the inflow. The negative momentum of the counterflow that is entrained by the jet will reduce the inflow momentum making the jet to slow down rapidly. At about $x=9d$ (axial distance), the centerline velocity of eccentric and centered jets decays to about 0.3 of the onset velocity for a less confined ($L/d=3.7$). While a centered jet appears to decay at a constant rate, an eccentric one apparently produces two linear gradients or rates of decay. The velocity profiles, in the two perpendicular planes crossing the centerline jet axis, show that similarity was not attained within the reach of measurement; however at sections close to the outgoing pipe, the velocities in the streamwise direction could be approximated by normal distributions.

The kinetic energy flux of the confined jet rapidly decreases through the production of turbulence and viscous dissipation. Measured turbulence intensities increase as the jet travels downstream; larger values for larger levels of confinement for the same distance downstream of the nozzle pipe. The Kolmogorov hypothesis of isotropic turbulence was found useful as a first approximation to calculate the rate of energy dissipation within the chamber. In a similar manner, a comparison of relative energy losses by jet diffusion computed with the theoretical model showed good agreement with the corresponding measurements. Hence, our findings allow optimizing the design of energy dissipators by reducing its size and use of baffle blocks through enhancing the mechanism on jet diffusion with appropriate confinement.

References

- Beltaos, S. and Rajaratnam, N. (1974). "Impinging circular turbulent jets." *J. Hydr. Eng. Div., ASCE*, 100, HY10: 1313-1328.
- Camino, G.A., Zhu, D.Z. and Rajaratnam, N. (2009). "Use of a stacked drop manhole for energy dissipation: A case study in Edmonton." *Can. J. Civ. Eng.*, 36: 1037-1050.
- Camino, G.A., Zhu, D.Z. and Rajaratnam, N. (2011). "Hydraulics of Stacked Drop manholes." *J. Irrig. Drain. Eng., ASCE*: In press.
- Canbazoglu, S. and Bozkir, O. (2004). "Analysis of pressure distribution of turbulent asymmetric flow in a flat duct symmetric sudden expansion with small aspect ratio." *Fluid Dynamics Research*, 35(5): 341-355.
- Chua, L.P. and Lua, A.C. (1998). "Measurements of a confined jet." *Phys Fluids*, 10(12): 3137-3144.
- Garcia, C.M., Cantero, M.I., Nino, Y. and Garcia, M.H. (2005). "Turbulence measurements with acoustic doppler velocimeters." *J. Hydraul. Eng, ASCE*, 131(12): 1062-1073.
- Goring, D.G. and Nikora, V.I. (2002). "Despiking acoustic doppler velocimeter data." *J. Hydraul. Eng, ASCE*, 128(1): 117-126.
- Herlina and Law, A.W.K. (2002). "Measurements of turbulent mass transport of a circular wall jet." *Int. J. Heat Mass Transfer* 45(24): 4899-4905.
- Heskestad, G. (1965). "A generalized Taylor hypothesis with application for high Reynolds number turbulent shear flows." *J. Appl. Mech*, 32: 735-739.
- Hinze, J.O. (1975). *Turbulence*, McGraw-Hill. 790 pp
- Kraus, N.C., Lohrmann, A. and Cabrera, R. (1994). "New acoustic meter for measuring 3D laboratory flows." *J. Hydraul. Eng, ASCE*, 120(3): 406-412.
- Law, A.W.-K. and Herlina (2002). "An experimental study on turbulent circular wall jets." *J. Hydraul. Eng, ASCE*, 128(2): 161-174.
- Liu, M. (2004). "Turbulence structure in hydraulic jumps and vertical slot fishways". Doctoral thesis. Civil and Environmental Engineering. University of Alberta: 313p
- Liu, M., Rajaratnam, N. and Zhu., D.Z. (2006). "Mean flow and turbulence structure in vertical slot fishways." *J. Hydraul. Eng, ASCE*, 132(8): 765-777.
- Liu, M., Zhu, D.Z. and Rajaratnam, N. (2002). Evaluation of ADV Measurements in Bubbly Two-Phase Flows. *Conf. on Hydraulic Measurements and Experimental Methods*, Estes Park, CO, ASCE-EWRI & IAHR, 28 July 2002 -1 August 2002.
- Lohrmann, A., Cabrera, R. and Kraus, N.C. (1994). Acoustic-doppler velocimeter (ADV) for laboratory use. *Proc. Symposium on Fundamentals and Advancements in Hydraulic Measurements and Experimentation*, Buffalo, New York, August 1-5, 1994.
- McCarthy, M.J. and Molloy, N.A. (1974). "Review of Stability of Liquid Jets and the Influence of Nozzle Design." *The Chemical Engineering Journal*,(7): 1-20.
- Mehta, P.R. (1981). "Separated flow through large sudden expansions." *Journal of the Hydraulics Division, ASCE*, 107(HY4 Proc. Paper, 16206): 451-460.

- Monin, A.S. and Yaglom, A.M. (1971). *Statistical Fluid Mechanics: Mechanics of turbulence*. Cambridge, Mass., MIT Press. 770 pp
- Nortek (2004). "Vectrino Velocimeter. User guide". Vangkroken, Norway.
- Padmanabham, G. and Gowda, B.H.L. (1991). "Mean and turbulence characteristics of a class of three-dimensional wall jets. Part 1. Mean flow characteristics." *J Fluid Eng-T ASME* 113(4): 620-628.
- Panchapakesan, N.R. and Lumley, J.L. (1993). "Turbulence measurements in axisymmetric jets of air and helium. Part 1. Air jet." *J. Fluid Mech.*, 246: 197-223.
- Pedersen, F.B. and Mark, O. (1990). "Head losses in storm sewer manholes: submerged jet theory." *J. Hydraul. Eng, ASCE*, 116(11): 1317-1328.
- Pope, S. (2000). *Turbulent flows*. Cambridge, United Kingdom. 771 pp
- Rajaratnam, N. (1976). *Turbulent Jets*. Amsterdam, Elsevier Scientific Publishing Company. 304 pp
- Rajaratnam, N., Johnston, G.A. and Barber, M.A. (1993). "Energy dissipation by jet diffusion in stormwater drop shafts." *Can. J. Civ. Eng.*, 20(3): 374-379.
- Rajaratnam, N., Mainali, A. and Hsung, C.Y. (1997). "Observations on flow in vertical dropshafts in urban drainage systems." *J. Environ. Eng., ASCE*, 123(5): 486-491.
- Rajaratnam, N. and Pani, B.S. (1974). "Three-dimensional turbulent wall jets." *J. Hydr. Eng. Div., ASCE*, 100(1): 69-83.
- Rodi, W. (1982). *Turbulent Buoyant Jets and Plumes*. Oxford, Pergamon Press. Ltd. 184 pp
- Rusello, P.J., Lohrmann, A., Siegel, E. and Maddux, T. (2006). Improvements in acoustic Doppler velocimetry. *7th Int. Conf. on Hydroscience and Engineering (ICHE-2006)*, Philadelphia, USA, Sep 10 – Sep 13.
- Shammaa, Y., Zhu, D.Z. and Rajaratnam, N. (2005). "Flow upstream of orifices and sluice gates." *J. Hydraul. Eng, ASCE*, 131(2): 127-133.
- Shinneeb, A.M., R., B. and J.D., B. (2010). "Confinement effect in shallow water jets." *J. Hydraul. Eng, ASCE*, 10.1061/(ASCE)HY.1943-7900.0000306((July 2010)).
- SonTek (1997). "MicroADV (Acoustic Doppler Velocimeter) Principles of Operation". SonTek Technical Notes. San Diego, SonTek. <http://www.sontek.com/>.
- Verhoff, A. (1970). "Steady and pulsating two-dimensional turbulent wall jets in a uniform stream". *Princeton University Rept. No. 723*.
- Voulgaris, G. and Trowbridge, J.H. (1998). "Evaluation of the acoustic Doppler velocimeter (ADV) for turbulence measurements." *Atmos. Ocean. Technol.*, 15(1): 272-289.
- White, C.M. and Nemenyi, P. (1942) "Report on research on fishpasses", *Institution of Civil Engineers*, London, United Kingdom. pp. 32-59
- Wu, H. and Patterson, G. (1989). "Laser-Doppler measurements of turbulent-flow parameters in a stirred mixer." *Chem. Eng. Sci.*, 44(10): 2207-2221.
- Wu, S. and Rajaratnam, N. (1990). "Circular turbulent wall jets on rough boundaries." *J. Hydraul. Res.*, 28(5): 581-589.

Wynanski, I. and Fiedler, H. (1969). "Some measurements in the self-preserving jet." *J. Fluid Mech.*, 38(pt 3): 577-612.

Notation

a = constant of proportionality

A = universal Kolgomorov constant

A_o = area of the jet at the emergence

b_y = distance in y -direction where $u_m = u_{mo}/2$

b_z = distance in z -direction where $u = u_m/2$.

d = diameter of the inlet pipe

E = kinetic energy flux

E_T = total energy per unit volume at the exit of the jet

f = pipe friction factor

f_1, g_1 = functional relations

f_R = user-defined frequency

F = dimensionless parameter

G_u, G_v, G_w = power spectra for the velocity components u', v' and w' , respectively

h = distance normal to the plate from one edge of the circular orifice

h_o = depth of water in the chamber

h_c = losses due to sudden contraction into the exit pipe

h_f = loss due to pipe friction

H = total energy head

k = wave number

K = mean kinetic energy per unit mass

K' = turbulent kinetic energy per unit mass

l = length of the outgoing pipe

L = length scale of the cross sectional area of the chamber

L_y = length of the chamber cross section (y -direction)

L_z = width of the chamber cross section (z -direction)

L_r = energy-containing eddy length scale

L_i = length scale based on an integral time scale from the power spectrum ($i = s, n, z$)

n = exponent for the decay of maximum velocity

Q = jet flow rate at an axial distance x from the nozzle

Q_o = flow rate at the emergence ($= U_o A_o$)

R_o = Reynolds number

R = hydraulic radius

u, v, w = velocities in x, y and z directions, respectively

$\overline{u'^2}, \overline{v'^2}, \overline{w'^2}$ = turbulence intensities in x, y and z directions, respectively

u_m = velocity at the central plane ($z = 0$)

u_{mo} = maximum value of u_m which occurs at a normal distance δ from the wall

U_o = jet exit velocity

U_c = convective velocity

$V = \sqrt{u^2 + v^2 + w^2}$ = total velocity at any distance x

$\bar{\epsilon}$ = average rate of energy dissipation

η = relative energy losses

$\eta_y = y/b_y$ = length scale in y -direction

$\eta_z = z/b_z$ = length scale in z -direction

ν = kinematics viscosity

Subscripts

0 = section at the emergence of the jet

1 = section across the chamber at a level aligned with the axis of the outlet pipe

2 = section at the exit pipe

CHAPTER 5: FLOW OBSERVATIONS IN A TALL PLUNGING DROP SHAFT*

5.1 INTRODUCTION

Common practice in urban drainage systems is the implementation of large dropshafts to meet elevation differences in the system. Mostly in North America, these structures are designed to have a slender geometry, i.e. the cross sectional dimension is much smaller than the height of the shaft, to optimize excavation and construction costs.

Model studies conducted on plunging dropshafts at St. Anthony Falls Hydraulic Laboratory proposed design configurations effective in dissipating energy and removing entrained air (Anderson and Dahlin 1975; Dahlin and Wetzel, 1982). Plunging type dropshafts of rectangular and circular cross sectional shape have been systematically studied in the past (Rajaratnam et al. 1997; Chanson 2004; Granata et al 2010 and others). Rajaratnam et al. (1997) presented an exploratory study carried out in a model with a shaft diameter (D_s) equal to twice the inlet diameter and drop height equal to $6.6D_s$. They reported for the first time that significant relative energy losses (between 80 to 95%) were achieved within the structure. Observations on the flow patterns related to the relative water discharge (up to $Q^*=1.5$ where $Q^* = Q / \sqrt{gd^5}$ and Q is the water discharge; g , the gravity constant and d , the inlet diameter) were detailed. Relative air flow rates were computed from pressure measurements in a short pipe with a bell-mouth entrance serving as single entry air vent.

* A paper based on the content of this chapter is currently being prepared for submission to the Journal of Hydraulic Engineering, ASCE

Chanson (2004) studied seven dropshafts: a) five shafts designed to investigate the effects of shaft pool or sump (pool height=0 and 0.32 m), outflow direction (90° and 180°), and drop height ($h=0.55$ and 0.87 m); and, b) two geometries were geometrically scaled (scaling ratio 3.1). The presence of a sump allowing a pool at the base of the shaft showed little effect on the energy losses. Conversely, greater losses were observed in a dropshaft with 90° outflow direction. The drop height showed little effect on the energy losses when comparing dropshafts with no pool and 90° outflow. Similarly, the shaft pool, outflow direction, and shaft height had little effects on the dimensionless water level in the shaft pool. Relatively close agreement was observed between model and prototype in terms of energy losses and pool height. Instead, observations on bubble penetration depths and recirculation times presented marked differences between model and prototype (Chanson 2004). Consistently smaller bubble swarm depths were observed in prototype.

In a similar way, Jalil (2009) studied a dropshaft with variable drop heights. His results revealed that the air entrainment for a specific dropshaft height increases with increasing water discharge, and for a specific discharge, it increases with increasing dropshaft height, more so for $h/D_s \geq 6.6$. The energy dissipation in the plunge flow dropshaft also increased with increasing dropshaft height, and for a specific dropshaft height decreases with increasing the water discharge.

Chanson (2002) firstly classified three flow regimes in a rectangular dropshaft dependent on the geometry and impingement location. Five sub-regimes were disaggregated from the initial three by Granata et al. (2010). They also provided a criterion of regime classification based on the parabolic trajectory of the falling jet and the geometry of the shaft. Granata et al. (2010) obtained empirical relations for local energy losses related to I as well as pool depths in terms of drop height, shaft diameter and flow rate. In terms of aeration, two regimes were proposed: a) Aeration Regime I with a direct ventilation of the downstream pipe from the manhole; b) Aeration Regime II if downstream pipe ventilation is cut down by outlet submergence or jet spreading. Particular geometries of plunging drop structures are enlisted in

Table 5.1. The inflow conditions as well as the geometry of the design define the flow patterns expected in drop structure.

On the other hand, experimental studies on air entrainment are challenged with the absence of appropriate model scaling to extrapolate results to prototype. Model predictions often underestimate the amount of air actually entrained in prototype (Falvey 1980). While a Froude model can model reasonably well the water flow, it does not describe adequately the entrainment and entrapment of air at a free surface. Chanson (2007) carried out an experimental investigation in a near-full size Roman dropshaft of plunging type. Air-water flow properties were measured with a single tip conductivity probe. Particle residence times were recorded with digital chronometers and using neutrally buoyant particles. However, there are still aspects of the hydraulics as well as the air demand and energy dissipation processes that were not fully described and analyzed.

For this study, a large scale model was built having the ratio shaft diameter to drop height as the one encountered in typical prototype structures in North America (Fig. 5.1). The aim of this experimental work is to explore the nature of the falling water in the air space of the dropshaft; i.e. distribution of the water concentration and local velocities across the shaft at different elevations from the inlet pipe. In addition, we pursue reliable measurements of air demand and assess the energy losses achieved within the structure.

Table 5.1 Geometry of previous models on plunging drop manholes and dropshafts

AUTHOR	Inlet cross-section		Approach flow	Shaft section			Outlet conduit
				Shape	Ratio* D_s/d	Slenderness ratio* h/D_s	
Gayer (1984)	circular	d=0.30m	supercritical ($F_o=6\sim 8$) ⁺	circular	3.3	0.5 ~ 0.8	d
Christodoulou (1991)	circular	d=0.19m	supercritical	circular	2.6	0.1 ~ 2.6	d
Rajaratnam (1997)	circular	d=0.15m	subcritical	circular	1.9	6.6	1.9d
Calomino et al. (1999)	circular	d=0.10m	supercritical	circular	1.5 ~ 4	0 ~ 3.3	d
Chanson (2004)	rectang.	b =0.50m	subcritical	rectangular	1.5	2.2 ~ 3.6	1.3b; b
		b=0.16m		rectangular			1.3b
De Marinis (2007)	circular	d=0.20m	supercritical	circular	5.0	2.0	d
Jalil (2009)	circular	d=0.15m	subcritical	circular	2.0	10.8 7.4	d; 2.0d
Camino (2009) offset SDM	circular	d=0.19m	subcritical, supercritical & full	rectangular	3.6	1.0	d; 1.3d
Camino (2010) symmetric SDM	circular	d=0.19m	subcritical, supercritical & full	rectangular	3.0	1.3; 2.0; 2.7	d
Granata et al. (2010)	circular	d=0.20m	supercritical	circular	5.0	2.1; 2.5; 3.1	d
62 Avenue dropshaft city Edmonton	circular	d=1.20m	variable	circular	1.0	19.7	1.33d
Current work	circular	d=0.19m	subcritical	circular	2.0	19.8	2.0d

d= inlet diameter; b = inlet width

*In the case of rectangular shafts D_s is taken as the square root of the cross sectional area

⁺approaching Froude number

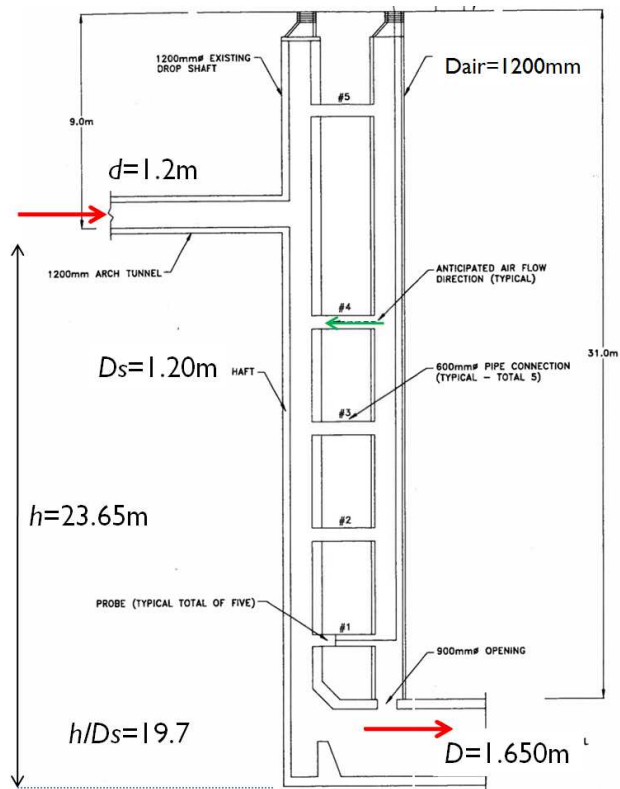
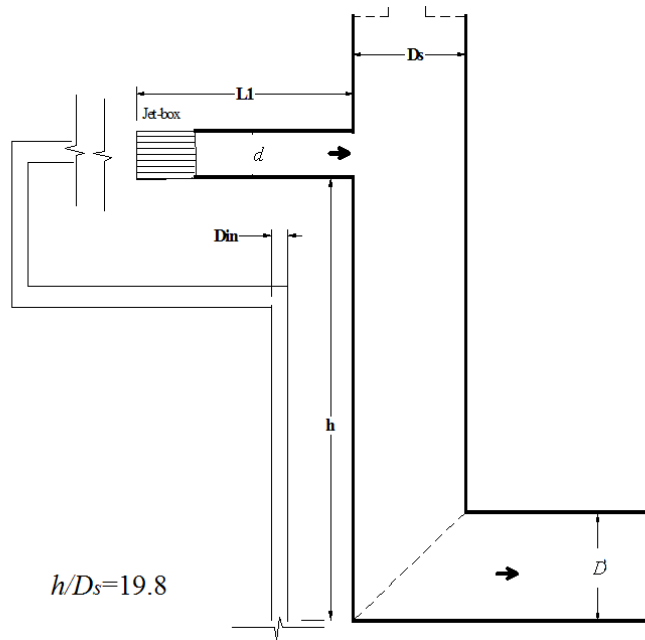


Figure 5.1 Sketches of a tall dropshaft in: a) model and b) prototype of typical ratio drop height to diameter of the shaft of the city of Edmonton (source: A.E. 2008)

5.2 EXPERIMENTAL SETUP AND PROGRAM

Plexiglas transparent pipes were used to construct a model structure of a slender plunging dropshaft in the lab (Fig. 5.2). A horizontal inlet pipe (diameter $d=0.19\text{m}$) was connected to a circular shaft (diameter $D_s=0.38\text{ m}$) with a straight entrance. The outgoing pipe (diameter $D=0.38\text{ m}$) was connected to the shaft with an elbow junction. The dimensions of the structure are summarized in Table 5.2. If the model dropshaft would represent a prototype dropshaft with a shaft diameter of 1.20 m as the one monitored for the odour control program in the city of Edmonton (A.E. 2008), the scale ratio will be about three having the same ratio of drop height to shaft diameter.

Table 5.2 Geometry of the model plunging dropshaft

h (m)	d (m)	D_s (m)	L_{in} (m)¹	L_{out} (m)²	D (m)³	D_s/d	h/D_s	h/d	D_s/D
7.7m	0.19	0.38	1.0	3.0	0.38	2.0	19.8	37.0	1.0

¹ L_{in} = length of the inlet pipe. ² L_{out} = length of the outlet pipe. ³ D = diameter of the outlet pipe

Water flow rates (up to 30 L/s) were recorded with a magnetic flow meter. Flows below 2 L/s were measured volumetrically as they were below the accuracy of the magnetic flow meter. For the range of discharges tested, inflows essentially subcritical were developed, i.e. considering an approach Froude number $F = v_o / \sqrt{(gA/T)}$, where v_o is the inflow velocity, T , top width and A , wetted cross-sectional area of inlet flow. Water flows above $Q^*=0.55$ could maintain a full pipe flow condition in the inflow.

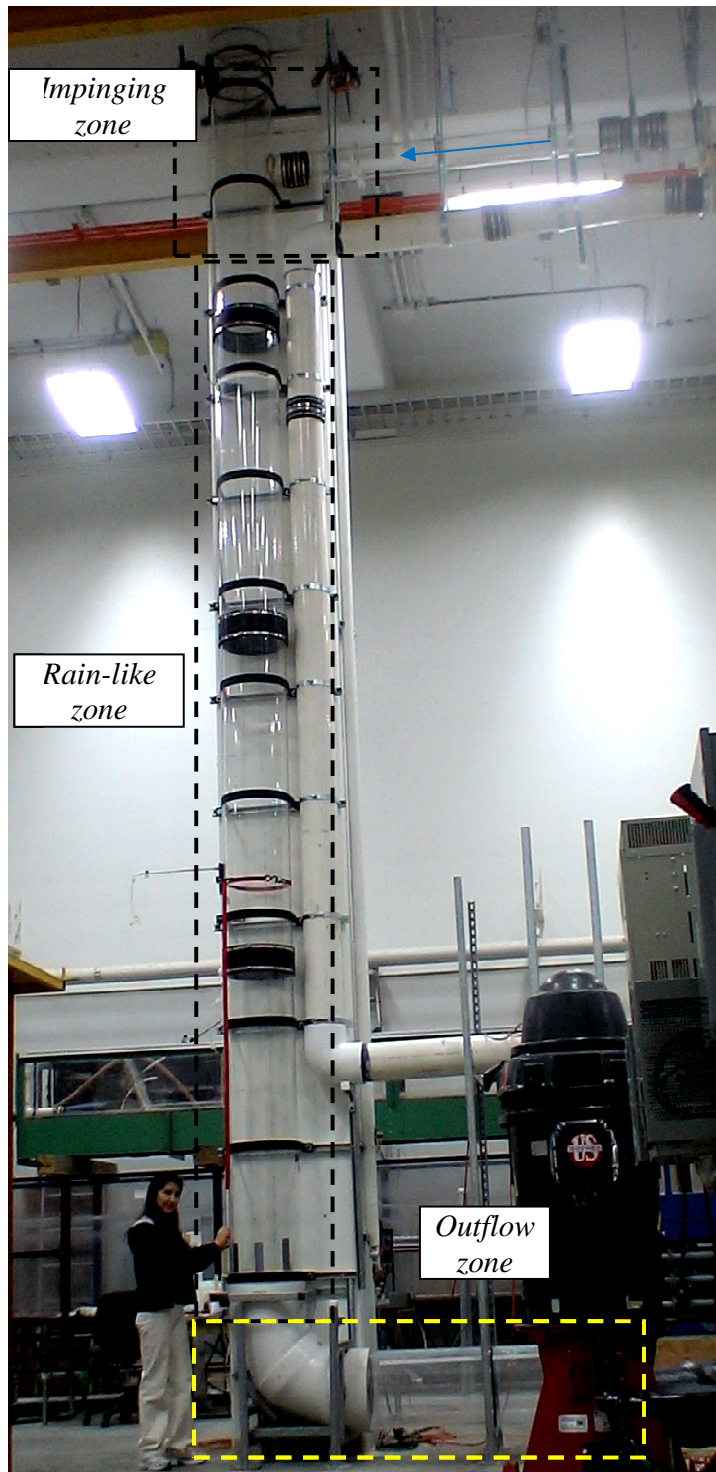


Figure 5.2 Experimental setup and definition zones

Air flow velocities were measured using an air rotating vane anemometer of 0.10m diameter (VelociCalc® Model 5725). The air vane was inserted across the unique air vent of the structure located at a side of the shaft close to the top. Measurements of wind velocity in the air space of the outgoing pipe were taken with a handheld anemometer La Crosse technology model EA-3010U.

Water velocities in the shaft and outlet were extracted from high speed imagery. A high speed camera (©Vision Research v7.3) controlled by Phantom Camera Control Software was used to capture 14-bit images with resolutions 600x800 pixels. Velocities of falling water in the shaft were processed from images sampled at rates above 5000 fps. Good definition images from water within the shaft were captured with appropriate depth of field (~0.30 m) using enough external light to reduce the aperture value and minimizing the shutter speed to ~30 μ s. The location of the camera was kept sufficiently far from the shaft to get enough approximation on measurement from streams away from the actual plane of focus. Errors below 8% are expected from this approximation. Videos from the outflow were captured with Redlake high speed camera (MotionScope 1000S) recording monochrome images at 250 fps and 1000 fps.

Distribution of the water flows across the shaft was attempted using a type of total-pressure probe of 2.4 mm inner diameter resembling a rain gauge. The probe was connected to graduated cylinders to collect water over a certain period of time. Similar samplers were previously used to capture sand particles in debris flows (Mainali and Rajaratnam, 1994). Special care was placed in having the connecting tube as short as possible (0.40 m in length), with downward slope and the end open to atmospheric pressure. Even though, the capture efficiency of the probe was acknowledged to be below 100%, results from probes of different diameters were proved to be consistent in a dimensionless form (Fig. 5.3). In general, the smallest diameter probe was chosen to produce representative local water concentrations from this direct water sampling technique.

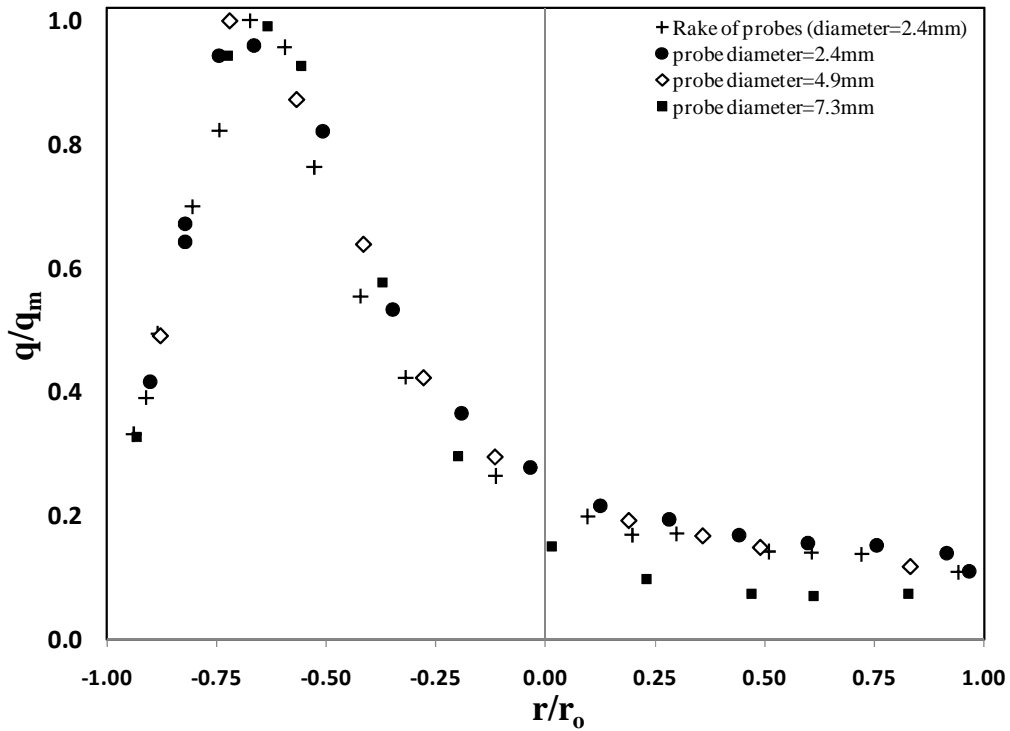


Figure 5.3 Calibration of total-pressure probes of 2.4mm, 4.9mm, 7.3mm and rake of 2.4mm probes for $Q^*=0.64$

5.3 EXPERIMENTAL RESULTS AND DISCUSSION

5.3.1 Data conditioning

An investigation of the sampling time required to get converged values of mean air velocities with an air vane anemometer was carried out in a first set of experiments. The length of the sampling should be long enough to average the turbulent fluctuations resulting from the turbulent water flow and the combined action of air entrainment, entrapment and detrainment in the shaft (e.g. at $Q^*=0.56$ in Fig. 5.4). An inspection of the variability of mean velocity outputs showed that the lower range of flows (i.e. $Q^*<0.2$) controls the sampling time. Experiments taken at 0.1 Hz for 60 s duration and at 1 Hz for 300 s duration did not show significant effect of the sampling time between 1 min. and 5 min. on the relative air flow rate β for Q^* above 0.2; however it affected β on the lower range of discharges in more than 25% difference.

Hence a sampling time of 300 s was chosen.

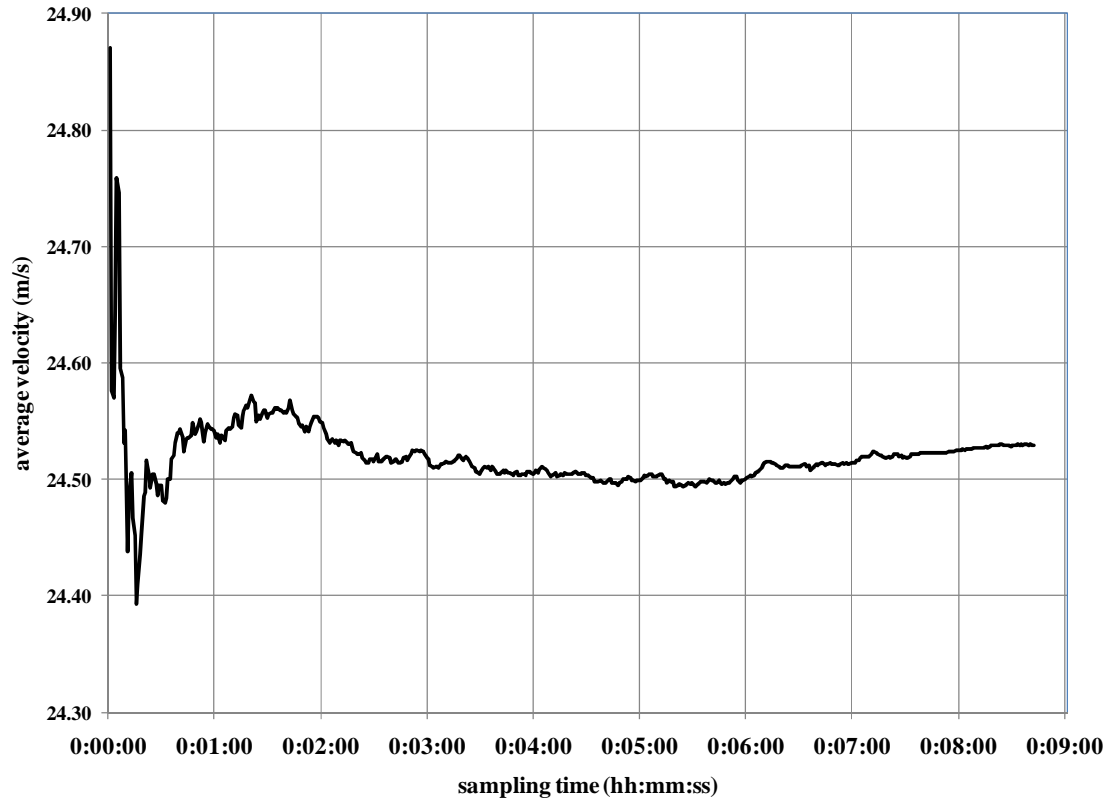


Figure 5.4 Convergence of the sampling time in the air velocity measurements for a dimensionless water discharge $Q^* = 0.56$

The setup was constructed in the Blench Hydraulics Lab of University of Alberta that has about 9m floor-to-ceiling height. Noise in the air flows were expected from different sources: a) air vane calibration due to drifts and nonlinearities; b) Variation on the water flow rate during the experiment verified by the fluctuations in the readings on the magnetic flow meter; and c) the ambient air in the laboratory as it is used as air reservoir for ventilation/flow for the building (personal communication with Lab technicians). When the lights of a room in the building are turned on/off, the ambient temperature automatically lowers down and the ventilation system is activated producing air flows in the lab.

An examination on the noise levels on the air flow measurements was conducted at

off-pump condition when the readings are expected to be zero and on-pump at zero flow. Air velocity readings at off-pump condition for a period of 24 hours are shown in Fig. 5.5. The measurements were started at the end of a set of experiments. A maximum air velocity of 0.55m/s was measured right after the pump was switched off; this is possibly due to the water draining through the blocked pump which could trickle for a long period of time (approximately two hours in measurements). Noise levels were verified at the beginning of each experiment.

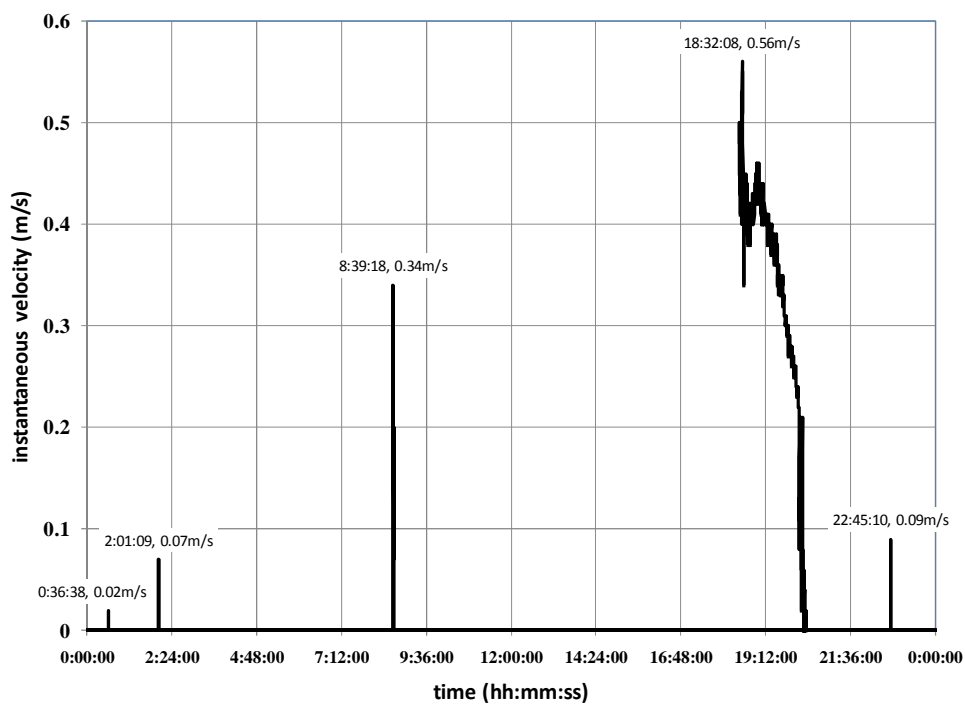


Figure 5.5 Instantaneous air velocity under off-pump condition for noise analysis

5.3.2 Qualitative observations on the physics of the flow

The impingement of the inflow jet on the shaft's inner wall directs the flow radially as an oblique impinging jet on a flat surface. The obliquity of the jet appears to be a key parameter defining the nature of the flow (Kate et al. 2007).

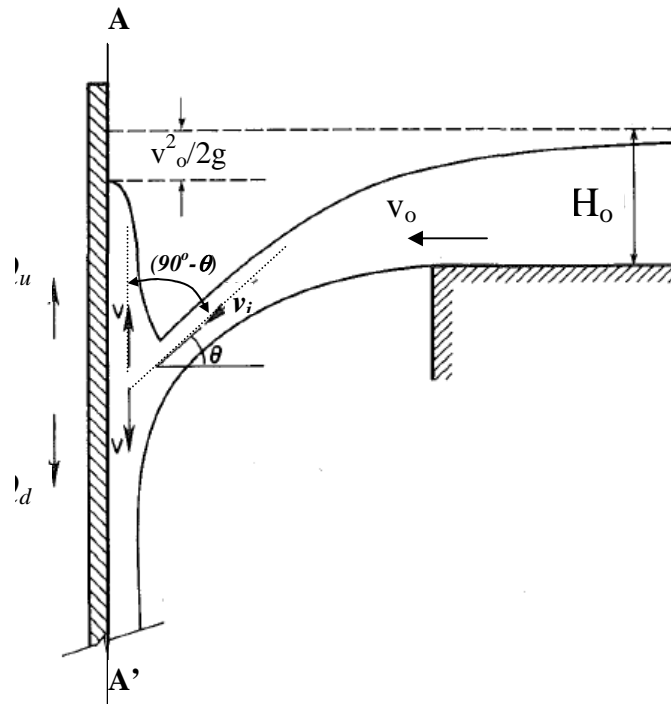


Figure 5.6 Inflow jet at impingement on shaft's wall (adapted from Quick, 1990)

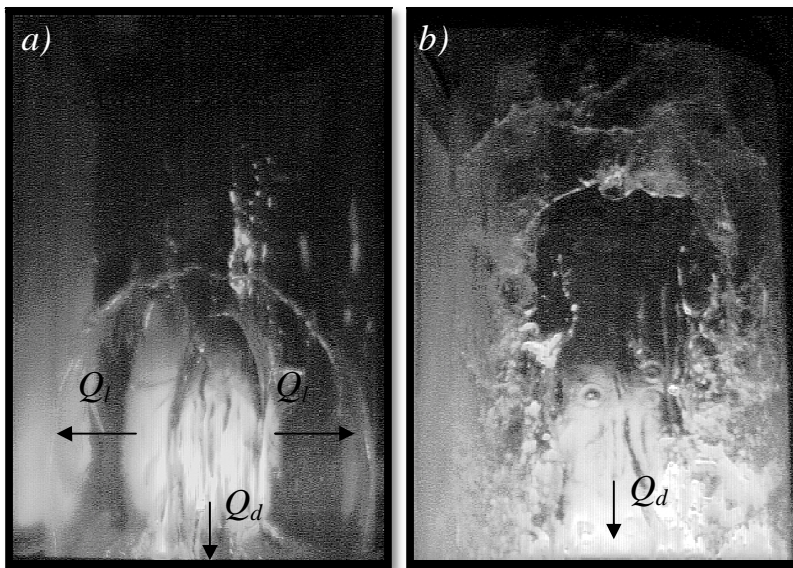


Figure 5.7 Frontal view (section A-A in Fig. 5.5) of the location of impingement on the curved inner periphery of the shaft for a) $Q^*=0.16$ and b) $Q^*=0.54$

Two distinct flows are diverted after the inflow hits on the curved vertical surface of the shaft in a so called impinging zone (see definition sketch in Fig. 5.6). One portion of the water flow forms a central ridge towards the downward direction (Q_d); while a

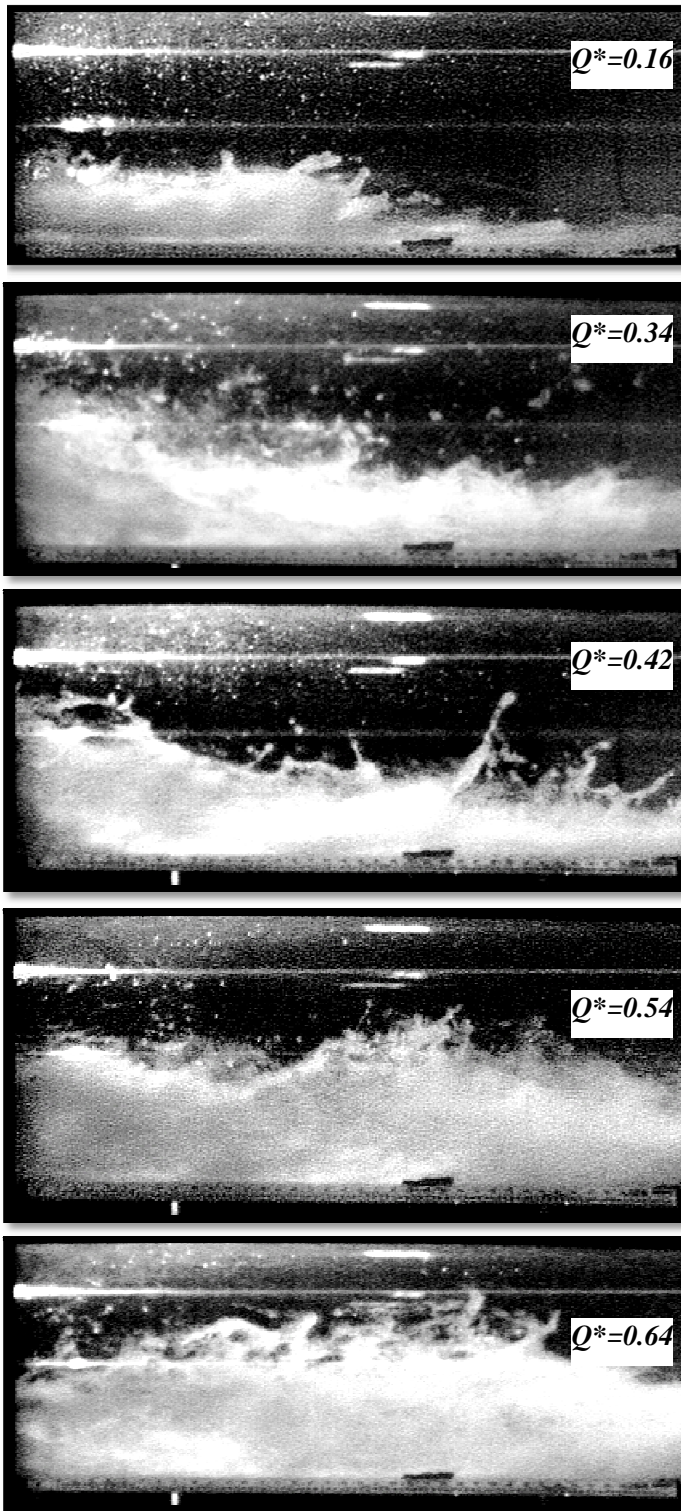
second one produces a water curtain (Q_l) attached to the wall with a peripheral velocity. A minor component of the flow rises upwardly from the impingement location (Q_u) forming a circular hydraulic jump. The relative proportion of the flow in the central ridge and the water curtain was observed to be dependent on the impinging velocity (v_i), angle of impingement (θ), water flow rate and characteristics of the impinging surface; as evidenced in photographs of Fig. 5.7 and direct survey into the flow. Given the inflow jet velocity out of the horizontal pipe and assuming a Bernoulli type jet into the shaft before impingement, one can readily compute the impinging velocity and impinging angle using Eqs. [5.1] and [5.2]:

$$[5.1] \quad v_i = \sqrt{(gD_s / v_o)^2 + v_o^2}$$

$$[5.2] \quad \theta = \text{arcCos}(v_o / v_i)$$

where v_o is the inflow velocity.

Soon after impingement, the water flow acquires a predominantly downward vertical velocity. In this zone of rain-like flow, while the central ridge detaches from the wall forming a major stream into the air space of the shaft, the water flowing adhered to the shaft's inner periphery forming a type of wall jet. In a third zone of outflow comprised by the shaft's bottom and outlet conduit, the water could form a plunge pool in the shaft and being directed towards downstream conduits producing mainly supercritical outflows. Instantaneous photographs of the outlet pipe for a range of flow rates is depicted in Fig. 5.8. Under certain flow rates, an unstable outflow is seen to swirl and shoot offset to the pipe axis. Note that a pool was not able to form for the range of discharges tested.



— 19.8

Figure 5.8 instantaneous scenes of spray formation in the outflow for a range of inflow discharges (MotionScope camera, shutter speed 900 μ s)

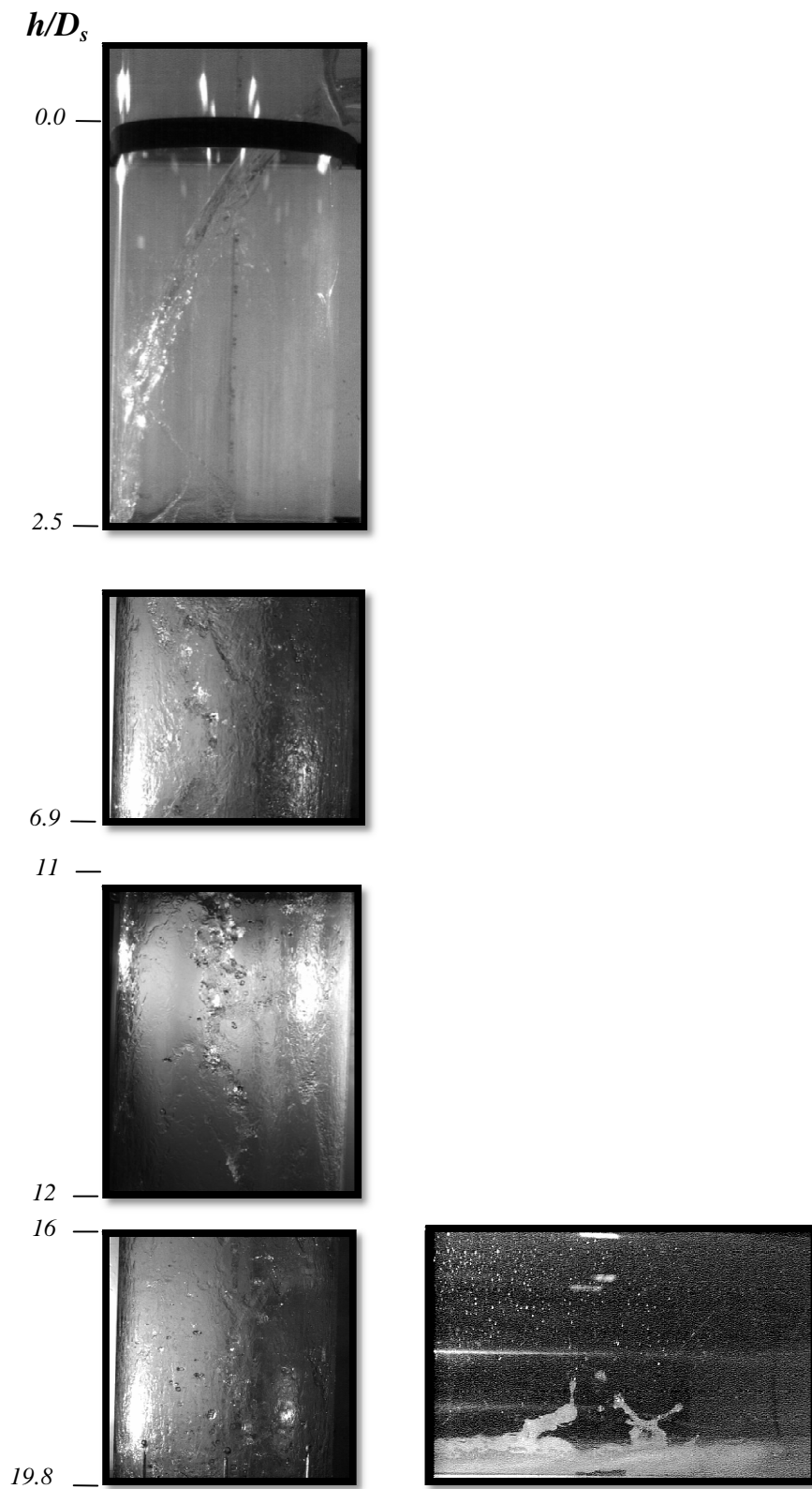


Figure 5.9 Sequence of water streams spreading and diffusing at different elevations of the shaft and outlet for $Q^*=0.16$ (Phantom v7.3 camera, shutter speed $20\mu\text{s}$)

If q is the sampling rate at a point in mL/s and q_m is the maximum value of q in a profile, dimensionless local sampling rates from a rake of 2.4 mm-probes were obtained at four elevations of the shaft; those are at $h/D_s=7, 12, 15$ and 17 . The rake of thirteen probes was traversed horizontally aligned with the main direction of the flow (i.e. inflow-outflow direction). From high speed imagery, it was visualized as a distinct water stream of qualitatively large concentration departing from the central ridge (Fig. 5.9). As the inflow discharge decreases, the central ridge appears to bounce further away from the impingement wall towards the opposite side of the shaft (Fig. 5.10). Kibar et al. (2010) investigated the behaviour of inclined water jets onto vertically located surfaces. They reported that in hydrophobic surfaces (Li et al. 2007), contra-intuitively the jet bounce back from the surface in a so called reflection pattern very much as the ridge formed in the downward flow along the shaft.

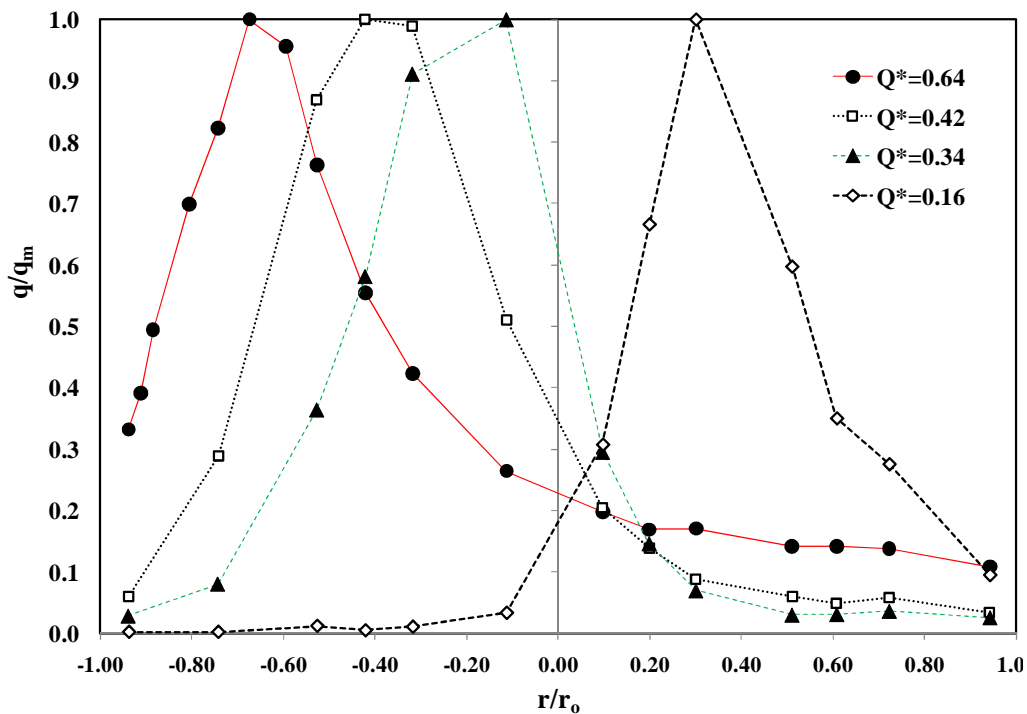


Figure 5.10 Dimensionless water sampling rate q/q_m in the main direction (inflow-outflow) at a section $h/D_s=17$ distance from the invert inlet elevation (negative values in x-axis are to distinguish the impingement side of the shaft at $r/r_o=-1$)

Kibar et al. (2010) observed that small size jets of few millimetres in diameter project water sheets over a larger area on the surface at higher jet velocities and inclination angles. Similarly, water spreads on the shaft's surface in a thin water sheet of parabolic shape and sharp vertex for small flow rates (up to about $Q^*=0.04$). The water curtain covers less than half the inner periphery of the shaft. From about $Q^*=0.13$, the water sheet develops helical motion with lateral rims or wings overlapping in the opposite face of the wall. The flow embraces the whole internal periphery of the shaft within $2D_s$ distance from the invert of the inlet pipe.

For three inflow water discharges, low ($Q^*=0.16$), medium ($Q^*=0.42$) and large ($Q^*=0.64$), the water flow distribution along the shaft from measurements of q at four shaft elevations show a spread of the core stream in the downward direction (Fig. 5.11). As the streams lose coherence, they release blobs of water, ligaments and drops of variable size. The distribution of the drop sizes and elongation of the ligaments is related to the angle of collision in an oblique collision. This mechanism of drop production suggests that the inflow impingement will affect the initial formation of threads and drops of water too. Apparently, the shape of the bulk liquid flow does not look much different from the one attained from a jet issued by a designed nozzle. Disintegration of water drops, coalescence between blobs, aggregation processes and various types of collision between water particles were visualized with high-speed photography under small inflow rates; large inflows developed thicker wall jets in the periphery that limited visualization.

When observing Fig. 5.11 and the decay of the actual values of q_m , it is tempting to speculate that the water jet forming the core stream diffuses and expands in a similar manner to a submerged jet due to the intense interaction water-air. The dispersion and disintegration of the falling jets is attributed to the shear in the inter-phase water-air as a result of velocity difference between the water jet and its surrounding air. The inner streams are expected to have intense air-water interaction induced by apparent air movements within the shaft.

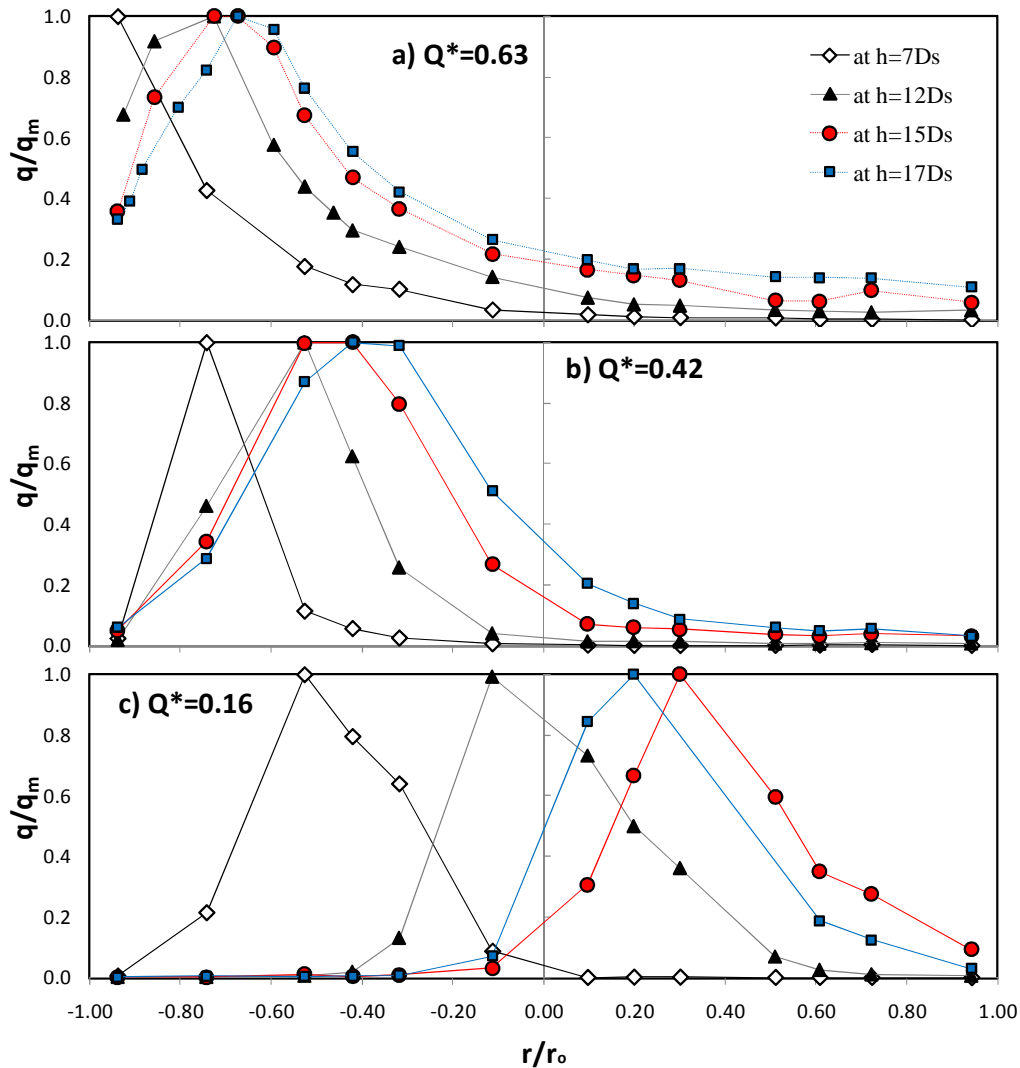


Figure 5.11 Dimensionless water sampling rate q/q_m across the inflow-outflow direction of different sections of the shaft (negative values in x-axis are to distinguish the impingement side of the shaft at $r/r_o=-1$)

Overall, the falling jet formed in the air space of the shaft was observed to have an inner region containing most of the water of the falling flow. This region consisted basically of a core stream as a somehow coherent intermittent jet. An outer region surrounding the first one consisted of smaller streams and drops of less water concentration. Attached to the wall of the shaft, there is a region of flow that might be termed cylindrical wall-jet region that flows along the shaft. Part of the wall jet is seen to detach from the shaft's wall at any imperfection in the surface (e.g. pipe connections), contributing to inner streams within the shaft.

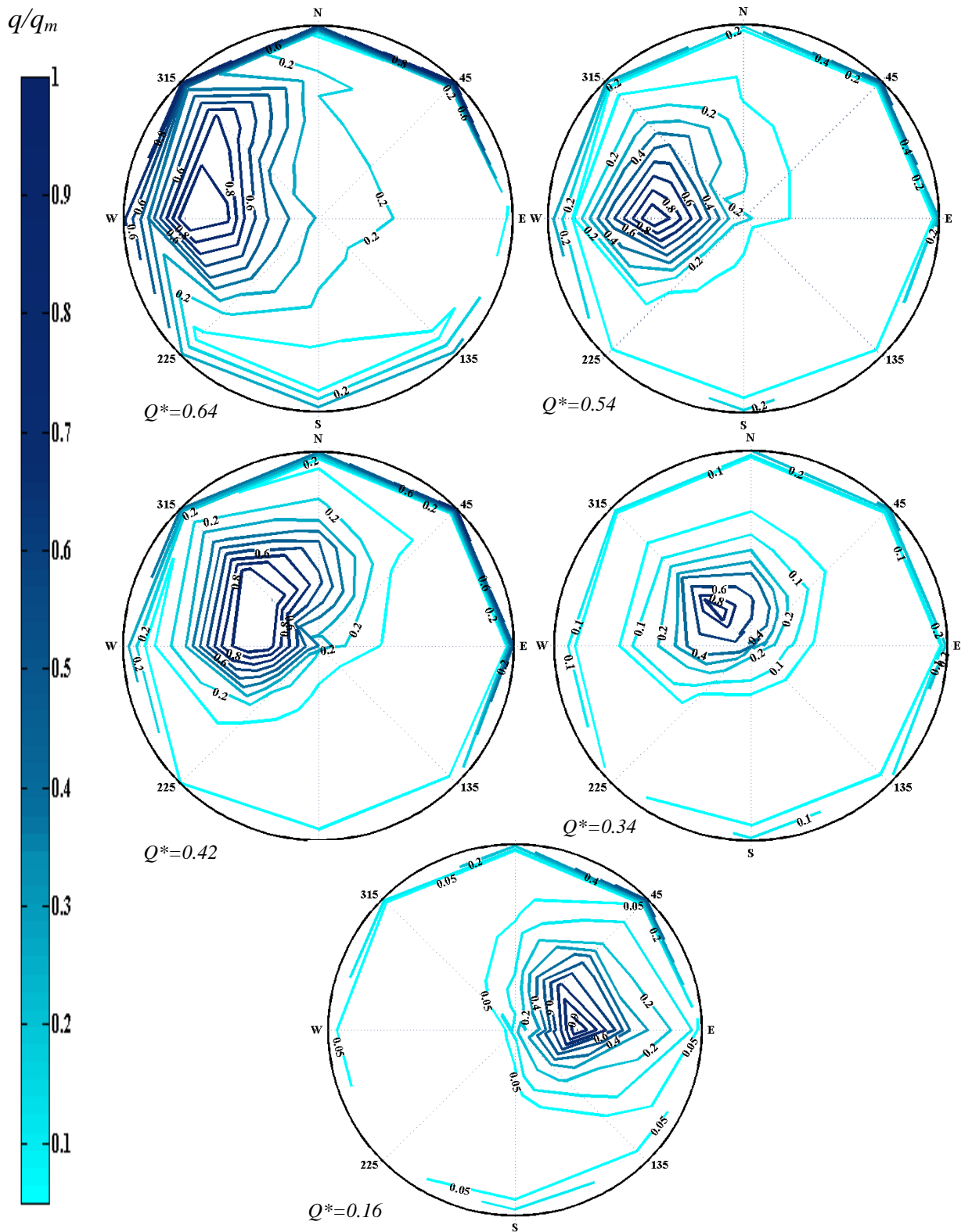


Figure 5.12 Dimensionless contours of water sampling rate q/q_m across a section of the shaft at a distance $h/D_s=17$ from the inlet

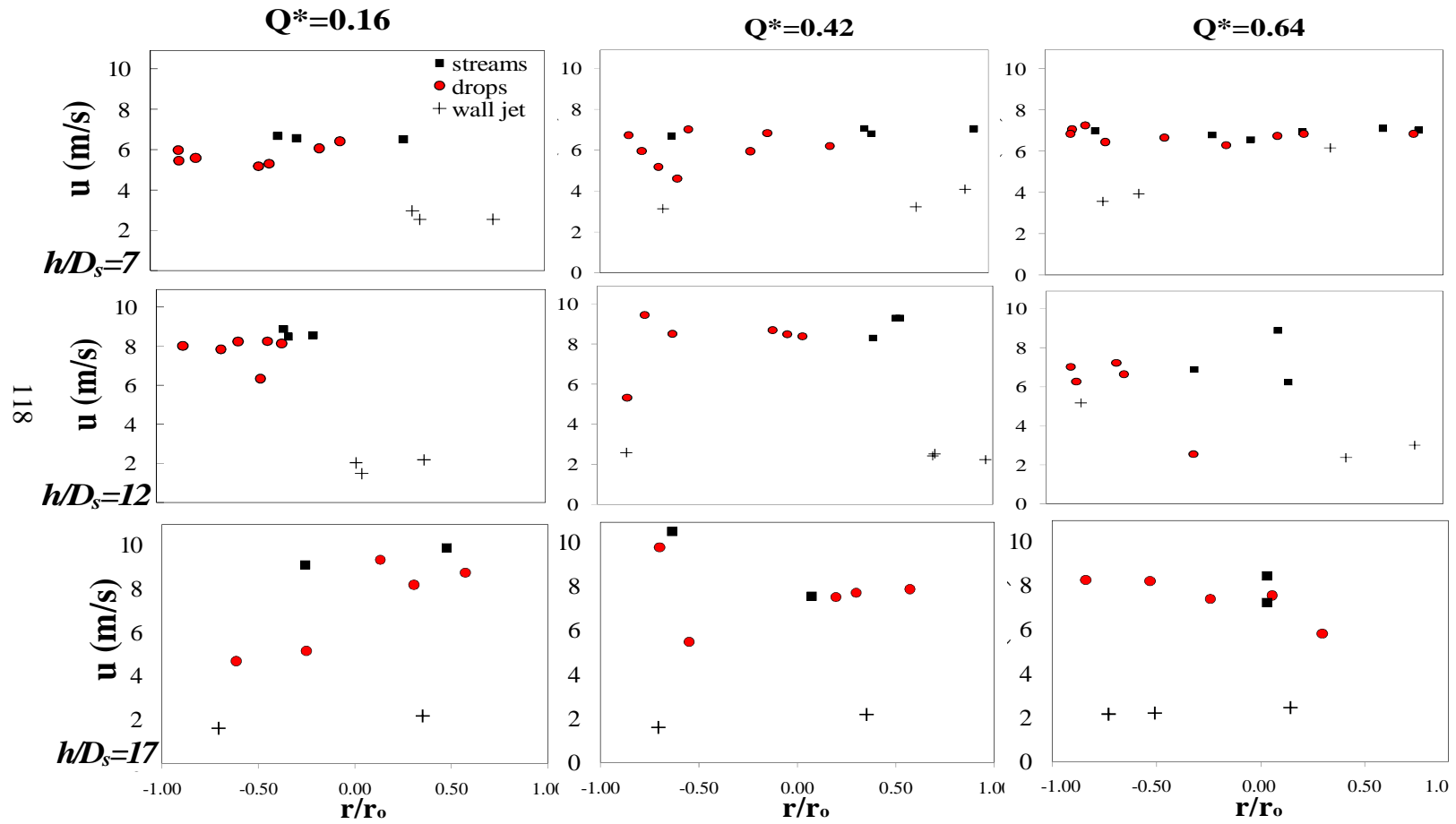


Figure 5.13 Mean relative water velocities along the shaft related to dimensionless drop height h/D_s for a range of discharges

At the furthest measuring cross section of the shaft (i.e. distance $h/D_s=17$ from the inlet pipe), right before the elbow towards the outlet, a set of contours of q/q_m are plotted for a range of inflow discharges (Fig. 5.12). In the graphs, line E-W corresponds to inlet-outlet direction. The concentric contours converge to the region of the core stream.

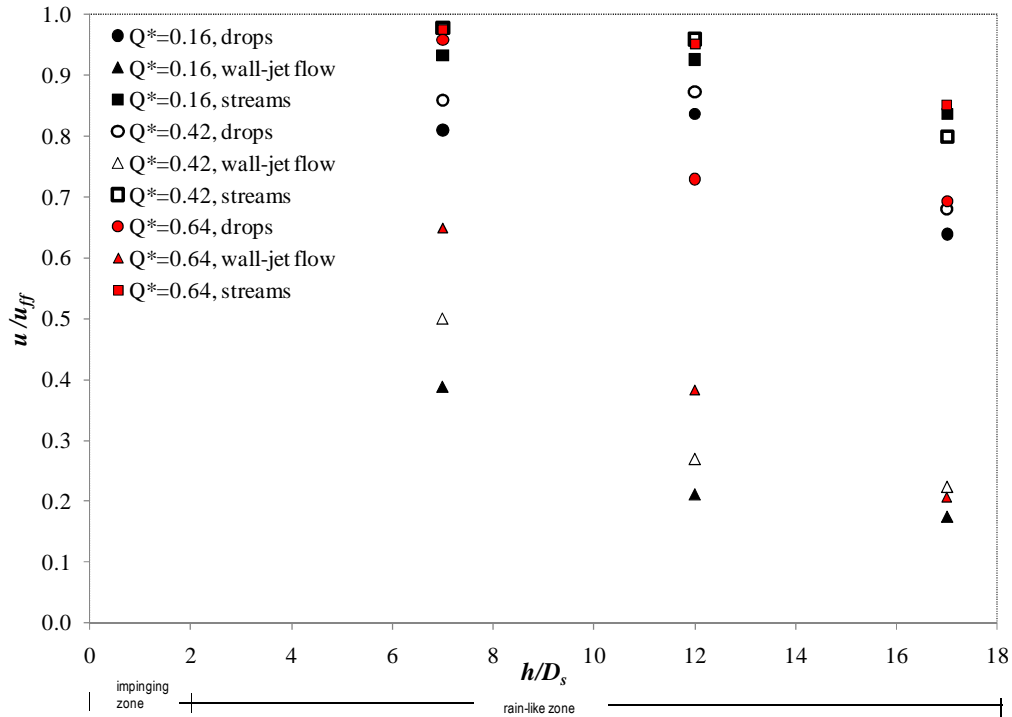


Figure 5.14 Mean relative water velocities along the shaft related to dimensionless drop height h/D_s for a range of discharges

Water velocities were obtained in the three regions of water flow across the shaft. High speed photography and image processing were the techniques employed. The wall jet sliding along the shaft's wall achieves a velocity of about 4m/s in the section closer to the inflow ($h/D_s=7$) and decelerate to about 2.5m/s in the section $h/D_s=17$ (Fig. 5.13). Mean velocities of the wall jet, expressed in relation to the free fall velocity, show a decay to a value below 0.3 at the furthest section tested (Fig. 5.14). The drops and streams achieve in general larger velocities than the wall jet ones. It

could be inferred that the pipe friction produces larger resistance to the flow than the shear stress from air drag. However, the relative velocity of the surrounding air with respect to the velocity of the jet will make a contribution to the stream stability (Hoyt and Taylor, 1977). Similar argument could explain a generally slightly larger velocities of the inner streams than of the drops which have larger interfacial area hence air drag. Overall, the inner flow in the region of core stream and small streams and drops show acceleration; yet, as compared to a Bernoulli jet attaining free fall velocity, they clearly decay (Fig. 5.14).

5.3.3 Energy dissipation

The energy losses inside a tall dropshaft were evaluated for a range of discharges of $0.06 < Q^* < 0.6$. Energy losses were computed from depth measurements using scaled meters in the incoming flow. While depths and water velocities in the outgoing flow were computed from high speed photographs on the outlet flow (Fig. 5.8), where swirling outflows evade accurate depth measurements.

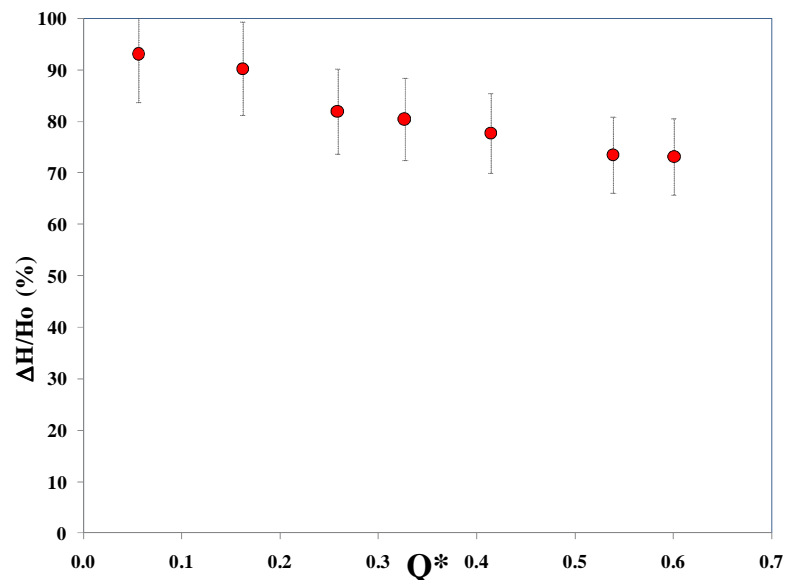


Figure 5.15 Relative energy losses attained in a tall dropshaft for a range of dimensionless flow rates Q^*

Relative energy losses expressed as $\eta = \Delta H / H_o = (H_o - H_3) / H_o$ where $H = z + y + V^2/2g$ is the total head in the inlet (subscript 0) and outlet sections (subscript 3). z is the invert elevation above the datum, y the water depth and V the mean velocity. The datum was fixed at the level of the invert elevation of the outlet pipe. The relative energy losses η were found on average equal to 83% (Fig. 5.15). In Fig. 5.16, a comparison between energy losses achieved within some plunging drop structures in sewer systems show that a tall dropshaft does not produce a significant variation on the losses with a variation in water discharge as do less slender structures (Chanson, 2004; de Marinis et al. 2007). Apparently the drop height expressed dimensionless as h/D_s plays a role in attaining adequate energy losses (see Fig. 5.17).

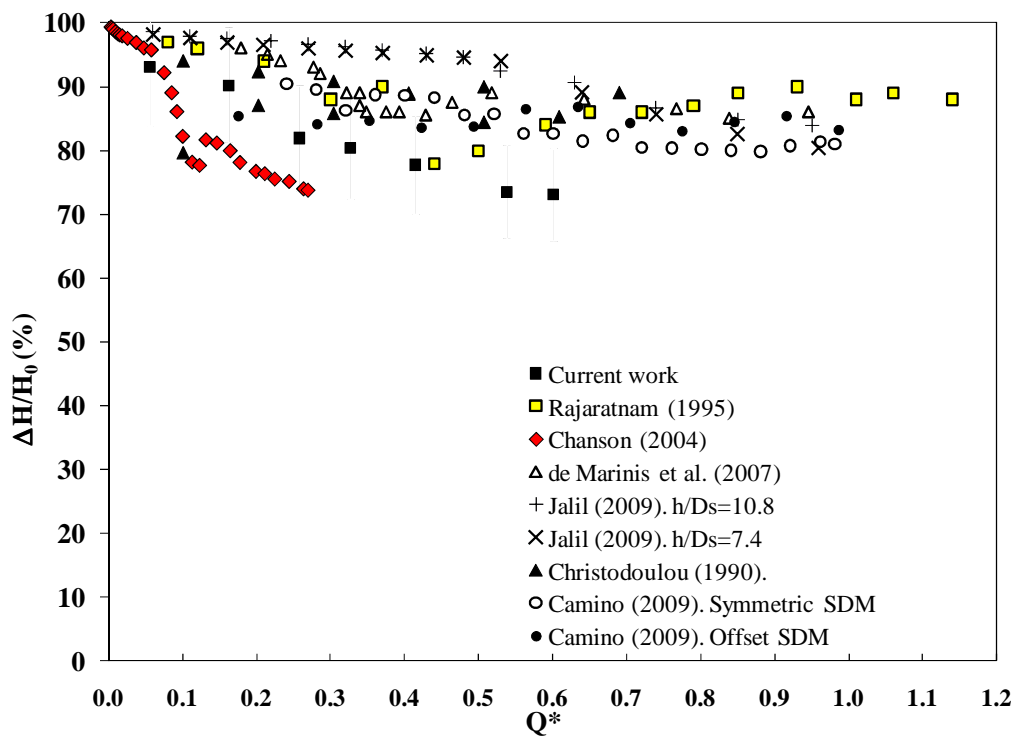


Figure 5.16 Comparison of relative energy losses for a range of dimensionless discharges of diverse plunging drop structures

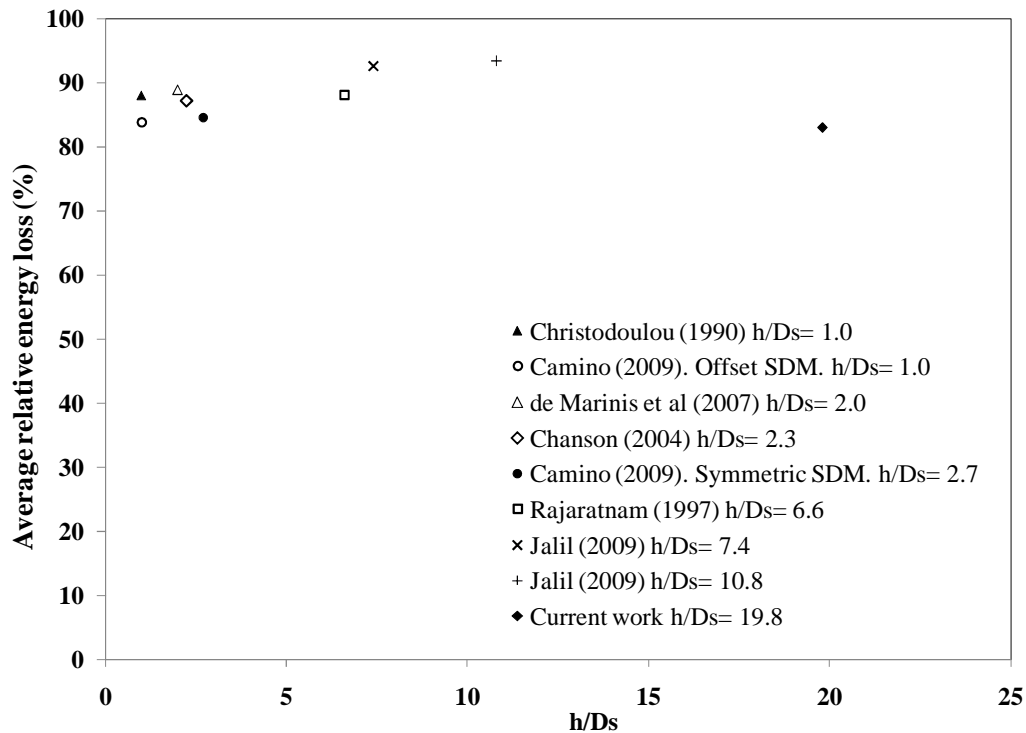


Figure 5.17 Comparison of mean relative energy losses with respect to the relative drop height of diverse plunging drop structures

5.3.4 Air demand

Large air entrainment was previously reported into dropshafts. Air captured in the urban drainage systems is not desirable. The formation of air traps within the system may generate high-pressure releases of air-water mixture and transient phenomena (Edwini-Bonsu and Steffler 2004). Additionally, the water-air mixture (bulky flow) reduces the carrying capacity of the system. Local air entrainment and entrapment processes have been shown to be dependent on the hydraulic operating system (Granata et al. 2010); however the hydraulics of dropshafts, more so air entrainment, are not yet well understood.

Various mechanisms of air interaction could be found within a large plunging dropshaft, particularly: a) inflow jet impingement and bouncing in the inner walls of

the shaft; b) air entrainment drag by free falling water droplets and streams; c) jet plunging when a pool is formed at the bottom of the shaft otherwise jet impingement on the bottom of the shaft; d) Air entrainment/detrainment at the rough water surface of the bottom pool and at the supercritical outflow.

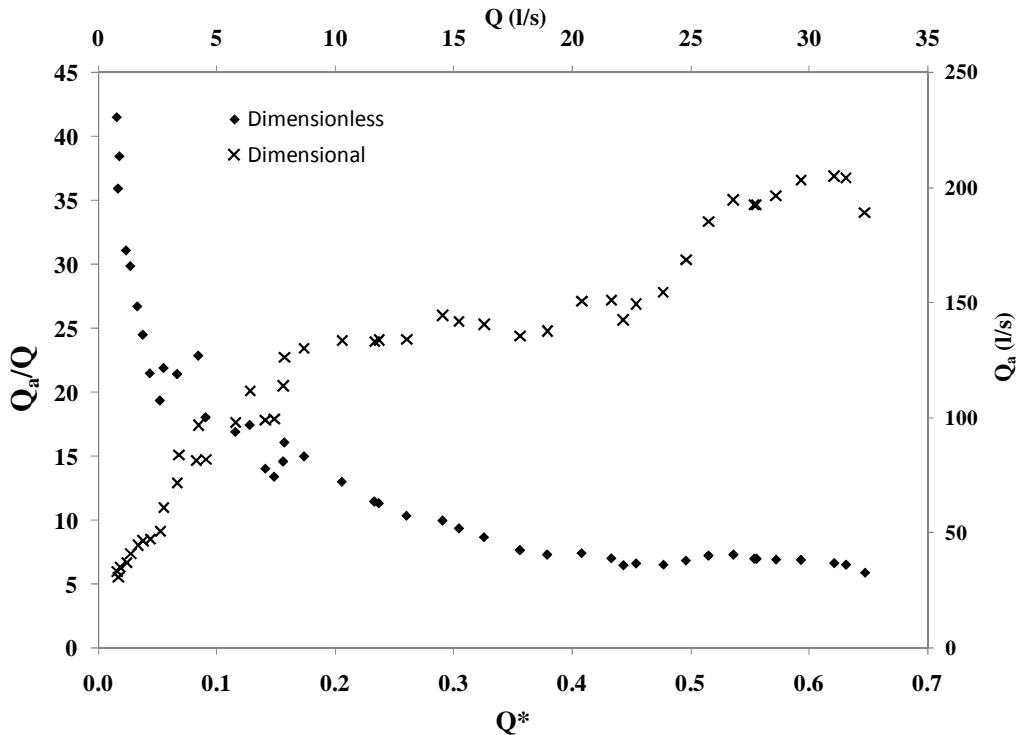


Figure 5.18 Air and water flow rates in a dimensional and dimensionless form

Relative air flow rates are typically expressed as $\beta=Q_a/Q$, where Q_a is the air demand into the structure and Q is the water discharge flowing into the structure in a steady state. Measurements in Fig. 5.18 were taken under essentially subcritical inflow condition. Fig. 5.18 shows an asymptotic curve of the relative air flow rate with increasing relative discharge Q^* . It appears that the y-axis in Fig. 5.18 for $Q^*=0$ represents the vertical asymptote to the curve in the lower end and a horizontal asymptote for β below 5 in the further end. Relative air discharges β as large as 40 were obtained for water flow rates below 1L/s. In a prototype dropshaft considering a Froudian similitude, it corresponds to about 16L/s, which is not an unusual sanitary

flow for big sewers.

Similar asymptotically decaying trend in the relative air flow rate was previously obtained by Rajaratnam et al. (1997) and Jalil (2009) (Fig. 5.19); they reported maximum values of β of 1.6 and 20, respectively. In dimensional form, the air demand is seen to increase with increasing water flow rate (secondary axes in Fig. 5.18). This tendency is not steady, a plateau is observed for Q between 7 and 22 l/s and above 26 l/s. A generalization of β to a curve of the form $\beta = a(Q^*)^b$, where a and b are experimental fitting coefficients was attempted showing inconclusive trends. The structure was also tested under no air supply from the single air vent in the shaft for the largest flow rate attainable for the pump ($Q^*=0.648$). No choking effect or water depth rising could be observed due to the small flow rate.

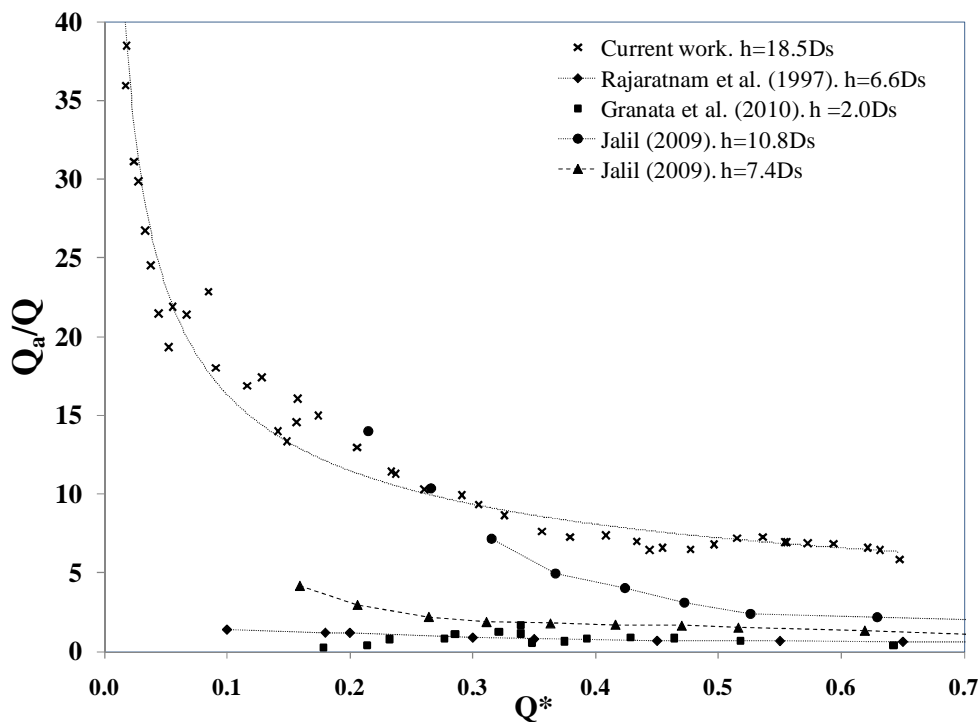


Figure 5.19 Comparison of relative air flow rates for different drop height plunging dropshafts

5.4 CONCLUSIONS AND REMARKS

A model exploratory study was carried out in a tall plunging dropshaft of 7.7m drop height (about 20 times its shaft diameter). The model could represent a typical prototype dropshaft in the city of Edmonton with a shaft diameter of 1.20m at a scale ratio of about three following a Froudian similitude. In a preliminary set of experiments, the effect of the ambient air into the shaft in the Blench Hydraulics Lab (air reservoir for the ventilation of the building) was assessed. Observations of the inflow jet in the impinging zone of the shaft revealed a thin spreading layer at low flow rates and splashing flow with a central downward ridge and an upward flow in the close neighborhood to the inlet for larger flow rates. Three regions of water flow across the shaft were recognized: a) an inner region containing a core intermittent stream; b) an outer region with smaller streams and drops, and c) a cylindrical wall jet region of flow adhered to the periphery of the wall. From high speed imagery, it was visualized that the core water stream is basically fed by the downward ridge. As the inflow discharge decreases, the central ridge appears to bounce further away from the impingement wall towards the opposite side of the shaft. Apparently, it diffuses and loses stability as it progresses further down the shaft.

Velocities computed from high speed photography, show that region of cylindrical wall jet achieve less velocity than inner streams and drops. Conversely to the wall jet velocity, the flow in the air space of the shaft show acceleration; yet, as compared to a Bernoulli jet attaining free fall velocity, the velocity decays.

For the range of water flows attained in the setup (up to 30L/s), no bottom pool was formed not even in the absence of air supply from the unique shaft's air vent. The relative energy loss achieved by the structure was about 85% for all the flow rates. The relative air flow rate β into the plunging dropshaft showed an asymptotically decaying curve with increasing dimensionless discharge Q^* . Values of β as large as 40 were obtained for the smallest water flow rates.

References

- A.E., Associated Engineering Alberta Ltd. (2008). "Odour Control Program Report - Draft". Edmonton, A. E. Alberta Ltd.
- Anderson, Alvin G. and Dahlin, Warren Q. (1975). "Dropshafts for the Tunnel and Reservoir Plan." *Minn Univ St Anthony Falls Hydraul Lab Proj Rep*,(154).
- Beltaos, S. and Rajaratnam, N. (1974). "Impinging circular turbulent jets." *J. Hydr. Eng. Div., ASCE*, 100 , HY10: 1313-1328.
- Calomino, F., Prega, G., Piro, P., and Veraldi, M.G. 1999. Hydraulics of drops in supercritical flow. 8 ICUSD, Sydney, Australia. Chanson, H. (2004). "Hydraulics of rectangular dropshafts." *Journal of Irrigation and Drainage Engineering*, 130(6): 523-529.
- Camino, G. A., Zhu, D. Z. and Rajaratnam, N. (2009). "Use of a stacked drop manhole for energy dissipation: A case study in Edmonton." *Can. J. Civ. Eng.*, 36: 1037-1050.
- Camino, G.A., Zhu, D.Z. and Rajaratnam, N. (2011). "Hydraulics of Stacked Drop manholes." *J. Irrig. Drain. Eng., ASCE*: In press.
- Chanson, H. (2002). "An experimental study of Roman dropshaft hydraulics." *J. Hydraul. Res.*, 40(1): 3-12.
- Chanson, H. 2004. *Hydraulics of rectangular dropshafts*. Journal of Irrigation and Drainage Engineering, **130**(6): 523-529.
- Chanson, H. (2007). "Air entrainment processes in a full-scale rectangular dropshaft at large flows." *Hydraulic Research*, 45(1): 43-53.
- Christodoulou, G.C. 1991. Drop manholes in supercritical pipelines. Journal of Irrigation and Drainage Engineering, **117**(1): 37-47.
- Dahlin, W.Q., Wetzel, J.M. and Nesbeitt, K.K. (1982). "Hydraulic modelling of vertical dropshaft structures." Coventry, U.K.: Sep.22-24, 1982, Cranfield, U.K., BHRA Fluid Engng., 1982, Paper X1, p.525-538.
- de Marinis, G., Gargano, R., Granata, F. and Hager, W.H. (2007). Circular drop manholes. Preliminary experimental results. *Proc. 32nd Congress of IAHR*, Venice, Italy, IAHR,.
- Edwini-Bonsu, S. and Steffler, P.M. (2004). "Air flow in sanitary sewer conduits due to wastewater drag: A computational fluid dynamics approach." *J. Environ. Eng. Sci.*, 3(5): 331-342.
- Falvey, H.T. (1980). "Air-water flow in hydraulic structures." *Water & Power Resour. Serv.* E. M. 41. Denver, U.S.A., USBR.
- Granata, F., de Marinis, G., Gargano, R. and Hager, W.H. (2011). "Hydraulics of circular drop manholes." *J. Irrig. Drain. Eng., ASCE*, 137(2): 102-111.

- Hoyt, J.W. and Taylor, J.J. (1977). "Waves in water jets." *J. Fluid Mech.*, 83(pt 1): 119-127.
- Li XM, Reinhoudt D, Calama MC (2007) What do we need for a superhydrophobic surface? A review on the recent progress in the preparation of superhydrophobic surfaces. *Chem Soc Rev*, 36:1350–1368
- Jalil, A., and Rajaratnam N. (2009), "Oblique impingement of circular water jets on plane boundaries" *J. of Hydraulic Research.*, 44(6): 807-814.
- Jalil, A. (2009). "Experimental and numerical study of plunging flow in vertical dropshafts". Doctoral thesis. Civil and Environmental Engineering. University of Alberta: 215p
- Kate, R.P., Das, P.K. and Chakraborty, S. (2007). "Hydraulic jumps with corners due to obliquely inclined circular liquid jets." *Physical Review E - Statistical, Nonlinear, and Soft Matter Physics*, 75(5).
- Kibar, A., Karabay, H., Yigit, K.S., Ucar, I.O. and Erbil, H.Y. (2010). "Experimental investigation of inclined liquid water jet flow onto vertically located superhydrophobic surfaces." *Exp. Fluids*, 49(5): 1135-1145.
- Mainali, A. and Rajaratnam, M. (1994). "Experimental study of debris flows." *J. Hydraul. Eng, ASCE*, 120(1): 104-123.
- Rajaratnam, N., Mainali, A. and Hsung, C.Y. (1997). "Observations on flow in vertical dropshafts in urban drainage systems." *J. Environ. Eng., ASCE*, 123(5): 486-491.
- Rao, A. and Arakeri, J.H. (2001). "Wave structure in the radial film flow with a circular hydraulic jump." *Exp. Fluids*, 31(5): 542-549.
- Quick, Michael C. (1990). "Analysis of spiral vortex and vertical slot vortex drop shafts." *J. Hydraul. Eng, ASCE*, 116(3): 309-325.
- Williamson, Scott (2001). "Drop structure design for wastewater and stormwater collection systems". W. B. P. F. Monographs. New York, Parsons Brinckerhoff Inc.: 131.

CHAPTER 6: CONCLUSIONS

An experimental investigation on stacked drop manholes (SDM) was carried out on two model structures with symmetric and offset alignments. An offset SDM was selected to resolve an elevation drop of 50 m in Windermere Subdivision in Edmonton. Four distinctive regimes classified were related to the water depths in chambers and the particular geometry of the manhole. While the first regime (free overfall flow in both chambers) achieved an average energy dissipation of 86 %; the second regime (surface jet in chamber 2) diminished to about 70 %. The third (submerged opening from downstream) and fourth (fully submergence) regimes dropped to an average of 56 % and 45 % of total energy dissipation, respectively.

Evidently, the energy dissipation was associated with the inflow conditions, geometry of the design and outlet controls. However, small changes in the rectangular opening and drop heights in the chambers did not exhibit any significant effect on the global energy dissipation; a larger drop height in the second chamber apparently increased the energy dissipation achieved by that chamber. On the other hand, it was interesting to observe that at a constant Froude number the overall energy loss decreases with increasing discharge. Conversely, for a given discharge, an increase in the Froude number showed an increase in the relative energy losses.

Water depths inside the chambers of the structure were basically governed by the outlet controls and not directly dependent on the approaching flow conditions. A non-dimensional relationship was then established for predicting water depths based on the downstream control. Furthermore, a more general flow classification was proposed based on the water depth and the drop height inside a typical manhole for which the downstream controls are dominant.

In the symmetric SDM, three flow regimes were classified in the first chamber: 1) A regime RI featured by a free falling jet hitting the bottom of the chamber and maintaining open-channel flow throughout the structure; 2) A regime RIII characterized by an inflow jet impinging on the front wall; and, 3) A transitional regime RII when one or both nappes of the falling jet impinged in the surroundings of the in-between opening. In the second chamber, once the outlet entrance was submerged, two types of flow were featured: 1) when the outflow runs as full pipe flow; and, 2) when an orifice type of flow is developed in the outlet pipe.

From momentum considerations, predictions on pool depths and energy losses were derived for a critical condition; i.e. a dropshaft type flow in the first chamber and an orifice outflow in the second chamber. Empirical factors were required to adjust pool depth predictions with corresponding measurements. Relative energy head losses (η) ranged between 70 to 95% inside the SDM. A mild decrease on η was observed with an increase in flow rate. Under surcharged flow conditions, average loss coefficients of $K=2.7$ for the SDM of large opening height and $K=6.4$ for the SDM of small opening height were recorded. Finally, air flow rates were recorded in a SDM for the largest total drop height ($h=8D$) and two opening heights. Overall less air was entrained into the structure once submergence of the opening from downstream occurred as compared to other drop structures of similar height. The increased drop height tested in this design showed an adequate performance being efficient in dissipating energy and producing moderate air entrainment in the system.

From a design standpoint, a square geometry of $3D \times 3D$ in the chambers of a symmetric SDM is found sufficient to allow major mechanisms of recirculation and plunging. No added dissipating benefit is observed from a larger section ($3.2D \times 4D$) of an offset SDM. A rectangular opening of large height ($a=D$) produces small losses under surcharged condition being efficient in dissipating energy under free fall operation. A drop height of $8D$ does not show excessive air entrainment as compared to other drop structures; however, a noticeable reduction in air transported into the

outlet pipe is observed once the opening is submerged from downstream. Air vents in both chambers are required to supply the air demand. A free board of about $2D$ above the inlet pipe is recommended for supercritical inflows.

From a separate experimental investigation on a circular jet sliding vertically in a confined chamber with enclosures of $L/d=3.7$ and $L/d=2.5$, representing the pool formed at the base of drop structures of different kind, the following conclusions can be drawn:

The confined jet diffuses more rapidly than a free jet due to reverse flows acting against the inflow jet direction. At about $x=9d$ (axial distance), the centerline velocity of eccentric and centered jets decays to about 0.3 of the onset velocity for the larger level of confinement tested (i.e. $L/d=3.7$). While a centered jet appears to decay at a constant rate, an eccentric one apparently produces two linear gradients or rates of decay. The turbulence intensities increase as the jet travels downstream; achieving larger values in jets with larger levels of confinement for the same distance downstream of the nozzle pipe. The velocity profiles, in the two perpendicular planes crossing the centerline jet axis, show that similarity was not attained within the reach of measurement; however at sections close to the outgoing pipe, the velocities in the streamwise direction could be approximated by normal distributions. The Kolmogorov hypothesis of isotropic turbulence could be used as a first approximation to calculate the rate of energy dissipation within the chamber. Finally, a comparison of relative energy losses by jet diffusion computed with the theoretical model showed good agreement with the corresponding measurements.

Finally, a model study carried out in a tall plunging dropshaft revealed interesting hydraulic features that foster our understanding of the flow inside the structure. The slender geometry of the model dropshaft, i.e. drop height about 20 times the shaft diameter, represented a typical prototype dropshaft in the city of Edmonton at a scale ratio of about three following a Froudian similitude. Observations of the inflow

impingement on the shaft revealed a thin spreading layer at low flow rates and splashing flow with a central downward ridge for larger flow rates. Three regions of flow across the shaft were recognized: a) an inner region containing a core stream; b) an outer region with smaller streams and drops, and c) a cylindrical wall jet region of flow falling along to the periphery of the wall. From high speed imagery, it was visualized that the core water stream is basically fed by the downward ridge. As the inflow discharge decreases, the central ridge appears to bounce further away from the impingement wall towards the opposite side of the shaft. Apparently, the central stream diffuses and loses stability as it progresses down the shaft.

Velocities computed from high speed photography, show that region of cylindrical wall jet achieve less velocity than inner streams and drops. Conversely to the wall jet velocity, the flow in the air space of the shaft show acceleration; yet, as compared to a Bernoulli jet attaining free fall velocity, the velocity decays. The relative energy loss achieved by the structure was about 85% for all the flow rates. The relative air flow rate β into the plunging dropshaft showed an asymptotically decaying curve with increasing dimensionless discharge Q^* . Values of β as large as 40 were obtained for the smallest water flow rates.